Azerbaijan Journal of Physics

Fizika

Azerbaijan Journal of Physics

FIZIKA

Institute of Physics
Azerbaijan National Academy of Sciences
Department of Physical, Mathematical and Technical Sciences

STUDY OF WH PRODUCTION AT LHC USING DIFFERENT EVENT GENERATORS

F.N. AHMADOV[1,2], M.A. MANASHOVA[1,3]

[1]Joint Institute for Nuclear Research, Dubna, Russia
[2]Institute of Physics of ANAS, AZ1143, H. Javid ave., 131, Baku, Azerbaijan
[3]Dubna State University
e-mail: fahmadov@jinr.ru, munira.manashova@mail.ru

In this paper, the angular features of the signal and background processes of the associated production of the Higgs boson with W-boson are presented. Signal and background processes are generated using the CompHEP, POWHEG and PYTHIA generators. Monte Carlo data are processed in ROOT software. We also compared the shape of the distributions of kinematic variables obtained from different generators and found that the shape of these distributions is similar for different generators. Significant deviation of POWHEG distributions from other generators can be explained by the fact that it uses NLO correction while other generators use LO approximation.

1. INRTODUCTION

One of the important production mechanism for the Higgs bosons in the Standard Model is its associated production with the $W^{\pm}$ -boson, $q\bar{q} \rightarrow W^{\pm}H$, where the $W^{\pm}$ bosons decay into leptons and the Higgs boson decays into a $b\bar{b}$ pairs. This work is motivated by the fact that observing the decay of the Higgs boson into a pair of $b\bar{b}$ quarks is a very important discovery for particle physics. There are various generators for simulating processes used in high energy physics to study the properties of elementary particles and fundamental interactions. It is very useful to compare the results from different event generators, and to try to understand the differences. The choice of event generators depends on the level of agreement of the data obtained from it with the experimental data, but when presenting the results of the selected event generator, it can be criticized. This work was done by using CompHEP [1], PYTHIA [2] and POWHEG [3] Monte Carlo event generators, which are designed to calculate the total cross sections and provide kinematic distributions for processes with several particles in the final state. The Leading Order (LO) or Next-to-Leading Order (NLO) Parton Distribution Functions (PDF) can be used depending on the generators. The generated Monte Carlo events were analyzed using the ROOT program [4]. Comparison of the results obtained from different generators are presented. CompHEP starts with the Feynman rules for the Lagrangian of the gauge model and calculates the matrix element for any process defined by the user. CompHEP is able to compute basically the lowest order (LO) cross sections and distributions with several particles in the final state (up to 6-7). It can take into account, all quantum chromodynamics (QCD) and electroweak (EW) diagrams, masses of fermions and bosons and widths of unstable particles.

The PYTHIA program appeared to solve the problem related to drawing strings in proton-proton processes. We used the latest version (v8) of the PYTHIA program [5]. The working procedure with the generator was divided into several stages. The first one is the initialization phase. It defines all basic characteristics of the future generated process. The next step is the generation cycle. At this stage, the events that will be generated and analyzed later are set up. And at the last stage, after the completion of the generation process, we get the result as an event file.

The main idea in POWHEG is to generate the hardest process first. After that the event is feed to any shower generator for subsequent, softer radiation. The first POWHEG concept was the realization of Z pair production in hadronic collisions. Processes such as the gluon fusion production of Higgs boson, Drell-Yan vector boson production, and single-top production were later included. POWHEG is implemented for generic processes using the POWHEG BOX package. It allows automatically create own POWHEG implementation for a process with given NLO matrix elements. The POWHEG BOX is a general computer framework for implementing NLO calculations in programs according to the POWHEG method. It also provides a library where included processes are made available to users. It can be connected with all modern Monte Carlo shower programs.

2. SIMULATION OF SIGNAL AND BACKGROUND SAMPLES

The procedure for generating events in PYTHIA is strictly organized: switches and parameters cannot be changed during the run, therefore, it is necessary to initialize the generation completely before generating events. To get the correct results, you need to give a fairly accurate recipe for the structure of the run. The process of generating events using the PYTHIA generator consists of several stages. First, at the initialization stage, we select the process which is needed. At this stage, you can change the default value of the beam energy. After setting the number of

events, the event generation process starts. At the beginning of the generation process information for the first event is printed to ensure that everything is working as planned. At the last stage, we receive the results of the generation as a table for the first event and as an LHE or root file that contains information about all events.

The CompHEP package is designed to calculate cross sections and generation of hard (basic) processes from matrix element (lagrangian) in the lowest order of perturbation theory. No higher order correction and hadronization are possible. CompHEP is divided into two separate parts, symbolic and numerical ones. The symbolic program is compiled and conserved in the installation area. The numerical binary is designed from several libraries and C code generated by the symbolic program. The calculation of signal and background processes in the program is carried out by determining the model of the interaction of elementary particles, which is necessary to continue work. The

first thing user should do is to choose the desired model. The procedure for generating events with CompHEP was exercised as in [6].

The first step in the generation of the code for a new process in POWHEG is to create a directory under the main POWHEG BOX and to work from inside this folder. This directory is called the process folder, from where all script files have to be executed. For a complete generation process, the basic necessary steps are performed as in [7].

In this paper, we considered $pp \to WH \to l\nu b\bar{b}$, as a signal process, $pp \to WZ \to l\nu b\bar{b}$ and $pp \to Wb\bar{b} \to l\nu b\bar{b}$ as background processes, where $l = e^{\pm}$ or $\mu^{\pm}$. The energies of the first and second beams (protons) were set to 6500 GeV, i.e. a total energy was 13 TeV. In all generators, 125 GeV was taken as the mass of the Higgs boson. Table 1 illustrates some features of the generators used in this work.

Table 1. Main features of the generators for signal process

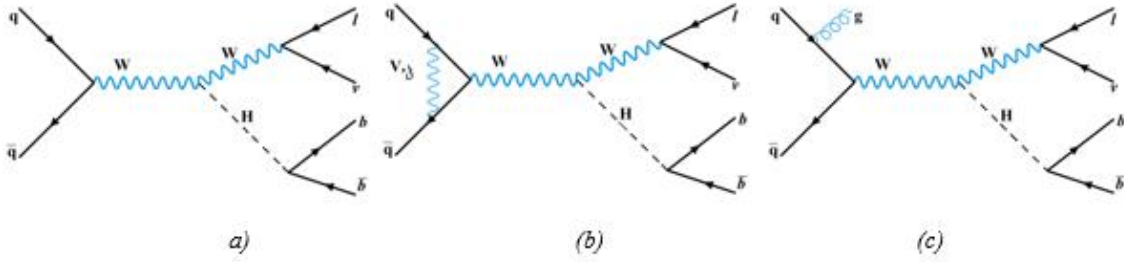|	CompHEP	PYTHIA8	POWHEG
# event	320000	320000	310000
Type of calculation	LO	LO	NLO
Parton-distribution function (PDF)	CTEQ6l1	CTEQ6l1	CTEQ6M

Fig. 1. Feynman diagrams for WH process at LO (a) and at NLO (b,c) as EW and QCD corrections to the LO respectively.

The LO and some NLO Feynman diagrams for the $pp \to WH \to l\nu b\bar{b}$ process are shown in Figure 1. The difference in transverse momentum distributions between the LO and NLO event generators can be seen in Figure 2. It should be noted that the differences between LO and NLO generators are not limited to the difference in the PDFs they use.

Another difference between them is that at the hard scattering level the formers use tree level matrix elements while the latter use one loop matrix elements. In the case of generating events with NLO matrix elements you improve the precision by lowering the dependencies of the renormalisation and factorization scales. The cross-section in the next to leading order approximation can be different from the cross-sections in the leading order by up to 30%. There are number of background processes that have large cross sections. In this work, we propose and use some variables ($cos\theta_l$, $cos\theta_W$) that will help to solve the background dominance problem.

3. EVENT SELECTION AND DATA ANALYSIS

Due to the big amount of background events, the search for signal events is complicated. Therefore, the choice of kinematic variables is important for the signal event selection. Some of the variables are determined using an approach that was used in the analysis at LEP [8] and in the ATLAS experiment [9]. One of these variables is transverse momentum of the charged lepton from the W decay (Figure 2). Another variable we use is the angle of the charged lepton in W rest frame relative to the W direction in WH or WZ/$Wb\bar{b}$ center of mass system for the signal and background processes respectively. To determine this angle, we have to transform all momenta from laboratory system to the WH center-of-mass frame (c.m.f.). Then we rotate the direction of the W-boson so that it coincides with the z-direction. Finally, we transform momentum of W boson along the z- axis to rest frame of W-boson. Since the same variable for

other particles of final state (neutrino, b and anti b-quarks) depends on each other and does not provide additional information, we define this variable only for the charged lepton. Figure 3a presents the comparison of the distributions of cosine of the charged lepton decay angle in the W rest frame relative to the W direction in the q$\bar{q}$ c.m.f. and figure 3b - the cosine of the W-boson polar angle with respect to the collision axis in the q$\bar{q}$ c.m.f. for events that are received from POWHEG, PYTHIA8 and CompHEP generators. Before creating these plots, we select events by applying a cut to some kinematic variables. These variables and applied cuts are as follows:

- The transverse momentum of a charged lepton, b- and anti b-quarks are required to be greater than 25 GeV, and for neutrinos - greater than 20 GeV.
- The pseudorapidity of the charged lepton, b- and anti-b-quarks should be within [-2.5, +2.5].
- The transverse momentum of the W boson must be greater than 150 GeV.

These cuts were selected according to those used in the analysis of experimental data [10]. They are related to the possibilities of reconstruction and calibration of the jets and leptons and suppression of the detector effects.

Fig. 2. Distributions of the transverse momentum of the charged lepton.

Fig. 3. Distributions of the cosine of the charged lepton (a) angle in the *W* rest frame relative to the *W* direction in the q$\bar{q}$ c.m.f. and (*b*) the cosine of the *W*-boson polar angle from the collision axis in the q$\bar{q}$ c.m.f. for different generators.

5

(a) *(b)* *(c)* *(d)* *(e)* *(f)*

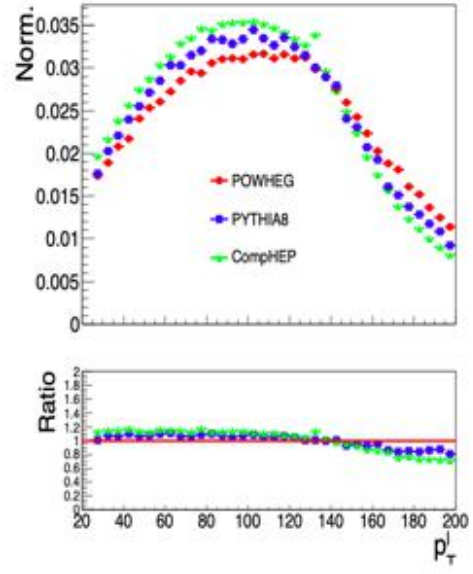*Fig. 4.* Distributions of the transverse momentum of the charged lepton, the cosine of the charged lepton angle in the W rest frame relative to the W direction in the $q\bar{q}$ c.m.f. and the cosine of the W-boson polar angle from the collision axis in the $q\bar{q}$ c.m.f. for *WH, ZH* and *Wb$\bar{b}$* events obtained (*a, c, e*) from CompHEP and (*b, d, f*) from PYTHIA8.

The distributions of some kinematic variables for the signal and background processes were compared. This procedure was repeated for events, simulated by various generators, in this case the PYTHIA8 and CompHEP generators. The distributions of three variables for signal and background samples are presented by 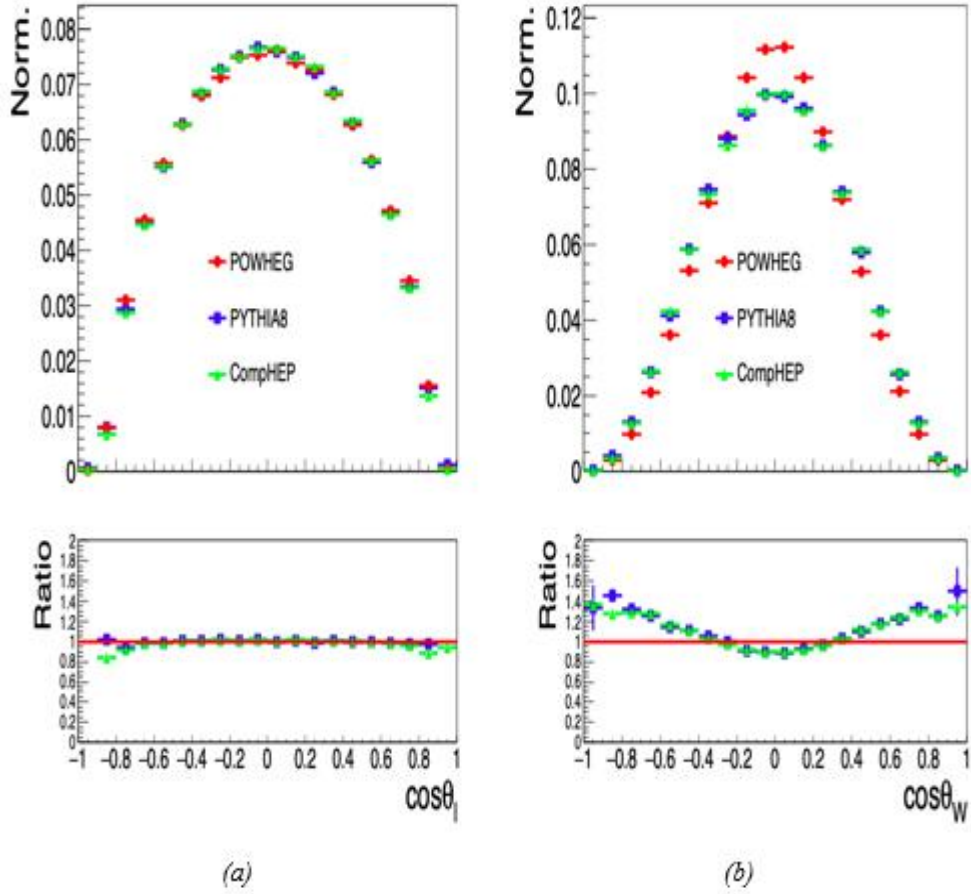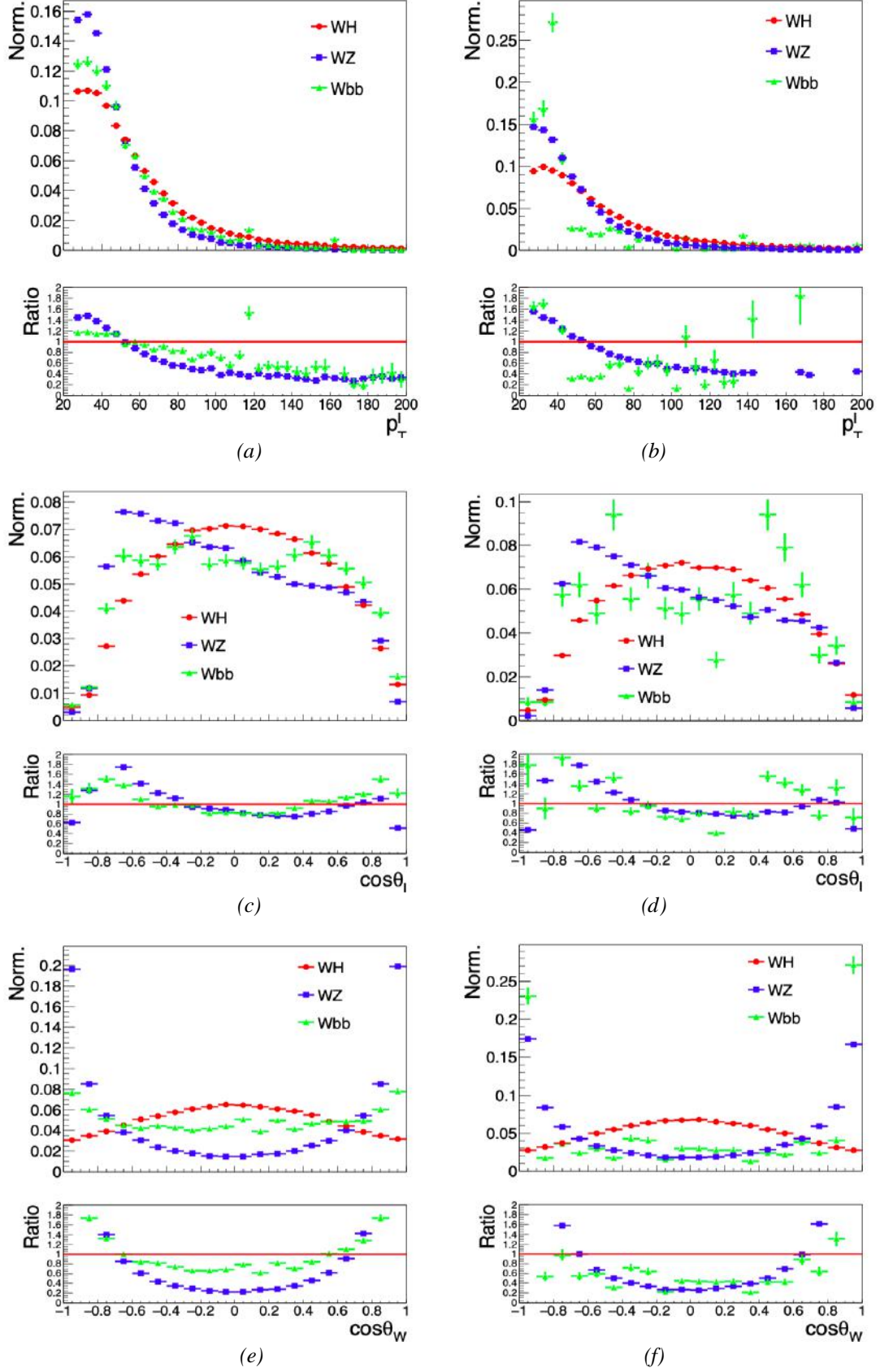Figures 4 (a-f). These variables are the transverse momentum of the charged lepton (a, b), the cosine of the charged lepton decay angle in the W rest frame relative to the W direction in the $q\bar{q}$ c.m.f. (c, d) and the cosine of the W-boson polar angle from the collision axis in the $q\bar{q}$ c.m.f. (e, f). The left plots (a, c, e) in Figure 4 were obtained using CompHEP generator, and the right plots (b, d, f) were obtained using PYTHIA8. In the plots, the signal is shown by a histogram with a red full circle, and WZ and $Wb\bar{b}$ are shown by a blue full square and a green full triangle, respectively. The difference in the shape of the distribution of the $Wb\bar{b}$ process between PYTHIA8 and CompHEP is due to the fact that in PYTHIA8 we cannot generate the $Wb\bar{b}$ directly, but only by generating the W+gluon and W+gamma processes, where the gluon and gamma decay into $b\bar{b}$.

4. CONCLUSION

From Figures 2 and 3, it can be seen that the shape of the distributions of variables for different generators are similar and the small difference between POWHEG and two other generators can be explained by the difference in the level of corrections (NLO and LO) that are taken into account during the event generation. It is obvious from Figures 4 that the shape of the distributions of variables for signal and background processes is very different. And these differences can be used in future analyses to suppress a large background contribution. The similarity of these distributions for the CompHEP and PYTHIA8 generators validates these variables and allows them to be used in the event selection process.

———————————————————————

[1]   *A. Pukhov, E. Boos, M. Dubinin, V. Edneral, V. Ilyin, D. Kovalenko, A. Kryukov, V. Savrin.* CompHEP - a package for evaluation of Feynman diagrams and integration over multi-particle phase space. User's manual for version 33, 2000 [arXiv:hep-ph/9908288].

[2]   *T. Sjostrand, S. Mrenna, P. Skands.* PYTHIA 6.4 physics and manual, JHEP 0605: 026,2006 [arXiv: hep-ph/0603175].

[3]   *S. Frixione, P. Nason and C. Oleari.* Matching NLO QCD computations with Parton Shower simulations: the POWHEG method, JHEP 11, 2007, 070 [arXiv:0709.2092].

[4]   *Rene Brun et al.,* ROOT Data analysis framework User's Guide, May 2018.

[5]   *T. Sjostrand, S. Mrenna and P.Z. Skands.* A Brief Introduction to PYTHIA 8.1, Comput. Phys. Commun. 178, 2008, 852 [arXiv:0710.3820].

[6]   Spin effects in the process of associative production of the Higgs boson and W± boson, F.Ahmadov, M.Manashova, Eurasian Journal of Physics and Functional Materials, Vol.4,#2, 2020, 132-138.

[7]   *Gionata Luisoni, Paolo Nason, Carlo Oleari, Francesco Tramontano.* HW/HZ + 0 and 1 jet at NLO with the POWHEG BOX interfaced to GoSam and their merging within MiNLO, 2013.

[8]   OPAL Collaboration, W-boson polarization at LEP2, Physics Letter B 585, 2004, 223-236.

[9]   ATLAS Collaboration, Measurement of W±Z production cross sections and gauge boson polarization in pp collisions at √s = 13 TeV with the ATLAS detector, Eur. Phys. J. C, 2019, 535.

[10]   ATLAS Collaboration, Observation of $H \to b\bar{b}$ decays and VH production with the ATLAS detector, Phys. Lett. B 786, 2018, 59.

FOUR WAVE INTERACTION IN THE CONSTANT INTENSITY APPROXIMATION

SH.SH. AMIROV

Faculty of Physics, Baku State University , 23 Z. Khalilov str., Az-1148, Baku, Azerbaijan
Department of Medical and Biological Physics, Azerbaijan Medical University
167 S.Vurgun str., Az-1022, Baku, Azerbaijan
E-mail: phys_med@mail.ru

Parametrical interaction of waves with four frequencies in nondissipative negative index materials is studied by employment the constant intensity approximation, taking into account the reverse reaction of excited waves onto the exciting ones. An expression for complex amplitude as well as the efficiency of conversion to signal wave at the frequency ω_1 in arbitrary phase detuning is obtained. It is shown that in contrast to the constant field approximation both amplitude and conversion efficiency are the functions of intensities of forward pump waves as well as the weak wave at frequency ω_2 in the constant intensity approximation. It is shown that maxima or minima of the conversion efficiency displace with alteration of weak wave intensity. Analytical expression for the optimum value of phase mismatch at which reflective index reaches its maximum is derived.

Keywords : metamaterials, phase mismatch, for wave mixing, coefficient of reflection, constant intensity approximation.
**PACS:** 78.67.Pt ; 42.65-k; 42.70-a

1. INTRODUCTION

The prospective negative index materials (NIM) are attractive with their unusual structure and properties [1,2]. The mesh of split-ring resonators are placed periodically. Each cavity is constructed of two concentric rings with a certain gap. The air gap between inner and outer ring serves as a capacitor. However the rings are act as an inductor making the LC resonant circuit.

Since NIM includes electro conducting wires-rods and split-ring resonator (Fig.1) the nonlinear response of material also has two components. Effective dielectric permittivity $\varepsilon = 1 - \omega_r^2/\omega$ where ω_r is the is the plasma frequency and ω is the frequency of the propagating electromagnetic wave. The effective permittivity is negative when the frequency is below the plasma frequency. When operating at the plasma frequency, the effective permittivity is zero, and hence yields a zero index of refraction. In a traditional nonlinear media four-frequency interaction are devoted number of works [3,4]. Investigations of nonlinear four-photon mixing in optical fibers are presented for the general case of depleted pump power in [5]. Efficiency of generation upon experimental four-frequency mixing in a layered negative index structure metal-dielectric-metal is higher as two orders as compared to that of generation in a pure gold film of 20nm thickness. Parametrical interactions of optical waves were investigated in metamaterials [6-8] by employment constant intensity approximation [9-13]. This paper centers on the study the four-frequency nonlinear mixing of optical waves in case of negligible linear losses .

2. THEORY AND DISCUSSIONS

We assume that idler A_2 and two pump waves $A_{3,4}$ are normally incident onto the left side surface of metamaterial with length l and propagate along positive direction of z- axis, while signal wave A_1 propagates in the opposite direction. Hence energy fluxes are as follows; $S_{2,3,4} -$ in thye positive direction of z-axis and S_1 in the negative direction (Fig.1).
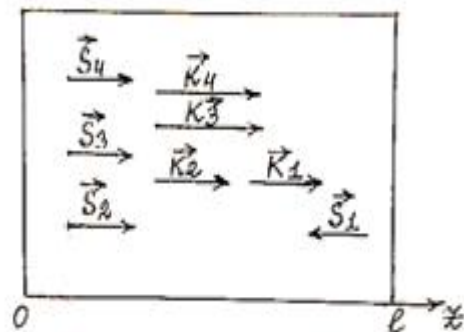
When three light waves at frequencies ω_2 , ω_3 and ω_4 are incident onto cubic nonlinear medium the nonlinear polarization leads to the generation of a new electromagnetic with frequency $\omega_1 = \omega_3 + \omega_4 - \omega_2$. In a photon language the FWM is that two photons with initial frequencies are subjected to elastic scattering to produce two new photons. Here the law of conservation of energy and momentum have to be fulfilled in this process: $k_1 = k_3 + k_4 - k_2$ where $k_j -$ are the wave numbers at respective frequencies $\omega_j (j = 1 - 4)$. Conservation of momentum leads to the phase matching conditions. Boundary conditions of the described interaction of waves are given by $A_{2,3,4}(z = 0) = A_{20,30,40}$ and $A_1(z = l) = A_{1l}$, where $z = 0$ corresponds to the left input of the metamaterial, $A_{20,30,40}$ are the initial amplitudes of the transmitted weak wave (A_{20}) at the frequency ω_2 and of the pump waves ($A_{30,40}$) at the frequencies $\omega_{2,3}$ and A_{1l} is the initial amplitude of the transmitted signal wave at the right input of the nonlinear medium at $z =$

l. For this consideration dielectric permittivity of the signal wave becomes negative that is reflected in the first equation of following set of reduced equations ($\delta_i = 0$):

$$\frac{dA_1}{dz} = -i\gamma_1 A_3 A_4 A_2^* e^{i\Delta z}, \quad \frac{dA_2}{dz} = i\gamma_2 A_3 A_4 A_1^* e^{i\Delta z}$$

$$\frac{dA_3}{dz} = i\gamma_3 A_1 A_2 A_4^* e^{-i\Delta z}, \quad \frac{dA_4}{dz} = i\gamma_4 A_1 A_2 A_3^* e^{-i\Delta z}$$

(1)

where A_j -are the complex amplitudes of the magnetic fields of the transmitted quasi-monochromatic waves, $\gamma_1 = 2\pi k_1 \chi_1^{(3)}/|\varepsilon_1|$ and $\gamma_{2,3,4} = 2\pi k_{2,3,4} \chi_{2,3,4}^{(3)}/\varepsilon_{2,3,4}$

are the nonlinear wave coupling coefficients, $\chi_j^{(3)}$ is the cubic susceptibility, and $\Delta = k_3 + k_4 - k_1 - k_2$ is the phase detuning of the interacting waves. The corresponding equations for the electric components can be derived analogously with replacement of the dielectric permittivity of the medium ε_j by the magnetic permeability μ_j and *vise versa* [14].

Differentiation of the first equation of system (1) yields to the following second order differential equatiuon

$$\frac{d^2 A_1}{dz^2} - i\Delta \frac{dA_1}{dz} + (\gamma_1\gamma_2 I_{30} I_{40} - \gamma_1\gamma_3 I_{20} I_{40} - \gamma_1\gamma_4 I_{20} I_{30} + \Delta^2/4)A_1 = 0$$

(2)

Having put $A_1 = a_1 \times \exp(i\Delta z/2)$ in the (2) gives

$$\frac{d^2 a_1}{dz^2} + \lambda^2 a_1 = 0$$

(3)

Where

$$\lambda = (\gamma_1\gamma_2 I_{30} I_{40} - \gamma_1\gamma_3 I_{20} I_{40} - \gamma_1\gamma_4 I_{20} I_{30} + \Delta^2/4)^{1/2}$$

Solution of (3) is given by

$$a_1 = C_1 \cos\lambda z + C_2 \sin\lambda z$$

(4)

For a complex amplitude of signal wave we can write

$$A_1 = (C_1 \cos\lambda z + C_2 \sin\lambda z)\exp(i\Delta z/2)$$

(5)

Equation constants C_1 and C_2 are found by the boundary conditions:

$$A_1(z = l) = A_{1l} \text{ and}$$
$$A_{2,3,4}(z = 0) = A_{20,30,40}$$

(6)

Employment of the first condition yields for constant C_1:

$$C_1 = \frac{A_{1l} e^{-\frac{\Delta l}{2}}}{\cos\lambda l} - C_2 \tan\lambda l$$

(7)

Application the second condition to the first equation for C_2 gives

$$C_2 = -i[\gamma_1 A_{30} A_{40} A_2^* + (\Delta/2)C_1]/\lambda$$

(8)

Further substitutions has allowed to obtain complex amplitude of the signal wave in non-dissipative medium in the form

$$A_1(z) = (M_1 + iM_2)e^{\frac{\Delta z}{2}}$$

(9)

Here

$$M_1 = \frac{A_{1l} e^{-i\frac{\Delta l}{2}}\cos\lambda z + m(\Delta/2)\frac{\sin\lambda l}{\lambda}\frac{\sin\lambda z}{\lambda}}{\cos\lambda l - i\frac{\Delta}{2\lambda}\sin\lambda l}$$

$$M_2 = \frac{m\sin\lambda l \frac{\cos\lambda z}{\lambda} - A_{1l} e^{-\frac{\Delta l}{2}}(\Delta/2)\frac{\sin\lambda z}{\lambda}}{\cos\lambda l - i\frac{\Delta}{2\lambda}\sin\lambda l} - m\frac{\sin\lambda z}{\lambda}$$

where $\lambda = (\gamma_1\gamma_2 I_{30} I_{40} - \gamma_1\gamma_3 I_{20} I_{40} - \gamma_1\gamma_4 I_{20} I_{30} + \Delta^2/4)^{1/2}$, $\quad m = \gamma_1 A_{30} A_{40} A_2^*$

In the input ($z = 0$) to the medium amplitude of signal wave is simplified as

$$A_1(z) = (M_3 + iM_4)$$

(10)

where

$$M_3 = A_{1l} e^{-i\frac{\Delta l}{2}}/(\cos\lambda l - i\frac{\Delta}{2\lambda}\sin\lambda l)$$

$$M_4 = m\frac{\sin\lambda l}{\lambda}/(\cos\lambda l - i\frac{\Delta}{2\lambda}\sin\lambda l)$$

Having put Euler's formula $e^{-i\frac{\Delta l}{2}} = cos\frac{\Delta l}{2} - isin\frac{\Delta l}{2}$ into expression (10) we get amplification factor η= $I_1(z = 0)/I_{1l}$ of a signal wave in case of arbitrary phase detuning:

$$\eta = \frac{(\frac{\Delta}{2\lambda}sin\lambda l \cdot sin\frac{\Delta l}{2} + cos\frac{\Delta l}{2}cos\lambda l - \frac{m\Delta sin^2\lambda l}{A_{1l}}\frac{}{\lambda^2})^2 + (cos\frac{\Delta l}{2} \cdot \frac{\Delta}{2\lambda}sin\lambda l - sin\frac{\Delta l}{2}cos\lambda l + \frac{m}{A_{1l}}\frac{sin2\lambda l}{2\lambda})^2}{[\,cos^2\lambda l + (\frac{\Delta}{2\lambda})^2 sin^2\lambda l]^2} \qquad (11)$$

Energy exchange between interacting waves is mainly dependent on the phase matching conditions. When this condition satisfy enhancement of idler and signal waves occur because they extract energy from two pump waves. In opposite case energy can flow back from idler and signal waves to the pump waves. When two pumps and a signal wave are incident onto nonlinear medium the idler wave is generated through four-wave mixing. Phase matching is important for signal amplification and generation of idler wave.

In the left input ($A_{1l} = 0$) of nonlinear medium the coefficient of reflection of the mirror that is the metamaterial itself due to its negative refractive index is calculated from the (11) by the following expression:

$$R = \frac{I_1(z=0)}{I_{20}} = (\gamma_1 A_{30}A_{40}tan\lambda l)^2 / \left(\lambda^2 + \frac{\Delta^2}{4} tan^2\lambda l \right) \qquad (12)$$

where

$$\lambda^2 = \frac{\Delta^2}{4} + K \ , \ \ K = \gamma_1\gamma_2 I_{30}I_{40} - \gamma_1\gamma_3 I_{20}I_{40} - \gamma_1\gamma_4 I_{20}I_{30}$$

To obtain the optimal value of phase mismatch parameter at which reflective index becomes maximum we differentiate expression (12) with respect to parameter Δ . Calculation shows that refractive index reaches its maxima when condition $\lambda l = 0, \ 1.5\pi, \ 2.5\pi, \ 3.5\,\pi$ is fulfilled. For optimal value of phase mismatch parameter then we get

$$\Delta_{\text{opt},1} = 2\sqrt{\gamma_1\gamma_3 I_{20}I_{40} + \gamma_1\gamma_4 I_{20}I_{30} - \gamma_1\gamma_2 I_{30}I_{40}} \qquad (13)$$

Principal maximum of reflective coefficient is obtained near to the $\Delta = 0$, which depends on the intensities of pump waves and idler wave.

Under phase matching conditions (Δ= 0) we get from (10) more simplified expression for the amplitude of a signal wave :

$$A_1(z) = (M_5 + iM_6) \qquad (14)$$

where $M_5 = A_{1l}/cos\lambda_1 l$, $M_6 = \frac{m}{\lambda}tan\lambda_1 l$, $\lambda_1 = (\gamma_1\gamma_2 I_{30}I_{40} - \gamma_1\gamma_3 I_{20}I_{40} - \gamma_1\gamma_4 I_{20}I_{30})^{1/2}$

All dependences of (10) and (12) on the various parameters of problem can be obtained in both constant field approximation and constant intensity approximation. Qualitative analysis of the formula (10) results in the following: conversion efficiency of energy of a signal wave has oscillator character which decrease with increase in the phase mismatch parameter. When coefficients γ_3 and γ_4 are differ from zero in the expression for λ we get result of constant intensity approximation while equality to zero is analogous to the result of constant field approximation.

As can be seen in contrast to the constant field approximation efficiency of conversion depends on the intensity of idler wave at frequency ω_2 in addition to other parameters. When we consider problem in the constant field approximation maxima and minima corresponding to different plots are coincide while those displace as a function of weak wave intensity in the constant intensity approximation.

Qualitative consideration shows that it is possible to obtain enhancement of the backward signal wave by varying the input intensities of forward waves.

3. CONCLUSIONS

On the basis of above stated one can conclude that efficiency of frequency conversion , coefficient of reflection upon four wave mixing in the constant intensity approximation are the functions of metamaterial thickness, intensities of forward pump waves as well as weak wave at frequency ω_2 . There is optimum value of phase mismatch at which coefficient of reflection reaches its maximum. In contrast to the constant field approximation , efficiency of frequency conversion increases with increase in the intensity of weak wave in the constant intensity approximation taking into account reverse reaction of excited waves on the phases of exciting waves. An existence a displacement of maxima and minima of conversion efficiency oscillations due to variations in intensity of weak wave has allowed to determine distance between neighbor minima or maxima and hence period of oscillations.

_____

FOUR WAVE INTERACTION IN THE CONSTANT INTENSITY APPROXIMATION

[1] *S.A. Akhmanov, V.A. Visloukh, A.S. Chirkin.* UFN 1986, v. 149, issue 3, p. 449-509.

[2] *Kh. Shumin, V. P. Drachev, A. V. Kildishev, et al.,* Nature, 2010, 466, 735–742.

[3] *K.K. Thyagarajan, Ajoy Ghatak.* Guided Wave Optical Components and devices. 2006.

[4] *F .Yaman, Govind P. Agrawal.* Guided Wave Optical Components and devices. 2006.

[5] *Yijiang Chen and Allan W.Snuder.* Optical letters, v.14, issue 1, 1989, pp. 87-89.

[6] *R.J. Kasumova, Z.H. Tagiyev, Sh.Sh. Amirov et al.*, J. Russ. Laser Res., 2017, 38, 211–218.

[7] *R.J. Kasumova, Sh.Sh. Amirov, and A.A. Shamilova.* Kvant. Elektr., 2017, 47 (7), 655–660.

[8] *Z.A. Tagiev, R.J. Kasumova, and R.A. Salmanova.* Opt. Spektrosk., 1999, 87, 94–97.

[9] *Z.H. Tagiev, R.J. Kasumova, R.A. Salmanova, and N.V. Kerimova.* J. Opt. B, 2001, 3, 84–87.

[10] *R.J. Kasumova, Sh.Sh. Amirov.* Superlattices and microstructures Vol. 126, 2019, p. 49-56.

[11] *Sh.Sh. Amirov, Z.H. Tagiyev, G.N. Akhmedov.* AJP "Fizika" v. XXIV, 2018, N 4 p. 7-10.

[12] *Sh.Sh. Amirov, R.J. Kasumova, Z.H. Tagiev.* Proceedings of International conference "Modern Trends in Physics" 2019, p. 205-210.

[13] *Sh.Sh. Amirov, R.J .Kasumova, Z.H. Tagiev.* Proceedings of the VIII International scientific-practical conference "Science and practice: implementation to modern society ", Manchester, Great Britain December 26-28, 2020, Scientific Collection "Interconf". 2020, N 3 (39) p.1212-1214.

[14] *A.K. Popov and V.M. Shalaev.* Appl. Phys. B, 84, 2006, 131–137.

PHOTOLUMINESCENCE OF $Ca_4Ga_2S_7:Eu^{2+}$ COMPOUND

B.D. URMANOV[1], M.S. LEONENYA[1], P.G. YABLONSKI[1],
O.B. TAGIYEV [2,3], F.A. KAZIMOVA[2], T.Sh. IBRAHİMOVA[2]
[1]Institute of Physics of Belarusian NAS, AZ1143, Minsk, Belarus
[2]Institute of Physics of ANAS, AZ1143, H. Javid ave., 131, Baku, Azerbaijan
[3] Branch of MSU named after M.V. Lomonosov, Baku, Azerbaijan
E-mail: oktay58@mail.ru

The photoluminescence (PhL) properties of chalcogenide $Ca_4Ga_2S_7:Eu^{2+}$ semiconductors in interval of impulse laser excitation from 10 up to 10^5 Vt/cm^2 at room temperature are studied.

PhL of $Ca_4Ga_2S_7:Eu^{2+}$ compound at excitation by radiation in range 450-575nm is characterized by essential dominance of the band in the spectrum on 660 nm. PhL of $Ca_4Ga_2S_7:Eu^{2+}$ compound on wave lengths 560 nm and 660nm damps at constant times 258 nsec and 326 nsec correspondingly.

Keywords: chalcogenide semiconductors, high excitation level, luminescence efficiency.
PACS: 76.30, 78.55

INTRODUCTION

The preparation of high-production devices for visualization and illumination which are able to compete with traditional systems requires the creation of luminophors with specific properties. This necessity causes to development of new materials or optimization of already existing luminophors.

In this aspect the triple alkaline-earth chalcogenide semiconductors of II-III$_2$-VI$_4$ (II-Ca, Ba, Sr; III-Ga, Al; VI-S, Se) type activated by rare-earth elements are perspective ones. In present, luminophors of above mentioned system activated by Eu ions attract investigators' attention, as they have properties required for comparably new technologies of plane screens, screens of inorganic electro-luminescence devices, including color TV and light sources [1 – 5].

$Ca_4Ga_2S_7:Eu^{2+}$ compound belongs to the group of high-performance luminophors with general formula $Ca_mGa_2S_n$:RRE (RRE is rare-earth element) where n=4,5,6,..., m = n-3 [6]. The compounds activated by 4f elements in M – Ga – S(Se) system can be active medium of semiconductor lasers, luminescence lamps, color displays and other systems of information mapping [7 – 9]. These compounds have the forbidden band width 3,0-4,4eV and effectively transform the electric field energy, roentgen and ultraviolet radiations, and also electron beams in visible light. The excitation spectrum of given compounds covers the region from vacuum ultraviolet up to 500 nm.

The investigation results of luminescence and optical properties of the crystals of $Ca_4Ga_2S_7$ type activated by Eu ions are shown in [10, 11]. The chalcogenide semiconductor $Ca_4Ga_2S_7:Eu^{2+}$ can be perspective luminophor for lighting devices on the base of InGaN-LD, however its spectral characteristics aren't studied enough. For establishment of usage possibility of this luminophor in such devices, it is necessary the study of its spectrum stability and radiation effectiveness in wide interval of excitation levels which is dedicated the present paper.

In the given paper the measurements of photoluminescence (PhL) spectra in the dependence on temperature and excitation level, excitation spectrums of photoluminescence and time-resolved photoluminescence spectra.

1. EXPERIMENT TECHNIQUE

The crystal samples $Ca_4Ga_2S_7$ are synthesized by solid-phase reaction of binary compounds CaS, Ga_2S_3 and EuF_3 at temperature 1400K taken in stoichiometric ratios in graphitized quartz ampoules evacuated up to 10^{-4} millimeter of mercury.

The obtained polycrystals are grinded with following deposition on quartz planes. The excitation spectra of photoluminescence (EPhL) are measured at excitation by monochromatic radiation of xenon lamp at temperature 300 K. The influence of excitation level on spectra and PhL efficiency in interval 10 –10^5 Vt/cm^2 is analyzed by integral PhL spectra of samples at excitation and 50 nano-sec impulse radiation of InGaN-LD on wave length 405 nm.

The investigation of damp kinetics of PhL micropowder $Ca_4Ga_2S_7:Eu^{2+}$ (5 %) is carried out at excitation by radiation of fourth harmonic of femtosecond Yb:KYW-laser on 260 nm at room temperature.

2. RESULTS AND THEIR DISCUSSION.

$Ca_4Ga_2S_7:Eu^{2+}$ (5 at.%) compound as a result of electron transitions in ions of Eu^{2+}- activator has PhL in yellow-red range in the form of two wide radiation bands with maximums on 560 and 660 nm at excitation by radiation on wave length 337 nm at room temperature (Fig.1., curve *1*).

The excitation spectra of short-wave band of PhL micropowder $Ca_4Ga_2S_7:Eu^{2+}$ (5 at. %) near 560 nm presents itself the wide band overlapping range from 250 up to 500 nm with maximum on 345 nm according to Fig.1 (curve *1'*). EPhL spectrum on 660 nm presents itself two wide bands overlapping

spectral ranges from 250 up to 350 nm and from 400 up to 625 nm with maximums on 265nm and 470nm correspondingly, as it is shown in Fig.1 (curve *2'*).

The essential differences of excitation spectra of PhL bands near 560 nm and 660 nm allows us to change the luminescence color of Ca$_4$Ga$_2$S$_7$:Eu^{2+} compound choosing the pumping source. As a result, PhL of Ca$_4$Ga$_2$S$_7$:Eu^{2+} compounds at excitation by radiation in range 450-575 nm are characterized by

significant dominance of the band in the spectrum on 660 nm in correspondence with Fig.1 (curve 1).

The obtained damp kinetics of PhL bands with maximums on 560 nm and 660 nm of Ca$_4$Ga$_2$S$_7$:Eu^{2+} (5 at.%) solid solutions are presented in Fig.2. The constants of damping times near 560 nm and 660 nm are 258 nsec and 326 nsec, correspondingly.
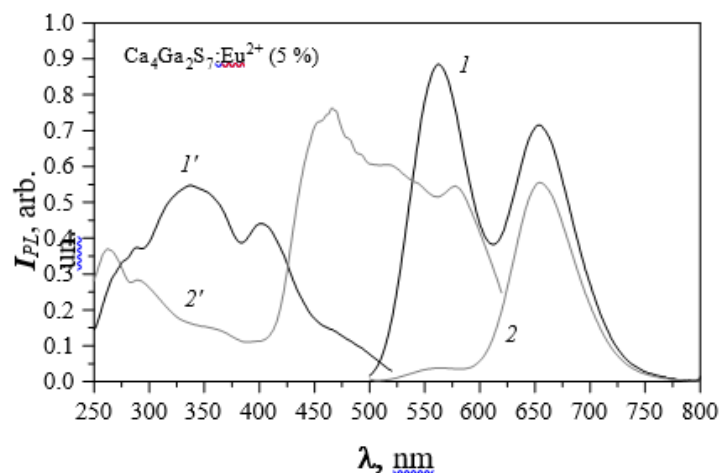

Fig.1. PhL spectra (curves *1* and *2*) and excitation PhL (curves *1'* and *2'*)
Ca$_4$Ga$_2$S$_7$:Eu^{2+} (5 at.%) compounds on wave lengths of excitation 337 nm (*1*) and 467 nm (*2*) and registration 560 nm (*1'*) and 660 nm (*2'*) at room temperature.
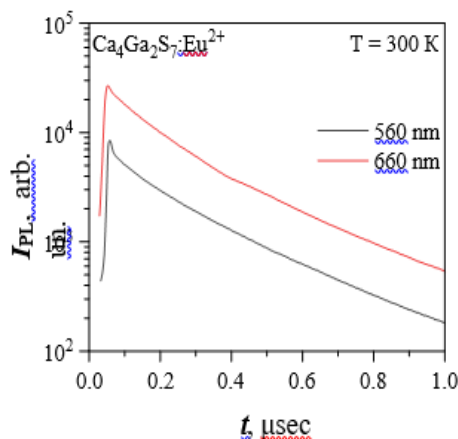

Fig.2. Damp kinetics of PhL bands with maximums on 560 nm and 660 nm of Ca$_4$Ga$_2$S$_7$:Eu^{2+} (5 at%) solid solutions at λ_{ex} = 260 nm and room temperature.

Ca$_4$Ga$_2$S$_7$:Eu^{2+} (5 at.%) compound has PhL in yellow-red range in the form of two wide radiation bands near 564 nm and 654 nm at temperature 10 K and excitation by continuous radiation on wave length 405 nm in correspondence with Fig.3 (a). Note that Eu^{2+} ions in different matrixes have wide bands of absorption and radiation. The radiation with wave length from ultraviolet up to red luminescence is observed in the dependence on matrix structure which is activated by Eu^{2+} ions [12]. 4f^7(^{8}S$_{/2}$) configuration is main unexcited state of Eu^{2+} ions and 4f^{6}5d configuration is excited state of Eu^{2+} ions. The intensive luminescence in yellow (564 nm) and red

(654nm) spectrum region is caused by 4f^{6}5d→4f^7(^{8}S$_{/2}$) electron transitions in Eu^{2+} ions.

The temperature increase from 10K up to 300K leads to widening of radiation bands of Ca$_4$Ga$_2$S$_7$:Eu^{2+} compound near 564 nm and 654 nm, blurring of their structure and the shift on 5 nm and 8 nm in short-wave side, correspondingly. The integral intensity decreases on 40%.

The significant stability behavior of PhL spectrum of Ca$_4$Ga$_2$S$_7$:Eu^{2+} compound in interval of excitation level from 10 Vt/cm^2 up to 2.2·10^5 Vt/cm^2 by impulse 50 nsec radiation of InGaN-LD on wave length 405 nm that is seen in Fig. 4(a), is observed [13]. PhL efficiency of Ca$_4$Ga$_2$S$_7$:Eu^{2+} compound saves its constant value in wide interval of excitation level from 10 Vt/cm^2 up to 2·10^4 Vt/cm^2 as it is seen in Fig.4 (b). The reversal efficiency decrease on 40% takes place with further increase of pumping up to 4·10^5 Vt/cm^2.

PhL kinetics of Ca$_4$Ga$_2$S$_7$:Eu^{2+} compound at room temperature and excitation level 2.2 μJ/cm^2 by impulse radiation of Yb:KYW-laser on wave length 260 nm and duration 140 fsec is described by two exponents with decay times 60 nsec and 240 nsec in correspondence with Fig.5. The further increase of pumping level up to 36 μJ/cm^2 leads to insignificant decrease of constant time of fast component up to 57 nsec. The presence of fast component in kinetics of PhL damping of Ca$_4$Ga$_2$S$_7$:Eu^{2+}compound at excitation by intensive laser radiation of femtosecond duration, is caused by the presence of cross-relaxation process that is character for semiconductor matrixes activated by Eu^{2+} ions.
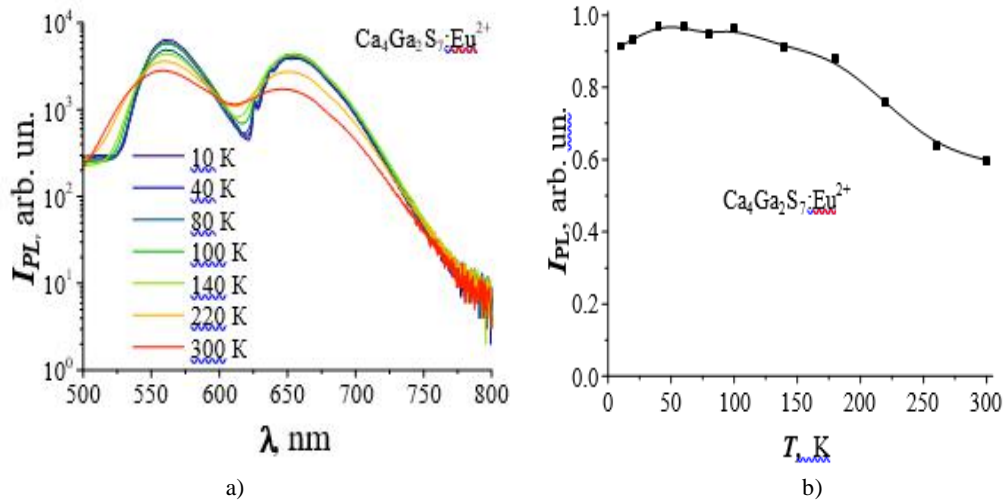
B.D. URMANOV, M.S. LEONENYA, P.G. YABLONSKI, O.B. TAGIYEV, F.A. KAZIMOVA, T.Sh. IBRAHİMOVA

a)

b)

Fig.3. PhL spectra of $Ca_4Ga_2S_7$:Eu^{2+}(a) compound and dependence of integral intensity of its PhL on temperature in interval 10 – 300K at excitation by radiation on wave length 405 nm with power density by order 1Vt/cm^2 (b).

a

b
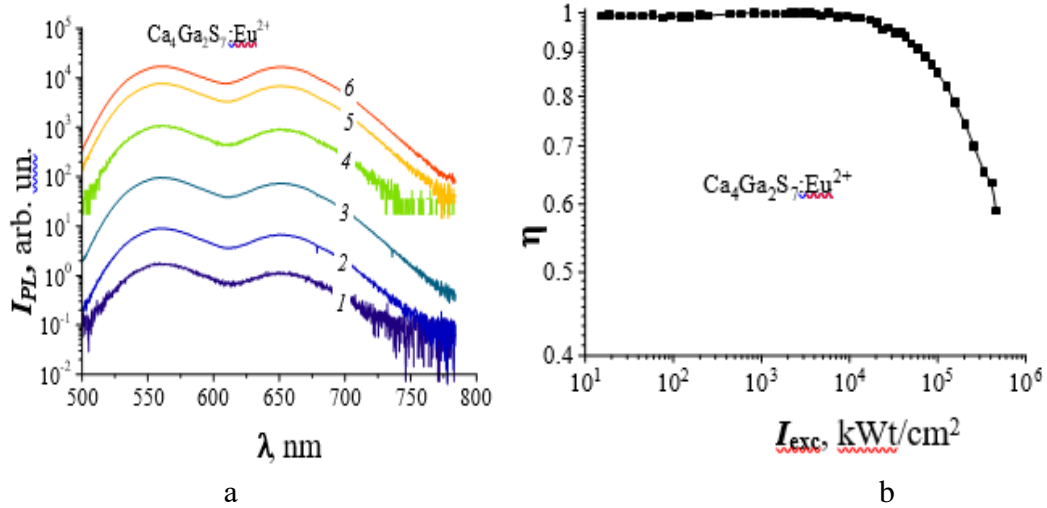
Fig.4. PhL spectra of $Ca_4Ga_2S_7$:Eu^{2+} compound at different excitation intensities 10 (*1*), 10^2 (*2*), 10^3 (*3*), 10^4 (*4*), 10^5 (*5*), 2.2·10^5 Vt/cm^2 by LD radiation on wave length 405 nm (a) and dependence of PhL integral intensity on excitation level at 300 K (b).
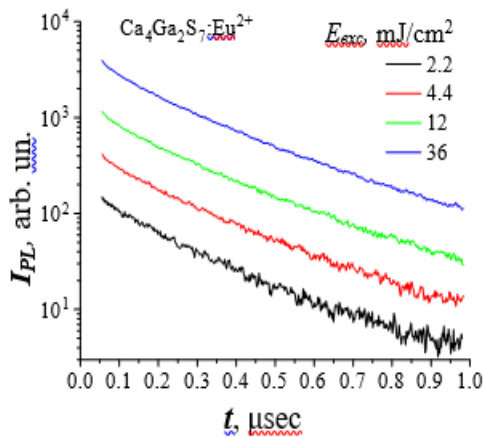
Fig.5. PhL damping kinetics of $Ca_4Ga_2S_7$:Eu^{2+} compound at temperature 300K and excitation different levels by impulse radiation of Yb:KYW-laser with duration 140fsec on wave length 260 nm.

CONCLUSION

It is shown that $Ca_4Ga_2S_7$:Eu^{2+} (radiated in yellow-red range) is the high-efficiency luminophors at excitation by UV-blue radiation of LD and LED (Light Emitting Diode) and have the high stability of the form and position of PhL spectrum in the excitation level interval up to ~10^4 Vt/cm^2 with further reversal PhL efficiency decrease that makes them perspective ones for the use in the capacity of luminophors excited by radiation of commercial AlGaN and InGaN lasers and light-emitting diodes for formation of sources of coherent and non-coherent radiation of "white" color with high values of colored characteristics [14 – 16].

_____

[1] *X. Wu, D. Carkner, H. Hamada, I. Yoshida.* Large-screen Flat Panel Displays based on Thick-Dielectric Electroluminescent (TDEL) Technology SID, 2004. vol. XXXV, Book II.-pp.1146-1149.

[2] *B.G. Tagiyev, S.A. Abushov, O.B. Ragiyev.* Journal of Applied Spectroscopy, 2010, vol.77, pp.124 – 128.

[3] *R.B. Jabbarov, C. Chartier, B.G. Tagiev, O.B. Tagiev, N.N. Musayeva, C. Barthou.* Benalloul P., Journal of Physics and Chemistry of Solids, 2005, vol. 66, № 6, p.1049-1056.

[4] *A.N. Georgobiani, V.V. Sturov, V.I. Tyutyunnikov, B.G. Tagiev, O.B. Tagiev, R.B. Jabbarov.* Journal of Physics and Chemistry of Solids. 2003. vol. 64. № 9-10, pp.1519-1924.

[5] *P. Benallol, Carlos Barthou, C. Foussier, A.N. Georgobiani, L.S. Lepnev, Y.N. Emirov, A.N. Gruzintsev, B.G. Tagiev, O.B. Tagiev, R.B. Jabbarov.* Journal of the Electrochemical Society.2003. 150(1). G62-G65.

[6] *B.G. Tagiyev, O.B. Tagiyev, R.B. Jabbarov, U.F. Kasumov, N.N. Musayeva.* New Technologies-21 century, №2, 58, 1999.

[7] *SeishiLida, Tamao Matsumoto, N. Mamedov, O. Tagiev, A. Bayramov, R. Jabbarov, B. Tagiev.* Jpn,J. Appl. Phys.1997, vol 36, pp. 857- 859, part 2, N7a.

[8] *A.N. Georgobiani, B.G. Tagiev, O.B. Tagiev, R.B. Jabbarov, N.N. Musaeva, U.F. Kasumov.* Jpn. J. Appl. Phys., 2000, vol., 39, № 39 -1, pp. 434 – 439.

[9] *P. Benalloul, C. Barthou, J. Benoit.* Appl. Phys. Lett., 1993, 63(14), pp. 154-156.

[10] *B.G. Tagiyev, O.B. Tagiyev, R.B. Jabbarov, U.F. Kasumov, N.N. Musayeva.* Photoluminescence of $Ca_4Ga_2S_7$:RRE. Inorganic mat.2001, vol.17, №12, pp.1430-1434.

[11] *B.G. Tagiyev, U.F. Kasumov, N.N. Musayeva, R.B. Jabbarov, A.S. Abushov.* Optical properties of $Ca_4Ga_2S_7$:Eu^{2+} compound, PTS, 2000, vol.34, №.10, pp. 1170-1172.

[12] *M.R. Davolos, A. Garcia, C.F. Fousser, and P. Hegenmuller.* Luminescence of Eu^{2+} in Strontium and Barium Thiogallates. J. Solid State Chemistry, 1989, 83, p. 316-323.

[13] *B.D. Urmanov.* Photoluminescence of chalcogenide semiconductors $Ca_{0.5}Ba_{0.5}Ga_2S_4$:Ce^{3+}, Sm^{3+} and $Ca_4Ga_2S_7$:Eu^{2+} in wide interval of excitation levels by study of InGaN-laser / B.D.Urmanov and others, Collected articles of 12th Belorussian-Russian seminar, Semiconductor lasers and systems on their base, 2019, pp.170 – 173.

[14] *B.D. Urmanov.* Increase of color rendering index value of standard white light-emitting diodes because of filling of spectral notches in blue-green and red regions. B.D.Urmanov and others. Collected scientific articles of I international scientific-technical conference "OPTO-MICRO- and MICROWAVE-ELECTRONICS, Minsk, October, 22-26, 2018, pp.44-47.

[15] *B.D. Urmanov.* The improvement of white light quality of radiation sources on the base of light-emitting diodes and luminophor mixture. B.D.Urmanov, V.A.Shulenkova, M.S.Leonenya "Modern problems of physics – 2018": Proceedings of VIII international school-conference of young scientists and specialists, Minsk, 2018, pp.169-172.

[16] *B.D. Urmanov.* White light source with high values of color characteristics on the base of InGaN-LED and luminophors mixture $BaGa_2S_4$:Eu^{2+}, $CaGa_2S_4$:Eu^{2+}и $(Ca,Sr)_2Si_5N_8$:Eu^{2+} / B.D.Urmanov and others, Theses of reports of XV International scientific conference Youth in Science, 2018, Minsk, 2018, p.163.

INFLUENCE OF POLARIZATION PROCESSES ON POLYMER ELECTRIC STRENGTH

I.K. ALIYEVA

Azerbaijan State Marine Academy, Az 1000, Z.Aliyeva str.,18, Baku, University
iradealiyevakerim@gmail.com

The distributions of breakdown waiting time (measured as electric durability τ) of polymers in constant field on sign in two directions (polarity) are determined and τ of polymer samples treated by preliminary polarization is also measured. It is shown that preliminary polarization of the samples in constant electric field decreases their electric strength at influence of the field of the same polarity. This fact evidences about cumulative nature of preparation process to breakdown and increases the electric density for the field of the opposite polarity. This indicates the ability to regeneration of "elements of destruction" caused by field action.

INTRODUCTION

The polymer films are widely used in the capacity of isolated materials in the different industries. That's why the investigation of their electric strength properties is the actual task. In spite of the fact that the study of influence of strong electric fields on polymer fields has continued many decades [1], the conventional point of view on nature of polymer electric strength is absent.

Many authors suppose that the formation of cavities of micron sizes in polymer in which the gas discharges can be formed is the reason of breakdown of polymer film under action of electric field. Note that gas discharges in cavities with sizes less 5mm don't form in the fields usually used in the experiments on study of polymer durability, i.e. in the fields with strength $E \sim 10^8$ V/m [1,2]. It is accepted that cavities appear as a result of molecule destruction [3-5]. At this fact it isn't considered that interatomic bond strength in macromolecule essentially exceeds σ stress which can act in dielectrics in electric field. Moreover, the macromolecule destructions can't lead to cavity formation as the material density at bond breakage doesn't change.

It is established that breakdown itself is the final act of polymer preparation process to breakdown appearance for polymer dielectrics. The experiment results on revealing and study of "electric durability" τ, which is breakdown waiting time at application to polymer samples of electric field strength E (constant or alternative ones) [6 – 8]. τ means that processes preparing the samples to breakdown take place in polymers under field action. From this it is followed that process consists of succession of some elementary acts the waiting time of which defines the process temps. Elementary acts leads to formation of local changes which are conventionally called "destruction elements". The accumulation of these elements for τ time forms the conditions of nucleation and development of magistral breakdown. Thus, the durability is the electric strength characteristics including the preparation process kinetics.

It is shown that under electric constant field action this process is the cumulative one and consists in constant formation in polymer of volume electric charge, the reach of some critic value of which leads to the breakdown [8 – 10]. So, the charge formation is the factor decreasing the electric strength. At the same time it is shown that accumulated charges can be eliminated (by heating of the samples or action of opposite polarity electric field) and thus one can carry out the regeneration of initial polymer strength state [8,9]. Thus, the possibilities of manipulation of polymer charge-strength state take place.

The polarization effect is the one of most essential electron processes causing the main peculiarities of electric structure of ionizing states as it defines the intrinsic energy of charge carrier and state of conduction levels in energy scheme of ionized states.

The study of polarization process influence on polymer electric strength and possibility to use the manipulation of accumulated charges as increasing factor of electric durability of polymer dielectrics is the aim of the given work.

OBJECTS AND INVESTIGATION METHODS

The films of polyethylene terephthalate (PETP) and polytetrafluorethylene (PTFE) with width in several decades of micrometers are the objects. Electrical load and breakdown are carried out in the cells with pressure electrodes with 18mm diameter at electric voltage by constant sign. The durability τ which is the time between moment of electric field application and breakdown appearance is measured. The test results of the similar type for electric destruction of solid states including the polymers are described in [10]. Note that qualitative analysis of test results is carried out without necessary taking under consideration of durability statistics.

As it is known [6,7], the durability values for externally identical samples and conditions of electrical load (electric strength E, temperature T) differ by wide spread (1–2 decade order on durability). That's why the corresponding statistical service of this

circumstances for the revealing of regularities of electric destruction kinetics.

EXPERIMENTAL RESULTS

The carried out investigations are dedicated to consideration of elementary processes taking place in polymer dielectrics in constant electric field which control the preparation of (breakdown) electric destruction kinetics. The breakdown preparation process in polymers being in electric field follows

from test results at constant and alternative field action. The distribution of series from 30 samples of PETP and PTFE on durability is given in Fig.1 (a,b), n_τ/n ratio is on ordinate axis where n_τ is sample number disruptive during τ time, n is total sample number. It is seen that curve of integral distribution on lgτ has S – type form that corresponds to unimodal distribution close to normal one (probability integral). The data for two directions (polarities) of applied field at constant values of E and T are given in Fig.1(a,b).
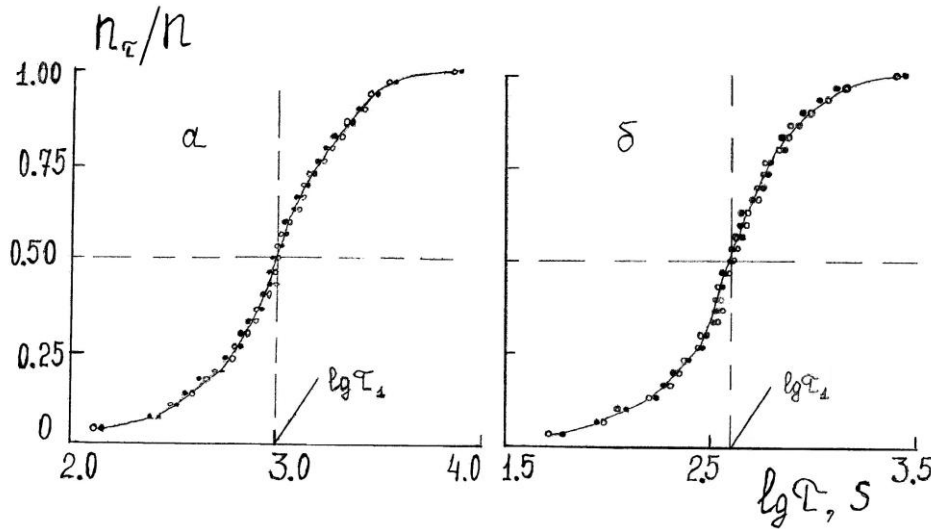

Fig.1. Integral distribution of polymer samples on electric durability in constant electric field. Light and dark points correspond to opposite field polarities. Temperature 100K.
  a is - PETP, E=0.62 GV/m
  b is - PTFE, E=0.46 GV/m

The distributions practically coincide with each other that establish the symmetry of test cell (diameter of electrodes is 18mm). The last fact will be the essential one at further manipulations.

τ_1 durability values (τ_1=1000sec for PETP, τ_1=400sec for PTFE) corresponding to breakdown of half sample number are defined from Fig.1 (a,b), i.e. during this time the breakdown of half number of electrically loaded samples, takes place. Thus, new series of the same samples are taken and endured at the same voltages and temperature during time τ_1 after which the voltage is taken. As a result, the half of sample number in series treated by field action but "not waiting" the breakdown stay not disruptive ones with which the further operations are carried out.

ANALYSIS AND RESULT DISCUSSION

The meaning and analysis technique of these operations is schematically explained in Fig.2. Here curve 1 is supporting curve corresponding to distribution by durability of second half of sample number in Fig., i.e. which have the durability bigger than τ_1. If after exposure τ_1 and voltage taking off, the accumulated changes are totally saved, so after repeatable field action of the same value and sign, distribution of residual samples on secondary

durability τ_2 should take place left than curve 1, i.e. in the form of curve 2. Such position of curve 2, which is absent to reconstruction of curve 1 in lg(τ-τ_1) coordinates should correspond to total absence of regeneration.

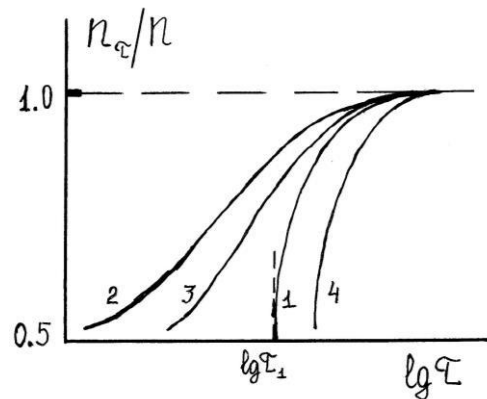*Fig.2.* Distributions on durability. 1 is distribution of not disruptive samples after exposure during τ_1 time; 2 is the same distribution in lg(τ- τ_1) on secondary durability (after interruption) at regeneration absence; 3 is distribution on secondary durability of the same samples at partial regeneration; 4 is distribution on secondary durability of the same samples at their strengthening.

If for the time of interruption of the same sign field action the changes in the rest samples are carried out or decrease of accumulated changes cause by temperature and opposite polarity field action, then the distribution on secondary durability should take place between curves 2 and 1 (curve 3).

The overlapping of the curve 3 on the curve 1 takes place at the total regeneration. Finally, for example, if the strengthening changes take place as a result of switching of the field in the samples, then distribution on secondary durability should take place right than curve 1 (curve 4).

The data correspond to experimental observation of curves 2 and 3 for the series of polymers are given in [8,9]. In this case, the samples are put for some time τ_1 in the field (the part of them are disrupted), further the voltage in interval time (τ_n) switches off and switches on again. The "secondary durability" (τ_2) which is the electric durability of not disruptive samples for τ_1 time beginning from the moment of second voltage switching on, is measured. The secondary durability of the samples is defined after changing temperature at definite time; τ_1 value corresponds to breakdown of half of samples. It is revealed that sample distributions on secondary durability shift in the region of least values τ in comparison with distributions in the tests without breaking of field action. Consequently, the sample exposure under voltage during time τ_1 leads to consumption of structural strength part. This evidences about the fact that breakdown preparation process takes place in electrically loaded polymers. As a result the changes which aren't totally regenerated during time τ_n accumulate in the samples during time τ_1, i.e. they show that changes accumulated in the samples for time τ_1 save if in interruption the sample doesn't heated or it isn't treated to action of opposite polarity field.

The distribution of polymer samples on secondary durability defined in tests with breaking of field action closes to distribution on durability in tests without breaking of field action, if for time τ the samples are heated or they are treated in opposite polarity field. This means that change regeneration accumulated in polymer samples for time τ_1 takes place at heating and in the opposite polarity field. Especially this fact (data on opposite polarity field regenerating action) leads to conclusion that sample preparation process to breakdown is connected first of all with formation of volume electric charges (rapidly, with electron accumulation in traps). So, the question arises: can this process lead not only to approach of electric stability losses (i.e. to breakdown approach), but to increase of electric stability.

This question is solved by following simple method. The series of samples (30) are treated under action of electric field of constant sign (E=0.62 GV/m for PETP and E=046 GV/m for PTFE) for the given polarity during time τ_1 (τ_1=1000sec for PETP, τ_1=400sec for PTFE). Further, the rest half of sample number at the same temperature (T=100K) are treated under field action of the same strength of opposite polarity, correspondingly for PETP and PTFE until appearance of sample breakdown. The distribution of this sample part on their secondary durability is shown in Fig.3. (a,b) (curve 2). It is shown that shift of distribution curve right from supporting curve 1 takes place, i.e. to the side of electric durability increase. Thus, it is experimentally established that samples previously polarized in the field of the one polarity are more electrically strength ones in respect of the opposite polarity field.

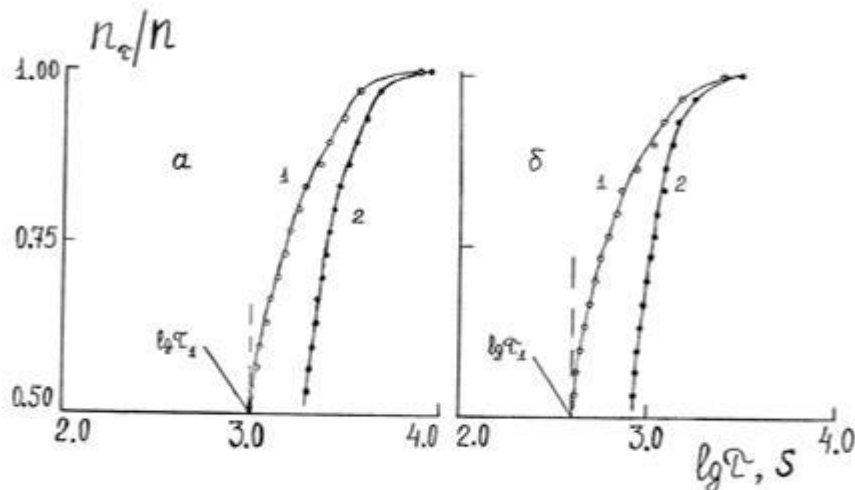*Fig.3.* Integral distribution of polymer samples on electric durability. Temperature is 100K.
   a is PETP, E=0.62 GV/m
   b is PTFE, E=0.46 GV/m
   1 - is distribution of disruptive samples after exposure during τ_1(τ_1=1000C for PETP, τ_1=400C – for PTFE) without the change of filed polarity
   2 - is distribution of disruptive samples after exposure during $\tau_1$time with change of filed polarity after it.

The results of polarization strength of polymer samples are obtained in the tests of another type on PTFE films. With this aim the dependence of breakdown waiting time (durability) on constant electric field strength of the given polarity is measured. The results of such measurements for T=293K are given in Fig.4 (dependence 1). Each point in graph is the result on averaging by 12 durability measurements at each value of field strength.

Many series of the same samples are treated by previous action of constant electric field of strength E=0.038 GV/m during 1 hour at 380K. Further, the electric durability of such samples at 293K at the both field polarity and opposite one is measured. If field polarity coincides with field polarity of previous polarization, then decrease of sample electric durability is observed (Fig.4., dependence 2). Vice versa, if the polarity is opposite one, then sample electric durability increases (Fig.4, dependence 3) and exceeds the durability of initial samples (not treated by previous polarization). The corresponding data for PETP are the similar.
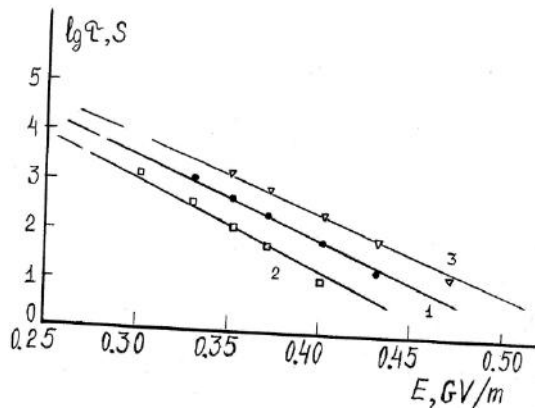

Fig.4. The dependence of PTFE durability on electric field strength (by sign). Temperature is 293K. 1 is durability of the samples without previous polarization; 2,3 are disabilities of the samples after exposure in constant field E=0.038 GV/m during 1 hour at 380K; 2 is durability of the disruptive samples in the field of the same polarity; 3 is the durability of the disruptive samples in the field of opposite polarity.

Thus, previous polarization of polymer samples in constant electric field decreases their durability at action of opposite polarity and increases the durability for opposite polarity field. The similar behavior of electric durability coincides with consumption of charge accumulation in polymer volume. The durability reduction (after some film exposure under voltage) up to primary value takes place at polymer heating or its placing for some time in electric field of opposite polarity. This means that the discharge of accumulated charge in the field of opposite polarity at heating takes place. Such operation leads even to that the electric durability of polymer films in field of opposite polarity (after action of initial field) is the highest than in continuously acting field. The durability estimations of polymer film carried out on the base of such consumptions in constant electric field is in the agreement with experimental data [8].

At transfer of described polarization phenomena on electric ones, the polymer destruction in alternating field should be expected for the polymers with continuous durability. However, as it is well known [11,12] in alternative field the breakdown takes place even rapidly than in constant one (at equality of amplitude strength values of alternative and electric fields), i.e. electric strength of polymer dielectrics in alternative electric field is essentially lower than in constant one [13] and in particular, it is known, that polymer durability in alternative field approximately on two orders less than durability value in constant field [14-16]. Thus, the revealing of general and specific moments in mechanisms of electric destruction for constant and alternative fields has the more actuality.

Finally, the possibility of technical use of "electret" strengthening of polymer dielectrics can serve the subject of further development.

CONCLUSION

The regeneration of electric density properties of polymer dielectric films after previous polarization which are reconstruction and strengthening of electric durability by the way of heating or action of opposite polarity field is studied. On the base of regeneration kinetics analysis the conclusion that regeneration is caused by discharge of volume charges, is made. This means that previous polarization of polymer films in them takes place and the binary volume charges (of double electric layers), i.e. polarization heterocharges, form.

[1] *L.A. Diddado, J.C. Fothergill.* Electrical Degradation and Breakdown in Polymers. Pater Peregrinus, London. 1992. pp 589.

[2] *M.A. Bagimov, V.P. Malin, S.A. Abbasov.* The influence of electric discharges on polymer dielectrics, Baku, Science, 1975, p.168.

[3] *N.R. Tu, R.C. Rao.* Ybgt-field electrical conduction in polyimide films. J.Appl. Phys. 1999, v.85, №10, p.7267-7267.

[4] *D. Liufu, X.S. Wang, D.M. Tu, K.C. Kao.* High-field electrical aging in polypropylene films. J.Appl. Phys., 1998, v.83, №4, p.2209-2214.

[5] *Z. Li, Y. Yin, X.S. Wang, D.M. Tu, K.C. Kao.* Formation and Inhibition of Free Radicals in Electrically Stressed and Aged Insulating Polymers. J.Appl. Polymer Sci 2003, v.89, p.3416-3425.

[6] *V.A. Zakrevski, N.T. Sudar.* Electric destruction of thin polymer films. PSS, 2005, vol.47, №5, pp.931-936.

[7] *V.B. Berejanski, B.M. Bikov, V.V. Gorodov, Zakrevski, A.I. Sluzker.* Electric durability of polymers at the absence of partial discharges, JTP, 1985, vol.55, № 8, pp.1663-1666.

[8] *I.K. Aliyeva, T.M. Veliyev.* Kinetics of mechanic and electric destructions of polymers, Baku, ASMA, 2018, p.192.

[9] *A.I. Sluzker, T.M. Veliyev, I.K. Aliyeva, V.A. Alekperov, S.A. Abbasov.* Cumulative processes in kinetics of mechanical and electric destructions of polymers. PSS, 1990, vol.32, №8, pp.2339-2344.

[10] *A.I. Sluzker, Y.I. Polikarpov, D.D. Karov.* On elementary acts in kinetics of electric destruction of polymers, JTP, 2006, vol.76, № 12, pp.52-56.

[11] *G.A. Vorobyev, S.G. Ehanin, N.S. Nesmelov.* Electric breakdown of solid dielectrics. PSS, 2005, vol.47, № 6, pp.1048-1052.

[12] *M. Nikita, S. Tajima, I. Kanno, G. Sawa, M. Ieda.* Higt-Field Conduction and Electrical Breakdown of Polyethylene at High Temperatures. Jpn. J.Appl. Phys., Pt.1. 1985, v.24, №8, p.988-996.

[13] *Abdelkrim Laifaoui, Mohend Seghir Herzine, Youcef Zebboudj, Jean-Micel reboul, Mohammed Nedjar.* IEEE Trans. Dielectr. Electr. Insul. 21, 2267 (2014). DOI:10.1109/TDEI. 2014. Oo4190.

[14] *T.M. Veliyev.* Role of charged particles and relaxation phenomena in the process of electric and mechanical destructions of polymer dielectrics in strong electric field. PhD thesis of phys-math science, Baku: 1986, p.161.

[15] *V.A. Zakrevskii, A.I. Sluzker.* Electric aging of polymer dielectrics at suppression of partial discharges. High-molecular compounds, 1986, vol.28 (A), №10, pp.2163-2169.

[16] *G. Mazzanti, G.C. Montanari, L.A. Dissado.* IEEE Trans. Dielec. Electr. Insul. 2005. 12, 876. DOI: 10.1109/TDEI. 2005. 1522183.

STRUCTURAL PHASE TRANSITIONS IN $Cu_3Ni_{0.5}Se_2$ CRYSTALS

G.M. AGAMIRZOYEVA, N.A. ALIYEVA

Institute of Physics of ANAS, AZ1143, H. Javid ave., 131, Baku, Azerbaijan
e-mail: nergiz_25@mail.ru

The compound of magnetic semiconductor of $Cu_3Ni_{0.5}Se_2$ composition is synthesized. The parameters of low-temperature phase are determined and the structural-phase transitions are investigated by high-temperature X-ray diffraction method. It is established that synthesized $Cu_3Ni_{0.5}Se_2$ is two-phase one at room temperature and it consists of rhombohedral and cubic phases with parameters a=4,321Å, c=20,620Å and a=11,841Å correspondingly. It is determined that the rhombohedral phase disappears and cubic superlatice saves in temperature interval 293<T<773 K at T=462±3K in two-phase system. At temperature T=665K the cubic superlatice transforms into cubic subcell with parameters a=5,94 Å, V=209.58 Å^3, sp.gr. $Fm\bar{3}m$, Z=4.

Keywords: crystalls, structure, phase transitions, modifications.
PACS: 64.60.-i

INTRODUCTION

It is known that thermomagnetic and thermoelectric materials with small lattice thermal conduction and high mobility of charge carrier have the wide field of use [1 – 4]. The so-called superion chalcogenides Ag, Cu and different solid solutions on their base belong to number of such materials [5 – 7]. It is obvious that the presence of experimental data on external factor influence on their structure is necessary for effective use of these materials. Note that for the given materials the polymorphous transformations under temperature influence is the one of the character properties. Indeed, the determination of equilibrium temperature between possible polymorphous modifications, temperature interval existence and structures of these phases has the big scientific and practical value.

The investigation results of structural-phase transitions of $Cu_3Ni_{0.5}Se_2$ composition solid solution in temperature interval 293-800K are given in present work.

EXPERIMENTAL PART

The physico-chemical characteristics of natural and synthetic umangite Cu_3Se_2 described in works [8 – 10] is the stimulus for $Cu_3Ni_{0.5}Se_2$ synthesis. It is seen that in such recording of chemical composition the valency balance isn't carried out and open composition should be in the form $Cu_2^{+1}Cu^{+2}Se$. For explanation of this statement we have made the attempt to obtain the full-valent solid solution by the way of implantation of Ni atom into Cu_3Se_2 composition. $Cu_3Ni_{0.5}Se_2$ is synthesized from Cu, Ni and Se elements the purity of which isn't less than 99.999 in evacuated~ 10^{-4} millimeter of mercury in quartz ampoules in inclined furnace (~15^0). Ampoule of length ~20 cm with substance (5 gr.) is gradually put into furnace the temperature of which is previously established in point 1250K. After total immersion of the ampoule the furnace temperature is increased up to T=1370 K and it is endured at the given temperature during 2,5 hours. Further the furnace temperature is decreased up to 700K and the ampoule is endured at this temperature

during six days for homogenization. The synthesized and annealed sample is the compact alloy of dark grey color and its powder has black color.

INVESTIGATION OF PHASET RANSFORMATIONS

All temperature experiments on revealing of structural-phase transitions in crystal of $Cu_3Ni_{0.5}Se_2$ composition are carried out in Institute of Physics of ANAS on powder diffractometer «D8 ADVANCE» («Bruker») in vacuum (10^{-2} torr) in temperature interval 293<T<700K at mode 40 кV, 40 мА, CuK_{α}-λ=1.5406Å, 10<2θ<80^0.

For this purpose, from the synthesized sample $Cu_3Ni_{0.5}Se_2$ the fine-dispersed powders are prepared and the diffractogram at temperature 300K (Fig.1) is obtained.

The treatment of the obtained diffraction picture, i.e. the indicating of interplanar spaces (d) with the use of calculative program TOPAS 4.2 shows that synthesized material at room temperature is the two-phase one and it consists of rhombohedral phase with lattice periods on hexagonal axes a_h=4.32 Å, c_h=20.60 sp.gr. $R\bar{3}m$, Z=9 and cubic phase with parameter a=11,841 Å, sp.gr. Pa-3, Z=32. The obtained X-ray diffraction data are given in Table 1, where ▲ is rhombohedral phase and ■ is cubic phase.

After definition of the main crystallographic parameters of low-temperature phase, we carry out the high-temperature investigations of the same sample in the mode of low-temperature variant. Whole investigation process is regulated in automatic mode. X-ray diffraction pictures at temperatures 293, 400, 500, 600, 700 K are obtained. At give temperatures the sample is endured during 25 minutes and the picture is taken after it.

The visual comparison of obtained temperature diffraction pictures and the treatment of separate peaks and whole diffractograms using TOPAS and EVA programs shows that the essential changes aren't observed in $Cu_3Ni_{0.5}Se_2$ structure in temperature interval 293-500K besides the decrease of initial peak intensity. The essential changes in sample diffraction picture is observed in point 500K. If we compare the

diffraction spectra in the given temperature, then it is revealed that at T= 500K the initial peak intensity $2\theta=13,125^0$ increases and reflections of double peak $2\theta=26,20^0$ and $26,53^0$, $43,35^0$, $44,00^0$ peaks of low-temperature phase damp. Simultaneously, the intensities of new reflections at $2\theta=26,68^0$ and $44,02^0$ strong increase.

The given experimental facts evidence that the structural change takes place in the sample near T=500K. By treatment of these diffraction pictures using the above mentioned programs it is established that the picture observable near 500K shows that all images of rhombohedral phase in the given temperature disappear and the system transforms into one-phase state with primitive cubic structure (Table 2). The lattice parameters of this phase are following: $a \approx 11,8684$ Å, sp.gr.-$Pa\overline{3}$, Z=32.

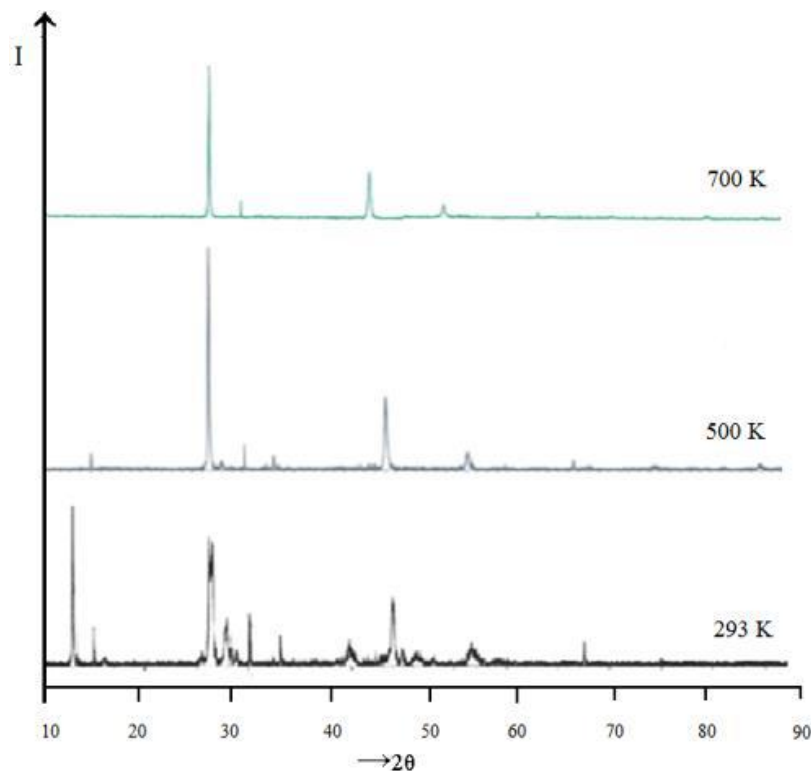*Fig. 1*. Cu₃Ni₀.₅Se₂ diffractograms in different temperatures 293K, 500K, 700K.

Table 1.
X-ray diffraction data of Cu₃Ni₀.₅Se₂ at temperature 293K.

№	d	I/I₀	hkl
1	6.77348	20	003▲
2	5.90905	1.5	200■
3	5.51234	10	100▲
4	3.51229	2	311■
5	3.39444	100	006▲
6	3.19555	17	312■
7	2.96211	3	400■
8	2.77339	6	330▲
9	2.70852	4	331■
10	2.26410	14	009▲
11	2.06174	60	440■
12	2.02388	11	441■
13	1.95728	7	600■
14	1.90273	3	611■
15	1.76240	11	200▲

▲ is rhombohedral phase with lattice parameter a=4.32 Å

■ is cubic phase with lattice parameter a=11,841 Å

Table 2.
X-ray diffraction data of Cu₃Ni₀.₅Se₂ at temperature 500K.

№	d	I/I₀	hkl
1	5,8984	18	200
2	3,3451	100	222
3	3,1989	7	321
4	2,9612	20	400
5	2,7102	10	330
6	2,0527	36	440
7	1,7519	12	622
8	1,6467	3	710
9	1,4639	7	800
10	1,3332	5	554
11	1,1188	5	910

The diffraction picture in comparison with intermediate cubic phase is significantly simplified with further temperature increase up to 700K. The part of weak reflections disappears and the intensities of neogenic peaks increase. By treatment and definition by auto-indicating program TOPAS of this phase diffraction data it is established that the primitive cubic superlatice with parameter a=11.684 Å at T=700K

transforms into face-centered cubic (FCC) phase with parameters a=5,96 Å, sp.gr. $Fm\overline{3}m$, Z=4 (Table 3).

Table 3.

X-ray diffraction data of $Cu_3Ni_{0.5}Se_2$ at temperature 700K.

№	d	I/I₀	hkl
1	3,34862	100	111
2	2,05061	43,5	220
3	1,74876	9,6	311
4	1,67431	0,6	222
5	1,45000	0,5	400
6	1,33061	1,5	331
7	1,29692	1	420

Correcting the equilibrium temperature between polymorpous modifications by extinction method and appearance of diffraction reflections (at increase and decrease of the temperature) it is established that rhombohedral α-phase of $Cu_3Ni_{0.5}Se_2$ at T=560±3K room-temperature two-phase system transforms into cubic β-phase (a=11.8844 Å) of $Pa\overline{3}$ symmetry.

CONCLUSION

As it is mentioned above, authors [5] show that Cu_3Se_2 umangite forms at interaction of $Cu_{2-x}Se$ and CuSe at temperature 408K. It decomposites on $Cu_{2-x}Se$ и CuSe at heating higher T=408K. Note that results of the given investigation of phase transitions show that implantation of Ni atoms into umangite increases $Cu_3Ni_{0.5}Se_2$ stability and it is stable up to T=567 K. Higher this temperature the cubic superlatice transforms into FCC lattice with parameter a=5,96 Å. One can suppose that the implantation of Ni bivalent atoms in umangite composition prevents the oxidation of Cu atoms up to bivalent state.

_____

[1] *V.V Qorbacev.* M.: Metallurqiya, (1980), p.132 (In Russian).

[2] *M.Kh. Balapanov, R.A.Yakshibayev, U.Kh. Mukhamedyanov.* PSS, 2003, vol. 45, № 4, pp. 604–608.

[3] *S.A. Aliyev, F.F.Aliyev.* PTS, 2003, vol. 42, № 4, pp. 404–408.

[4] *S. Kashida, W. Shimosaka , M. Mori, D. Yoshimura.* Journal of Physics and Chemistry of Solids 64, (2003), pp. 2357-2363.

[5] *N.Kh. Abrikosov, V.F. Bankina, L.V. Poretskaya and E.V. Skudnova.* Nauka, Moscow, 1975, p.220.

[6] *V.M. Glazov, A.S. Pashinkin, V.A. Fedorov.* Inorganic Materials, 2000, vol.36, №7, pp. 641-652.

[7] *R.D. Heyding, R.M. Murray.* Canadian Journal of Chemistry, 1976, vol. 54, №6, pp. 841-848.

[8] *N.A. Əliyeva, G.F. Qənizadə, Q.H. Hüseynov, F.F. Yəhyayeva.* Fizika Jurnalı, 2017, vol. XXIII, №3, pp. 24-27.

[9] *A.L.N. Stevels.* Philips Res. Rep. Suppl., 1969, №9, p.124.

[10] *A.L.N. Stevels, G.A. Wiegers.* Recl. Copper telluride, Trav.Chim.Pays-Bas 90, 1971, p.352.

[11] *K. Koto , N. Morimoto.* Acta Crystl. 1966, vol. 152, p. 915.

BANDGAP RENORMALIZATION OF THE InSe BY LASER RADIATION

A.H. KAZIM-ZADE[1], V.M. SALMANOV[1], A.G. GUSEINOV[1], R.M. MAMEDOV[1], S.S. RAGIMOV[1,2], I.I. QURBANOV[2], V.N. JAFAROVA[2]

[1] *Baku State University, Baku, AZ1148 Azerbaijan*
[2] *Institute of Physics of ANAS, AZ1143, H. Javid ave., 131, Baku, Azerbaijan*
e-mail: vagif_salmanov@yahoo.com

Nonlinear absorption of light and its time evolution in InSe under the influence of picoseconds laser excitation have been investigated experimentally. It was shown that the decrease in exciton absorption in InSe at high levels of optical excitation due to the exciton – exciton interaction and screening of the Coulomb potential by free carriers, generated by laser light. Observations of induced absorption in the energy region between the exciton level and the edge of the conduction band are associated with the appearance of a continuum of states due to a shift in the edge of the energy band.

1. INTRODUCTION

As you know, the interaction of light waves of high power and high monochromaticity with matter, lead to the emergence of a new field of physics - nonlinear optics. In turn out that under sufficiently strong excitation the optical properties of basically all semiconductors exhibit nonlinear characteristics. They may give rise to effects such as excitation-dependent absorption and refraction, nonlinear wave mixing, optical bistability, harmonic generation, parametric light generation, multiphoton absorption, band filling, band renormalization, thermal nonlinearities, or other optical instabilities. Some of these effects have attracted considerable attention, since the may be useful for applications in optical switching devices, optical logic gates, or even optical computing. A variety of experimental methods have been employed to study mechanisms responsible for optical nonlinearities in the absorption spectra and to measure the nonlinear refractive indices in semiconductors. Pump-probe spectroscopy, nonlinear interferometry, beam-distortion measurements, four-wave mixing and phase conjugation are among these techniques [1–4].

InSe crystals belonging to III-VI compounds semiconductors have received considerable attention recently as an interesting class of nonlinear optical materials. Due to the layered structure, crystal structure features, high polarizability, optical uniformity, the presence of natural mirror surfaces, strong and broadband light absorption in a wide frequency range, the presence of exciton absorption with a fairly high binding energy (~ 25 meV), the possession of the band gap areas of generation of modern lasers, a variety of nonlinearity mechanisms and the existence of developed technology for producing perfect crystals makes InSe crystals popular in quantum electronics. This article is an experimental study of the renormalization of bands in InSe crystals at high levels of optical excitation.

2. EXPERIMENTAL METHODS

Indium selenide has a layered structure, where each layer contains two indium and two selenium close-packed sublayers in the stacking sequence Se-In-In-Se [5]. The bonding between two adjacent layers is of the Van der Waals type, while within the layer the bonding is predominantly covalent. The investigated InSe crystals were obtained by the Bridgman method. The ingot were cleaved along the planes of layers ($\perp$ to the c-axis), obtaining slices about 10-50 μm thick. Mobility and concentration of charge carriers measured by conventional methods at room temperature were μ_n ~1,2×10³ sm²/V·s and n=7×10¹⁴ sm⁻³, respectively.

In our experiments, we used a picosecond YAG: ND³ laser, generating light pulses of 25 ps duration, operating in the mode synchronization mode, as a light source. After amplification, the light pulse was split into two: the first, converted in the KDP crystal into a light pulse with a double frequency $\hbar\omega_H = 2,34 эB$), served as an excitation source, the second was converted into a light pulse with a wide spectral distribution when passing through a cell with heavy water (0.75 ÷1.5) μm. The time delay between the probe light pulse and the pump pulse was carried out by changing the path length of the pump pulse. The zero delay was determined by measuring the correlation function of the pump pulse and the probe pulse by m of up-conversion in a KDP crystal The spectral distribution of the probe pulse transmitted through the InSe sample was studied using an M833 automatic double-dispersion monochromator (spectral resolution ~0.024 nm at a wavelength of 600 nm), with a detector detecting radiation in the length range waves of 350 - 2000 nm, a storage oscilloscope ((Le Croy 9400) and a computer system (board Master 800 ABI 8). The exciton absorption spectra and the dynamics of nonlinear absorption of light were studied at T = 4.2 K using the pump-probe spectroscopy method. In this case, the crystal was excited by an intense light pulse $\hbar\omega$ = 2.34 eV and the absorption spectra were recorded using a probe pulse at different instants of time. The experimental setup is shown in Figure 1.
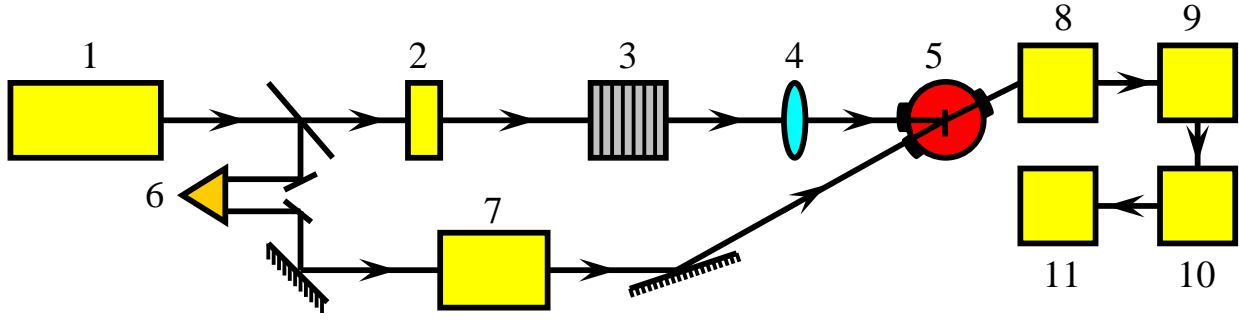
Fig. 1. Schematic of an experimental setup for measuring the transmission spectra of InSe crystals: 1-YAG: Nd^3 laser, 2-crystal KDR, 3-optical filters, 4-lens, 5-sample, 6- delay time, 7-cell with heavy water (deuteroxide), 8-monochromator, 9-detector, 10-oscilloscope, 11-computer system.

3. EXPERIMENTAL RESULTS AND DISCUSSION

Figure 2a shows the spectral dependence of the optical density of InSe crystals at various excitation intensities (there is a zero time delay between the pump pulse and the probe pulse). As can be seen from the figure, nonlinear absorption is observed in the exciton absorption region ($\hbar\omega = 1,336$ eV) and the sample is bleached at the indicated radiation frequency at high excitation levels. The observed bleaching is saturated at an incident light intensity of

~ 600 MW/sm^2. The characteristic absorption length of the pump radiation is $\ell = 1/\alpha = 10^{-4}$ sm, $\alpha = 10^4$ sm^{-1} for $\hbar\omega = 2,34$ eV.

Figure 2b shows the absorption spectra of InSe crystals for various time delays between the probe pulse and the pump pulse. A broadening of the spectral line and a shift in the maximum of exciton absorption to the region of high energies relative to the unexcited state are observed. In the energy region between the exciton level and the edge of the conduction band, induced absorption appears.
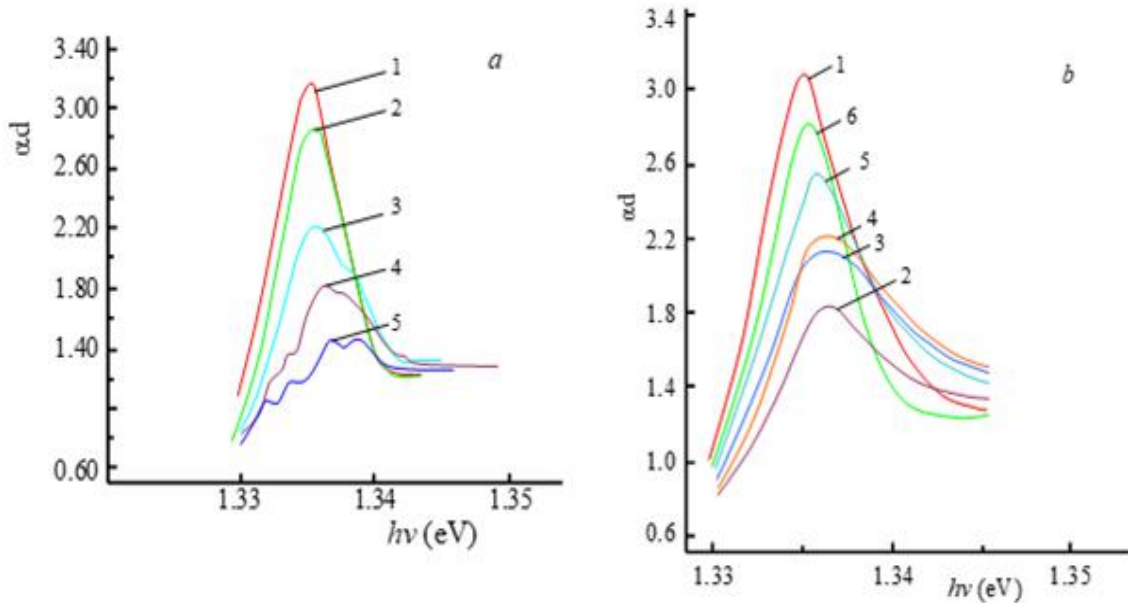
Fig. 2. a) absorption spectra of InSe at various excitation intensities I_{pump} (MW/ sm^2): 1 - 0, 2-12, 3-60, 4-250, 5-600 (there is zero time delay between the pump pulse and the probe pulse, $\Delta t = 0$) at T = 4.2K, b) absorption spectra of InSe for various time delays between the pump pulse and the probe pulse: 1 - $I_{pump} = 0$, 2 - $\Delta t = 24$ ps, 3 - $\Delta t = 98$ ps, 4 - $\Delta t = 297$ps, 5- $\Delta t = 660$ps, 6- $\Delta t = 910$ps, $I_{pump} = 600$ MW/sm^2, $\hbar\omega_{pump} = 2.34$ eV, T = 4.2 K.

The time dynamics of bleaching in the region of exciton absorption and induced absorption has its own characteristic features (Fig. 3, a, b). It was experimentally established that the bleaching in the exciton absorption region is characterized by a rise front in time of ~ 60 ps, and the decay has a fast and slow kinetics (Fig. 3, a). The kinetics of induced absorption in the energy region between the exciton

level and the edge of the conduction band is shown in Fig. 3, b. Note that at high excitation levels (I~600MW/sm^2), a probe pulse is amplified and the rise front is characterized by a time of ~ 60 ps. The maximum of the induced absorption is reached over the time of ~200÷300ps and with an increase in the pump intensity, shifts toward longer times.
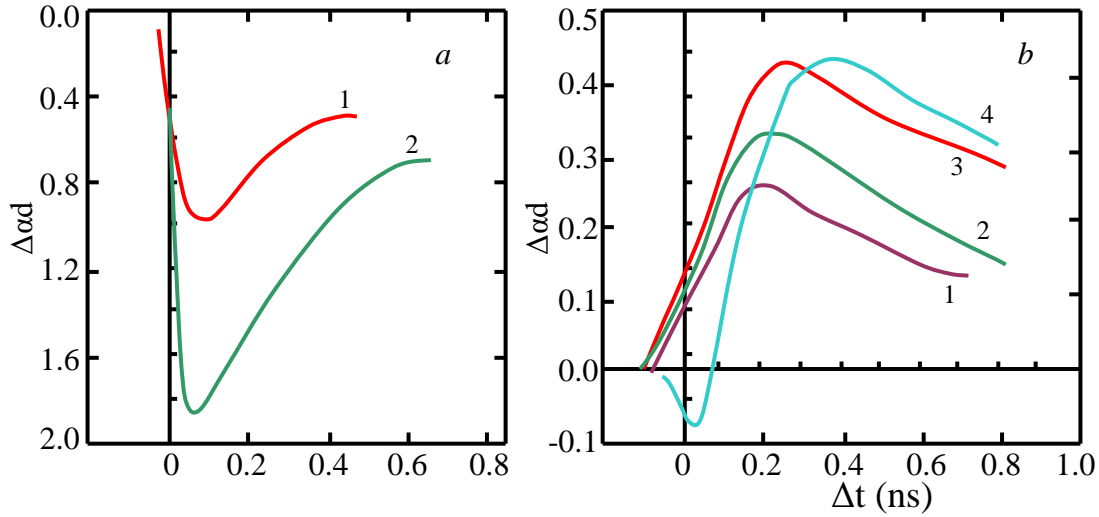
Fig. 3. Dependence of the optical density InSe on the delay time between the pump pulse and the probe pulse (Δt). a) at the maximum of the exciton absorption, $\hbar\omega_{probe}$ = 1.336 eV, $\hbar\omega_{pump}$= 2.34 eV, T = 4.2 K; 1- I_{pump}= 100 MW/sm², 2- I_{pump}= 200 MW/sm²; b) in the absorption continuum, $\hbar\omega_{probe}$ = 1.340 eV, $\hbar\omega_{pump}$ = 2.34 eV, T = 4.2 K; 1- I_{pump} = 100 MW/sm², 2- I_{pump} = 200 MW/sm², 3- I_{pump} = 300 MW/sm², 4- I_{pump} = 400 MW/sm².

In our opinion, nonlinear absorption is observed in InSe crystals at high levels of optical excitation in the exciton absorption region. The observed features in the InSe absorption spectra can be explained by the interaction of excitons and the screening of the Coulomb potential by free carriers generated by laser radiation. Indeed, when InSe crystals are excited by laser light, electrons and holes bind to excitons. Subsequently, with an increase in the excitation intensity, the density of excitons increases, and when it reaches a certain critical value, an interaction between excitons occurs, which leads to the decay of excitons and the formation of free electron-hole pairs. This phase transition is called the Mott criterion for excitons [6]

$$n_{Momm} = \frac{\pi}{3}(\frac{1,46}{4a_{экс.}}\frac{m_0}{m_e + m_h})^3 \qquad (1)$$

Knowing the effective masses of electrons and holes (m_e=0.7m_0, m_h =0.5 m_0), as well as the Bohr radius of the exciton $a_{ex.}$= 3.7 nm in InSe, we can calculate the exciton concentration, which turned out to be equal to $n_{Mott} \sim 2,5\times10^{16} cm^{-3}$. Experiments show that in InSe the density of pairs generated by laser light with an intensity of I_0=1,5x10²⁶ photon/sm² ·s, $\alpha \sim 10^4$ sm⁻¹ and duration of Δt=2,5x10⁻¹¹ s is

$$\Delta n = \alpha\ I_0\Delta t = 3,8x10^{19}\ sm^{-3} \qquad (2)$$

As can be seen from a comparison of formulas (1) and (2), the values of the concentration of nonequilibrium carriers obtained by us are three orders of magnitude higher than the exciton density required for the Mott transition.

We also determined the screening length of the Coulomb interaction by free carriers. The shielding length can be determined using the following formula [7]

$$L = \hbar/2(\pi/3)^{1/6} N^{-1/6} \frac{\varepsilon^{1/2}}{em^{*1/2}} \qquad (3)$$

where ε is the dielectric constant of the crystal, m∗ is the effective mass, and N is the concentration of the generated carriers.

Substituting the values of the corresponding parameters of InSe crystals, we find that the screening length L ~ 10A° is much smaller than the radius of the exciton. The Bohr radius of the exciton in InSe is ~ 37A°.

As can be seen from Fig. 2b, at a light intensity of I_{pump}~600MW/sm², the complete disappearance of the exciton absorption line was not detected. This, apparently, is associated with inhomogeneous excitation of the sample at $\hbar\omega_{pump}$=2.34eV. Thus, a situation is experimentally realized when both the electron-hole plasma (EHP) and the dense exciton gas are present in the sample.

Since the decrease in exciton absorption is due to the interaction of excitons and the screening of the Coulomb potential by free carriers, the increase in the transmission of the probe pulse should be proportional to the integrated pulse intensity, i.e. the rise time of enlightenment should be of the order of the pulse duration (see Fig. 3, a, b). On the other hand, the tightening of the leading front of enlightenment may be due to the diffusion of nonequilibrium carriers. Initially, the generation of free carriers occurs in a thin layer of ~10⁻⁴ sm, subsequently, electrons and holes diffuse deep into the sample, thereby reducing exciton absorption. The ambipolar diffusion coefficient in InSe is <10 sm²/s; therefore, the time scale of carrier redistribution due to diffusion over the sample is more than 1 ns, which indicates an insignificant effect of the diffusion process.

It seems that a rapid decrease in the bleaching (see Fig. 3, a) is mainly associated with recombination processes in the electron – hole pair and dense exciton

gas. Slow kinetics is possibly determined by the screening process of excitons of the direct zone by nonequilibrium carriers of the indirect zone (the lifetime of these carriers is $\sim 10^{-7}$ s).

Another consequence that exciton interaction and screening of the Coulomb potential by free carriers generated by laser radiation can lead to is a decrease in the bandgap or renormalization of bands in InSe at high levels of optical absorption. In our opinion, our observation of induced absorption in the energy region between the exciton level and the edge of the InSe conduction band is associated precisely with the appearance of a continuum of states due to a shift in the edge of the energy band (see Fig. 2, b)[8]. As a result of the renormalization of the forbidden zone the energies of the electrons and holes in their respective bands are reduced. This energy reduction is a consequence of the exchange effect for particles with equal spin and Coulomb correlation effect for all particles. The exchange effect is caused by the Pauli exclusion principle. The probability that two Fermions with identical quantum numbers are at the same point in real space is zero. For increasing separation between the particles, the probability slowly approaches unity. Hence, the Pauli exclusion leads to a reduction of the probability that equally charged particles come close to each other and this in turn reduces the repulsive (i.e., positive Coulomb energy) contribution. This situation for particles with equal spins is often described by the presence of an "exchange hole", where each Fermion is surrounded by a region where the probability for the existence of another identical Fermion is very small. Correspondingly, equally charged Fermions with different quantum numbers (e.g., electrons with different spins) avoid each other because of the Coulomb repulsion. As in the case of the exchange hole, this "Coulomb hole" also leads to a decrease of the overall energy.

A good approximation for the bandgap reduction is

$$\delta E_g = \sum_{q \neq 0} [V_s(q) - V(q)] - \sum_{q \neq 0} V_s(q)[f_e(q) + f_h(q)]]$$
(4)

where the first and second terms are called the "Coulomb-hole" and "screened-exchange" contributions, respectively. Here $V(q)$ and $V_s(q)$ are the Fourier transform of the unscreened and screened Coulomb potentials, respectively. The renormalized bandgap is then

$$E_g^/ = E_g + \delta E_g$$
(5)

with $\delta E_g < 0$ [the first term in Eq. (4) has a negative sign since the screened Coulomb potential is smaller than the bare Coulomb potential, $V_s(q) < V(q)$].

The bandgap shift when the concentration of excitons is high enough and their collective properties must be taken into account. More specifically, we are talking about such concentrations $n_{ex.}$, at which the value $(n_{эк.} \cdot a_{эк.}^3)^{1/3}$ begins to approach unity, i.e. the average distance between excitons becomes comparable with their radius. The bandgap shift depends on the distance r_s between two excitons

$$r_s \equiv \left(\frac{1}{n_{эк.} a_{эк.}^3} \frac{3}{4\pi} \right)^{1/3}$$
(6)

With decreasing r_s renormalization of zones increases.

We see that the screened exchange and the Coulomb-hole contributions both increase with increasing carrier density (decreasing particle separation). For low carrier densities, the dominating contribution comes from the Coulomb-hole term, whereas at elevated densities, both terms are equally important. An often useful approximation for the bandgap reduction has been derived in [9]

$$\frac{\delta E_g}{E_B} = E_{xc} + n \frac{\partial E_{xc}}{\partial n}$$
(7)

where E_B is the exciton Rydberg energy and

$$E_{xc} = \frac{4.8316 + 5.0879 r_s}{0.0152 + 3.0426 r_s + r_s^2}$$
(8)

Bandgap reduction leads to a monotonous red shift of the onset of the continuum absorption in semiconductors. At the Mott density the bandgap has shifted one exciton Rydberg energy below the zero-density bandgap E_g. For even higher densities, bandgap renormalization may cause increasing absorption in the spectral region below the exciton resonance. Whether such an increasing absorption is visible in an experimental spectrum depends on the magnitude of the bandgap renormalization versus the increasing chemical potential due to the bandfilling effect.

Qualitatively, the renormalization of zones can be explained as follows. Due to inhomogeneous excitation near the front surface, the density of nonequilibrium carriers is high and the Fermi level is in the renormalized zone. The contribution of this region of the sample to the transmission of the probe pulse leads to its increase. In the same part of the sample where the Fermi level does not lie in the zone, the probe pulse is absorbed. Subsequently, due to recombination processes in the electron – hole pair, the plasma density and the corresponding interval between the Fermi quasilevels decrease, which leads to an increase in the absorption of the probe pulse. An additional confirmation of this is the fact that the rise time of the induced absorption is of the order of the time of a rapid decay of the bleaching in the exciton absorption region (Fig. 3, a). The disappearance of induced absorption is associated with a further decrease in the concentration of nonequilibrium carriers.

CONCLUSION

In InSe layered crystals, the absorption spectra and its time evolution at various laser intensities were studied by the method of pump-probe spectroscopy. It is shown that the bleaching in the region of exciton absorption is due to the screening of the Coulomb potential by free carriers and the exciton-exciton interaction. Experiments show that the density of pairs generated by laser light ($\sim 4.5 \times 10^{19} cm^{-3}$) in InSe is three orders of magnitude higher than the exciton density required for the Mott transition in these crystals ($n_{Mott} \sim 2,5 \times 10^{16} cm^{-3}$). An estimate shows that the screening length of the Coulomb potential by free carriers ($L \sim 10 A^o$) is much shorter than the Bohr radius of the exciton ($\sim 37 A^o$) in InSe. In the energy region between the exciton level and the edge of the conduction band, induced absorption is detected. The reason for this absorption is the renormalization of bands in InSe at high levels of optical excitation.

_____

[1] *M.J. Moran, C.Y. She. R.L. Carman.* IEEE J. Quantum Electronics 1975, 11, 259.

[2] *M. Kull, J.L. Coutaz.* J. Opt. Soc. Am. B 1990, 7, 1463.

[3] *M. Sheik-Bahae, A.A. Said, E.W. Van.* Stryland. Opt. Lett., 1989, 14, 955.

[4] *N. Peyghambarian, S.W. Koch and A. Mysyrovicz.* Introduction to semiconductor optics. New Jersey, 1993, p.325.

[5] *J. Gammassel, P. Merle, H. Mathieu.* Phys. Rev.B, 1978, v.17, 4718.

[6] *A. Cingolani.* Sol. Stat. Commun. 1985, v.35, 1007.

[7] *E. Gross.* Svobodnie elektroni v tverdix telax, Moskva, Mir, 1982, 35s.

[8] *V.Q. Lisenko, V.I. Revenko.* Fiz. Tver. Tela, 1978, v.20 (7), p. 2144.

[9] *P. Vashista and R.K. Kalia.* Phys. Rev.B, 1982, 25, p. 6412.

LIMIT RELATION BETWEEN PSEUDO JACOBI POLYNOMIALS AND HERMIT POLYNOMIALS WITH A SHIFTED ARGUMENT

Sh.M. NAGIYEV
Institute of Physics of ANAS, AZ1143, H. Javid ave., 131,
Baku, Azerbaijan

In this paper, we prove a new limit relation between the pseudo-Jacobi polynomials and Hermite polynomials with shifted argument.

1.   NEW GENERALIZED FREE HAMILTONIAN

In paper [1], we proposed a new generalized free Hamiltonian with position-dependent mass $M = M(x)$ for the describing the dynamical quantum systems. This Hamiltonian has the form

$$H_0 = \frac{1}{4N} \sum_{i=1}^{N} \left(M^\alpha \hat{p} \, M^\beta \hat{p} M^\gamma + M^\gamma \hat{p} \, M^\beta \hat{p} M^\alpha \right). \tag{1}$$

It is compatible with Galilean invariance [2] and can be represented in the form

$$H_0 = -\frac{\hbar^2}{2M} \partial_x^2 + \frac{\hbar^2 M'}{2M^2} \partial_x + A_N \frac{{M'}^2}{M^3} + B_N \frac{M''}{M^2}, \tag{2}$$

where for the coefficients A_N and B_N we have the expressions

$$A_N = \frac{\hbar^2}{2N} A, \quad A = \sum_{i=1}^{N} (\alpha_i + \gamma_i + \alpha_i \gamma_i),$$

$$B_N = -\frac{\hbar^2}{4N} B, \quad B = \sum_{i=1}^{N} (\alpha_i + \gamma_i). \tag{3}$$

Note that all Hamiltonians used in the literature to describe the quantum dynamics
of particles with mass dependent on the position [2-17]. Further, in the paper [1] on the basis of the Schrödinger equation, we constructed an exactly solvable model of a linear harmonic oscillator. The wave functions of this model are expressed in terms of pseudo Jacobi polynomials $P_n(x; v, N)$. The model mass function contains some parameter a. Purpose of this paper is to prove that in the limit $a \to \infty$ the pseudo Jacobi polynomials go over to the Hermite polynomials with a shifted argument $H_n(z - z_0)$.

2.   BASİC FORMULAS

Pseudo Jacobi polynomials are defined in terms of hypergeometric functions as follows [18,19]

$$P_n(x; v, N) = \frac{(-2i)^n (-N + iv)_n}{(n - 2N - 1)_n} \, {}_2F_1 \left(\begin{matrix} -n, & n - 2N - 1 \\ & -N + iv \end{matrix}; \frac{1 - ix}{2} \right), n = 0,1,2, \dots, N \tag{4}$$

and satisfy the orthogonality relation

$$\frac{1}{2\pi} \int_{-\infty}^{\infty} (1 + x^2)^{-N-1} e^{2v \arctan x} P_m(x; v, N) \, P_n(x; v, N) =$$

$$= \frac{\Gamma(2N+1-2n)\Gamma(2N+2-2n) 2^{2n-2N-1} n!}{\Gamma(2N+2-n)|\Gamma(N+1-n+iv)|^2} \delta_{nm}. \tag{5}$$

We also write down for them a differential equation

$$(1 + x^2) y'' \big(x_1 + 2(v - Nx) y'(x) - n(n - 2N - 1)\big) y(x) = 0, \quad y(x) = P_n(x; v, N) \tag{6}$$

Similar formulas for the Hermite polynomials are

$$H_n(x) = (2x)^n {}_2F_0\left(-\frac{n}{2}, \quad -\frac{(n-1)}{2}; -\frac{1}{x^2}\right),$$ (7)

$$\int_{-\infty}^{\infty} e^{-x^2} H_m(x) H_n(x)\, dx = 2^n (n!)\sqrt{\pi}\,\delta_{mn},$$ (8)

$$y''(x) - 2xy'(x) + 2ny(x) = 0, \quad y(x) = H_n(x).$$ (9)

3. THEOREM

The following limit relation holds between the pseudo Jacobi and Hermite polynomials

$$\lim_{N\to\infty} 2^n N^{\frac{n}{2}} P_n\left(\frac{x}{\sqrt{N}}; v\sqrt{N}, N\right) = H_n(x - v).$$ (10)

We will prove this theorem in two ways.

Proof 1. To prove (2), we will use the recurrence relations for the pseudo Jacobi and Hermite polynomials [18,19], which have the form

$$P_{n+1}(x; v, N) = A_n P_n(x; v, N) + B_n P_{n-1}(x; v, N),$$ (11)

$$H_{n+1}(z) = 2z H_n(z) - 2n H_{n-1}(z),$$ (12)

where

$$A_n(x, v) = x - \frac{v(N+1)}{(n-N-1)(n-N)}, \quad B_n(v) = -\frac{n(n-2N-2)(n-N-1-iv)(n-N+1+iv)}{(2n-2N-3)(n-N-1)^2(2n-2N-1)}.$$ (13)

Let be

$$Q_n = 2^n N^{n/2} P_n\left(\frac{x}{\sqrt{N}}; v\sqrt{N}, N\right) \text{ and } \quad \bar{Q}_n = \lim_{N\to\infty} Q_n.$$ (14)

Then from (11) we obtain the following recurrence relation for the polynomials Q_n

$$Q_{n+1} = \bar{A}_n Q_n + \bar{B}_n Q_{n-1},$$ (15)

where

$$\bar{A}_n = 2\sqrt{N} A_n\left(\frac{x}{\sqrt{N}}; v\sqrt{N}\right), \bar{B}_n = 4N B_n(v\sqrt{N}).$$ (16)

Since $\lim_{N\to\infty} \bar{A}_n = 2(x-v)$ and $\lim_{N\to\infty} \bar{B}_n = -2n$, then passing to the limit $N \to \infty$ in (15) we come to

$$\bar{Q}_{n+1} = 2(x-v)\bar{Q}_n - 2n\bar{Q}_{n-1}.$$ (17)

And this coincides with the recurrence relation for the Hermite polynomials (12) for $z = x - v$. Hence, $\bar{Q}_n = H_n(x - v)$. This completes the proof of (10).

Proof 2. Let us now prove the relation (10) by the method of mathematical induction. To do this, we first write explicitly the pseudo Jacobi and Hermite polynomials for the first few values of n:

$$P_0(x; v, N) = 1, \quad P_1(x; v, N) = x - \frac{v}{N},$$

$$P_2(x; v, N) = \left[x - \frac{v(N+1)}{N(N-1)}\right]\left(x - \frac{v}{N}\right) - \frac{N^2 + v^2}{N^2(2N-1)},$$

$$H_0(z) = 1 \quad H_1(z) = 2z \quad H_2(z) = 4z^2 - 2.$$ (18)

Using the explicit form of polynomials (18), we can directly verify that for $n = 1$ and 2, relation (10) is true, i.e.

$$\lim_{N\to\infty} 2\sqrt{N}\, P_1\left(\frac{x}{\sqrt{N}}; \nu\sqrt{N}, N\right) = H_1(x-\nu),$$

$$\lim_{N\to\infty} 2^2 N\, P_2\left(\frac{x}{\sqrt{N}}; \nu\sqrt{N}, N\right) = H_2(x-\nu). \tag{19}$$

Assuming now that our relation (10) is true for n, we see that then it is true for $n+1$ as well. Indeed, we have

$$\lim_{N\to\infty} 2^{n+1} N^{\frac{n+1}{2}} P_{n+1}\left(\frac{x}{\sqrt{N}}; \nu\sqrt{N}, N\right) =$$

$$= \lim_{N\to\infty} 2\sqrt{N} A_n\left(\frac{x}{\sqrt{N}}, \nu\sqrt{N}\right) \lim_{N\to\infty} 2^n N^{\frac{n}{2}} P_n\left(\frac{x}{\sqrt{N}}; \nu\sqrt{N}, N\right) +$$

$$+ \lim_{N\to\infty} 4N B_n(\nu\sqrt{N}) \lim_{N\to\infty} 2^{n-1} N^{\frac{n-1}{2}} P_{n-1}\left(\frac{x}{\sqrt{N}}; \nu\sqrt{N}, N\right) = 2z H_n(z) - 2n H_{n-1}(z).$$

Therefore, according to (18), we can write

$$\lim_{N\to\infty} 2^{n+1} N^{\frac{n+1}{2}} P_{n+1}\left(\frac{x}{\sqrt{N}}; \nu\sqrt{N}, N\right) = H_{n+1}(z), z = x-\nu.$$

Hence, the limit relation (10) is also true for all values of *n*. This completes the second proof of the theorem.

———————————————————————

[1] *Sh. M. Nagiyev, K. Sh. Jafarova.* Generalized Hamiltonian with position-dependent mass and pseudo-Jacobi oscillator, AJP Fizika, 2021, vol. XXVII: 1,.

[2] *J.-M. Levy-Leblond.* "Position-dependent effective mass and Galilean invariance", Phys. Rev. A, 1995, 52, 1845–1849.

[3] *O. von Roos.* "Position-dependent effective masses in semiconductor theory", Phys. Rev. B, 1983, 27, 7547–7551.

[4] *A.R. Plastino, A. Rigo, M. Casas, F. Garcias and A. Plastino.* "Supersymmetric approach to quantum systems with position-dependent effective mass", Phys. Rev. A, 60, 1999, 4318–4325.

[5] *C. Quesne and V.M. Tkachuk.* "Deformed algebras, position-dependent effective masses and curved spaces: an exactly solvable Coulomb problem", J. Phys. A: Math. Gen., 37, 2004, 4267–4281.

[6] *J. Yu, S.-H. Dong,* Exactly solvable potentials for the Schrödinger equation with spatially dependent mass, Phys. Lett. A 325, 2004, 194–198.

[7] *M.L. Cassou, S.-H. Dong, J. Yu.* Quantum features of semiconductor quantum dots, Physics Letters A 331, 2004, 45–52.

[8] *B. Roy.* Lie algebraic approach to singular oscillator with a position-dependent mass Europhys. Lett., 2005, 72 (1), pp. 1–6.

[9] *A.G.M. Schmidt.* Wave-packet revival for the Schrödinger equation with position-dependent mass, Phys. Lett. A 353, 2006, 459–462.

[10] *A de Souza Dutra, A de Oliveira.* Two-dimensional position-dependent massive particles in the presence of magnetic fields, J. Phys. A: Math. Theor. 42, 2009, 025304 (13pp).

[11] *G. Levai, O. Ozer.* An exactly solvable Schrödinger equation with finite positive position-dependent effective mass, J. Math. Phys. 51, 2010, 092103.

[12] *A. Arda, R. Sever,* Bound State Solutions of Schr¨odinger Equation for Generalized Morse Potential with Position-Dependent Mass, Commun. Theor. Phys. 56, 2011, 51–54.

[13] *H. Rajbongshi.* "Exactly solvable potentials and the bound-state solution of the position-dependent mass Schrodinger equation in *D*-dimensional space", Theor. Math. Phys., 2015, 184, 996–1010.

[14] *N. Amir, S. Iqbal.* Algebraic solutions of shape-invariant position-dependenteffective mass systems, J.Math.Phys. 2017, 57, 465202.

[15] *E.I. Jafarov, S.M. Nagiyev, R. Oste and J. Van der Jeugt.* Exact solution of the position-dependent effective mass and angular frequency Schrödinger equation: harmonic oscillator model with quantized confinement parameter, Journal of Physics A: Math.Theor.

[16] *E.I. Jafarov, S.M. Nagiyev, A.M. Jafarova.* Quantum-mechanical explicit solution for the confined harmonic oscillator model with the Von Roos kinetic energy operator, Reports on Mathematical Physics, Vol. 86: 1, 2020, 25-37.

[17] *E.I. Jafarov, S.M. Nagiyev, A.M. Seyidova.* Zhu-Kroemer kinetic energy operator with position-

dependent effective mass and exact solution of the non-relativistic confined harmonic oscillator model. AMEA-nın Xəbərləri, Fiz.-texn., riyaz. Ser., fizika və astronomiya №2, 2020, 3-14.

[18] *H. Bateman and A. Erd´elyi.* Higher Transcendental Functions: Vol. 2, McGraw Hill Publications, New York, 1953.

[19] *R. Koekoek, P.A. Lesky and R.F. Swarttouw.* Hypergeometric Orthogonal Polynomials and their q-Analogues, Springer, Berlin 2010.

GENERALIZED HAMILTONIAN WITH POSITION-DEPENDENT MASS AND PSEUDO-JACOBI OSCILLATOR

Sh.M. NAGIYEV, K.Sh. JAFAROVA

Institute of Physics, Azerbaijan National Academy of Sciences, H. Javid av. 131, AZ-1143, Baku, Azerbaijan

Exactly-solvable model of the quantum harmonic oscillator is proposed. In this work we propose a new generalized Hamiltonian, to describe variable mass systems. Wave functions of the stationary states and energy spectrum of the model are obtained through the solution of the corresponding Schrödinger equation with the positive position-dependent effective mass. We have shown that the wave functions of the stationary states of the model under consideration are expressed through the pseudo Jacobi polynomials $P_n(\xi; \nu, \overline{N})$. The parameter a of the model is quantized in terms of $\overline{N}$. As a consequence of it, the number of the its energy spectrum is finite. Under the limit $a \to \infty$ the system recovers the known non-relativistic quantum harmonic oscillator in the quantum mechanics. We also obtained the limiting relation between the pseudo Jacobi and Hermite polynomials.

1. INTRODUCTION

The number of exactly solvable problems in quantum mechanics is limited, but they play an important role in the study of the properties of various dynamical systems. This is, firstly, due to the fact that the exact solutions play the role of the foundation on which the solution of many other problems is built, secondly, they allow, from the point of view of symmetry, to understand their essence, and thirdly, they themselves can have directly various applications in many areas of theoretical physics. It should also be noted that exactly solvable problems are also interesting from the point of view of mathematics, since in many cases they can lead to the establishment of new properties of various special functions. For example, the problem of a harmonic oscillator, being exactly solvable, is widely used in atomic and nuclear physics, in the theory of crystals, in quantum field theory, etc. [1-4]. For this reason, the construction of exactly solvable quantum mechanical models, including models of a harmonic oscillator, for describing various physical systems has always attracted and continues to attract the attention of physicists [5-11].

On the other hand, various quantum mechanical systems described by the Schrödinger equation in cases where the Hamiltonian of the system contains the position-dependent mass [12-29]. These systems have found applications in a wide range of fields of the material science and condensed matter physics. A number of papers [14, 17, 19, 20, 22-29] are devoted to the construction of exactly solvable potentials for the Schrödinger equation with the position-dependent mass mass, and in [15] was obtained exact solution of the Dirac equation for a charged particle with position-dependent mass in the Coulomb field.

Our goal is to construct a quantum-mechanical exactly solvable model of a linear harmonic oscillator with the the position-dependent mass in an external uniform gravitational field. Our construction is based on the Schrödinger equation with a free Hamiltonian, generalizing the free Hamiltonian von Roos with the position-dependent mass. We show that the wave functions of our model are expressed in terms of pseudo-Jacobi polynomials. For this reason, we will call it the pseudo-Jacobi oscillator.

This article is organized as follows. Section 2 contains brief review of the nonrelativistic quantum-mechanical linear harmonic oscillator model.

2. NONRELATIVISTIC LINEAR HARMONIC OSCILLATOR WITH CONSTANT MASS

Let us write the one-dimensional Schrödinger equation describing the motion of a nonrelativistic quantum particle with constant mass m_0 in the external field $V(x)$.

It has the form

$$\left[\frac{\hat{p}^2}{2m_e} + V(x)\right]\psi(x) = E\psi(x), \qquad (2.1)$$

where $\hat{p} = -i\partial_x$ is the momentum operator. A linear harmonic oscillator with frequency ω corresponds to the following potential energy

$$V(x) = \frac{m_0\omega^2 x^2}{2}. \qquad (2.2)$$

Let us rewrite equation (2.1) with potential (2.2) as

$$\frac{d^2\psi}{dx^2} + \frac{2m_0}{\hbar^2}\left(E - \frac{m_0\omega^2 x^2}{2}\right)\psi = 0. \qquad (2.3)$$

The solution and energy spectrum of this equation are well known [1]

$$\psi_n^{0S}(x) = C_n^{0S} e^{-\frac{1}{2}\lambda_0^2 x^2} H_n(\lambda_0 x),$$

$$E_n^{0S} = \hbar\omega\left(n + \frac{1}{2}\right), \quad n = 0,1,2,\dots, \quad (2.4)$$

where $H_n(x)$ are Hermite polynomials, and $\lambda_0 = \sqrt{m_0\omega/\hbar}$. Normalizing constants

$$C_n^{0S} = \frac{C_0^{0s}}{\sqrt{2^n n!}},$$

$$C_0^{0S} = \left(\frac{\lambda_0^2}{\pi}\right)^{1/4} = \left(\frac{m_0\omega}{\pi\hbar}\right)^{1/4} \qquad (2.5)$$

found from the orthogonality condition for the Hermite polynomials [30, 31]

$$\int_{-\infty}^{\infty} e^{-x^2} H_m(x)H_n(x)dx = \sqrt{\pi}2^n n! \, \delta_{nm}. \qquad (2.6)$$

3. GENERALIZED FREE HAMILTONIAN WITH THE POSITION-DEPENDENT MASS

In this paper, we will construct a new model of a nonrelativistic linear harmonic oscillator, namely with the position-dependent mass pseudo-Jacobi oscillator. It should be noted that the construction of models of quantum physical systems with the position-dependent mass $M \equiv M(x)$ starts with choosing the form of the free Hamiltonian to describe the position-dependent mass systems and with the subsequent selection of the mass function $M(x)$. The point is that due to the non-commutativity of the momentum operators $\hat{p} = -i\hbar\partial_x$ and the function $M(x)$, the question arises of their ordering in the expression for the free Hamiltonian

$$H_0 = \frac{1}{2M(x)}\hat{p}^2. \qquad (3.1)$$

In this regard, we note that this issue was analyzed in [13], where it is proposed to restrict ourselves to a specific class of the form of the Hamiltonian with the position-dependent mass. According to this paper the free Hamiltonian operator must depend only on the mass function $M(x)$. Accordingly, it will take the following general form

$$H_0 = \frac{1}{2}\hat{p}\frac{1}{M(x)}\hat{p} + W_{kin}(x), \qquad (3.2)$$

with the condition that the term W_{kin} be a functional of M, possibly involving its derivatives. Further the dimensional arguments require this term to be homogeneous of degree (-1) in M and of degree (-2) in x. Analyticity conditions precluding nonintegral powers of the derivatives of M and, finally, the condition that for a constant function $M(x) = m$ one recovers the usual expression, implying that the derivatives of M must appear with positive (integral) powers, lead to two possible terms only in W_{kin}:

$$W_{kin} = A_1\frac{M'^2}{M^3} + B_1\frac{M''}{M^2}. \qquad (3.3)$$

In this paper is also stated that under the above conditions the most general free Hamiltonian is precisely the von Roos Hamiltonian of the form [12]

$$H_0 = \frac{1}{4}\left(M^\alpha\hat{p}\,M^\beta\hat{p}M^\gamma + M^\gamma\hat{p}\,M^\beta\hat{p}M^\alpha\right), \qquad (3.4)$$

where the real parameters α, β and γ satisfy the natural condition $\alpha + \beta + \gamma = -1$, but otherwise they are arbitrary. The von Roos free Hamiltonian (3.4) has the form (3.2) with (3.3), where the coefficients A_1 and B_1 are

$$A_1 = \frac{1}{2}(\alpha + \gamma + \alpha\gamma), B_1 = -\frac{1}{4}(\alpha + \gamma). \quad (3.5)$$

In this section, we propose a new (generalized) free Hamiltonian to solve the problems with mass depending on the position as

$$H_0 = \frac{1}{4N}\sum_{i=1}^{N}\left(M^{\alpha_i}\hat{p}M^{\beta_i}\hat{p}M^{\gamma_i} + M^{\gamma_i}\hat{p}M^{\beta_i}\hat{p}M^{\alpha_i}\right), \qquad (3.6)$$

where $N = 1,2,3\ldots$ is an arbitrary positive integer and the parameters $\alpha_i, \beta_i, \gamma_i$ $(i = 1,2,\ldots,N)$ satisfy the conditions(3.7)
$\alpha_i + \beta_i + \gamma_i = -1, i = 1,2,\ldots,N$.
The Hamiltonian (3.6) is more general than the Hamiltonian (3.4) von Roos [12] and the Hamiltonian

$$H_0 = \frac{1}{6}\left(\frac{1}{M}\hat{p}^2 + \hat{p}\frac{1}{M}\hat{p} + \hat{p}^2\frac{1}{M}\right), \qquad (3.8)$$

proposed in [24]. Consequently, the free Hamiltonians used in the literature [12-29] for dynamical systems with the position-dependent mass are special cases (3.6). For example, for $N = 3$, $\alpha_1 = -1$, $\beta_1 = \gamma_1 = 0$, $\alpha_2 = \gamma_2 = 0$, $\beta_2 = -1$ and $\alpha_3 = -1$, $\beta_3 = \gamma_3 = 0$ from (3.6) follows (3.8). If we represent (3.6) in the form (3.2) and (3.3), i.e.

$$H_0 = -\frac{\hbar^2}{2M}\partial_x^2 + \frac{\hbar^2 M'}{2M^2}\partial_x + A_N\frac{M'^2}{M^3} + B_N\frac{M''}{M^2}, \qquad (3.9)$$

then for the coefficients A_N and B_N we get the following expressions

$$A_N = \frac{\hbar^2}{2N}A, \ A = \sum_{i=1}^{N}(\alpha_i + \gamma_i + \alpha_i\gamma_i),$$

$$B_N = -\frac{\hbar^2}{4N}B, \quad B = \sum_{i=1}^{N}(\alpha_i + \gamma_i). \qquad (3.10)$$

From the requirement that the Hamiltonian H_0 (3.6) (or (3.9)) be Hermitian, it follows that the coefficients A_N and B_N (3.10) must be real. Therefore, in the general case, the parameters $\alpha_i, \beta_i, \gamma_i$ $(i = 1,2, ..., N)$ can be complex, provided that the relations $\gamma_i = \alpha_i^*$ $(i = 1,2, ..., N)$ are satisfied, i.e. α_i and γ_i must be mutually complex conjugate.

Taking into account now (3.9), the Schrödinger equation for quantum systems with the position-dependent mass in the potential field $V(x)$ is written in the form

$$\left\{\partial_x^2 - \frac{M'}{M}\partial_x - \frac{A}{N}\frac{M'^2}{M^2} + \frac{B}{2N}\frac{M''}{M} + \frac{2M}{\hbar^2}[E - -V(x)]\right\}\psi(x) = 0. \qquad (3.11)$$

4. PSEUDO-JACOBI OSCILLATOR WITH THE POSITION-DEPENDENT MASS

For building pseudo-Jacobi oscillator with the position-dependent mass we define position-dependent mass function $M(x)$ as follows

$$M(x) = \frac{a^2 m_0}{a^2 + x^2}, \qquad (4.1)$$

where $a > 0$ is some parameter with the dimension of length. Obviously, in the limit $a \to \infty$, the dependence of the mass (4.1) on the coordinate x disappears, i.e.

$$\lim_{a \to \infty} M(x) = m_0. \qquad (4.2)$$

Let's write the potential energy of our model in the usual form

$$V(x) = \frac{M(x)\,\omega^2\,x^2}{2}. \qquad (4.3)$$

It is also clear that the following limit relations will take place both for the generalized free Hamiltonian (3.6) (or (3.9)) and for the potential energy of the model (4.3)

$$\lim_{a \to \infty} H_0 = -\frac{\hbar^2}{2m_0}\partial_x^2, \lim_{a \to \infty} V(x) = \frac{m_0\,\omega^2\,x^2}{2}.(4.4)$$

i.e., in the limit when the model parameter a tends to infinity ($a \to \infty$), these quantities coincide with the corresponding quantities of nonrelativistic quantum mechanics

Substituting the expression for mass (4.1) into (3.11), we obtain the Schrödinger equation describing the motion of our oscillator model

$$\left\{\partial_x^2 + \frac{2x}{a^2+x^2}\partial_x - \frac{A}{N}\frac{4x^2}{(a^2+x^2)^2} + \frac{B}{N}\frac{3x^2-a^2}{(a^2+x^2)^2} + \frac{2a^2 m_0}{\hbar^2(a^2+x^2)}\left[E - \frac{a^2 m_0 \omega^2 x^2}{2(a^2+x^2)}\right]\right\}\psi = 0. \qquad (4.5)$$

In terms of the new dimensionless variable $\xi = \frac{x}{a}$, the equation (4.5) takes the form

$$\left(\partial_\xi^2 + \frac{\tilde{\tau}}{\sigma}\partial_\xi + \frac{\tilde{\sigma}}{\sigma^2}\right)\psi = 0, \qquad (4.6)$$

where we have introduced the following notations $\tilde{\tau} = 2\xi$, $\sigma = 1 + \xi^2$, $\tilde{\sigma} = c_0 - c_2\xi^2$. For the coefficients c_0 and c_2 we have

$$c_0 = \frac{2a^2 m_0 E}{\hbar^2} - \frac{B}{N},$$

$$c_2 = \frac{a^4 m_0^2 \omega^2}{\hbar^2} - \frac{2m_0 a^2 E}{\hbar^2} - \frac{A_2}{N},$$

$$A_2 = \sum_{i=1}^{N}(\alpha_i + \gamma_i - 2\alpha_i\gamma_i). \qquad (4.7)$$

Let us look for solution ψ of equation (4.6) as follows [32]:

$$\psi = \varphi(\xi)y(\xi), \quad \varphi(\xi) = e^{\int \frac{\pi(\xi)}{\sigma(\xi)}d\xi}. \qquad (4.8)$$

Here, $\pi(\xi)$ is an arbitrary polynomial of at most first degree and $\sigma \equiv \sigma(\xi)$. Then, by performing simple straightforward computations, one obtains the following second-order differential equation for $y \equiv y(\xi)$:

$$y'' + \frac{\bar{\tau}}{\sigma}y' + \frac{\bar{\sigma}}{\sigma^2}y = 0, \qquad (4.9)$$

with

$$\bar{\tau} = \tilde{\tau} + 2\pi, \quad \bar{\sigma} = \tilde{\sigma} + \pi^2 + \sigma\pi'.$$

It is seen that $\bar{\tau}(\xi)$ and $\bar{\sigma}(\xi)$ are polynomials, respectively, not higher than the first and second degrees. We now choose a polynomial $\pi(\xi)$ from the condition that the polynomial $\bar{\sigma}(\xi)$ be divided without remainder by $\sigma(\xi)$, i.e.

$$\bar{\sigma} = \lambda\sigma, \lambda = \text{const.} \qquad (4.10)$$

Now, equation (4.9) takes the form

$$\sigma y'' + \bar{\tau}y' + \lambda y = 0. \qquad (4.11)$$

Condition (4.10) gives a quadratic equation for the definition of a polynomial $\pi(\xi)$ and a constant λ:

$$\pi^2 - (\sigma' - \tilde{\tau})\pi - \mu\sigma + \tilde{\sigma} = 0,$$
$$\mu = \lambda - \pi'. \qquad (4.12)$$

From here, we find

$$\pi = \frac{\sigma' - \tilde{\tau}}{2} + e\sqrt{\left(\frac{\sigma' - \tilde{\tau}}{2}\right)^2 + \mu\sigma - \tilde{\sigma}} \ , \ \ e = \pm 1.$$
(4.13)

In our case $\sigma' - \tilde{\tau} = 0$ and we have $\pi = e\sqrt{\mu\sigma - \tilde{\sigma}}$ or $\pi = e\sqrt{\mu - c_0 + (\mu + c_2)\xi^2}$. Since $\pi(\xi)$ is a polynomial, the discriminant of a polynomial of the second degree standing under the root (4.13) D must be equal to zero. The equation D = 0 allows us to find a constant μ. After determination μ, we find $\pi(\xi)$ by equation (4.12), then $\varphi(\xi)$, $\bar{\tau}(\xi)$ and λ with the help of (4.8), (4.9) and (4.12). In our case there are two possibility:

1) $\mu = c_0$, $\pi = e\,q_1\xi$, $q_1 = \sqrt{(c_0 + c_2)}$,
2) $\mu = -c_2$, $\pi = eq_2$, $q_2 = \sqrt{-(c_0 + c_2)}$,
(4.14)

Where $\quad c_0 + c_2 = \frac{a^4 m_0{}^2\omega^2}{\hbar^2} - \frac{Q}{N}$,
$Q = B + A_2 = 2\sum_{i=1}^{N}(\alpha_i + \gamma_i - \alpha_i\gamma_i)$.

We will restrict ourselves to the case when $c_0 + c_2 > 0$. In this case, the physical meaning has the first

expression for the polynomial $\pi(\xi)$. Moreover, for $\varphi(\xi)$ we obtain the following expression: $\varphi(\xi) = (1 + \xi^2)^{\frac{eq_1}{2}}$. From the requirement of finiteness $\varphi(\xi)$ at points $\xi = \pm\infty$, i.e. from the condition $\lim_{\xi\to\pm\infty} \varphi(\xi) = 0$ (square integrability condition), we get $eq_1 < 0$. This means that $e = -1$ and, $\pi = -q_1\xi$. Thus, we get:

$$\varphi(\xi) = (1 + \xi^2)^{-\frac{q_1}{2}}$$

$$q_1 = \sqrt{\frac{a^4 m_0{}^2\omega^2}{\hbar^2} - \frac{a}{N}} = \sqrt{\lambda_0^4 a^4 - \frac{a}{N}}. \quad (4.15)$$

Now, taking into account that $\bar{\tau} = 2(1 - q_1)\xi$ and $\lambda = \mu + \pi' = c_0 - q_1$, one can rewrite the equation (4.11) in the form

$$(1 + \xi^2)y'' + 2(1 - q_1)\xi y' + (c_0 - q_1)y = 0.$$
(4.16)

Comparison (4.16) with the second order differential equation for the pseudo Jacobi polynomials $\bar{y} \equiv P_n(\xi; \nu, \bar{N})$:

$$(1 + \xi^2)\bar{y}'' + 2(\nu - \bar{N}\xi)\bar{y}' + n(2\bar{N} - n + 1)\bar{y} = 0, n = 0,1,2,3\dots,\bar{N} \qquad (4.17)$$

gives us the relations

$$\nu = 0, \ q_1 = \bar{N} + 1,$$
$$c_0 - q_1 = n(2\bar{N} + 1 - n), \bar{N} = 0,1,2,3,\dots \qquad (4.18)$$

These relations lead to quantization of arbitrary parameter a being of position dimensions and introduced in the framework of definition of the position-dependent mass $M(x)$ (4.1):

$$a \equiv a_N = \left[(\bar{N} + 1)^2 + \frac{Q}{N}\right]^{1/4}. \qquad (4.19)$$

Therefore, position-dependent effective mass $M(x)$ is quantizing as follows:

$$M(x) \equiv M_N(x) = \frac{\sqrt{(\bar{N}+1)^2 + \frac{Q}{N}}}{\sqrt{(\bar{N}+1)^2 + \frac{Q}{N} + \lambda_0^2 x^2}}\, m_0. \qquad (4.20)$$

Taking this hidden feature of position-dependent effective mass $M(x)$, one obtains the following exact expressions for the energy spectrum

$$E \equiv E_n = \frac{\hbar^2}{2m_0 a^2}\left[n(2\bar{N} + 1 - n) + \bar{N} + 1 + Q/N\right] \qquad (4.21a)$$

or

$$E_n = \frac{1}{2}\hbar\omega\,\frac{n(2\bar{N}+1-n)+\bar{N}+1+Q/N}{\sqrt{(\bar{N}+1)^2 + Q/N}}, \quad n = 0,1,2,3\dots,N. \qquad (4.21b)$$

Thus, exact polynomial of equation (4.16) are expressed by the pseudo Jacobi polynomials, i. e.

$$y(\xi) \equiv y_n(\xi) \equiv P_n(\xi; \nu, \bar{N}). \qquad (4.22)$$

36

Now, taking into account (4.8), (4.15) and (4.22) one obtains the following expression for the wave functions of our model

$$\psi(\xi) \equiv \psi_{Nn}(\xi) = C_{Nn}(1 + \xi^2)^{-\frac{q_1}{2}} P_n(\xi; 0, \bar{N}). \tag{4.23}$$

Let's express them through the variable x:

$$\psi_{Nn}(x) = C_{Nn} \left(1 + \frac{\lambda_0^2 x^2}{\sqrt{(\bar{N}+1)^2 + Q/N}} \right)^{-\frac{\bar{N}+1}{2}} P_n \left(\frac{\lambda_0 x}{\sqrt[4]{(\bar{N}+1)^2 + Q/N}}; 0, \bar{N} \right) \tag{4.24}$$

Normalizing constants ($n = 0,1,2,3 \dots, N$)

$$C_{Nn} = 2^{\bar{N}-n} \sqrt{\frac{\lambda_0}{\pi n!}} \left[(\bar{N} + 1)^2 + Q/N \right]^{-\frac{1}{8}} \frac{\Gamma(\bar{N}+1-n)}{\Gamma(2\bar{N}+1-2n)} \sqrt{\frac{\Gamma(2\bar{N}+2-n)}{2\bar{N}+1-2n}} \tag{4.25}$$

we find from the condition that the wave functions (4.24) are orthonormal

$$\int_{-\infty}^{\infty} \psi_{Nn}^*(x)\psi_{Nm}(x)dx = \delta_{nm}. \tag{4.26}$$

In calculating the integral in (4.26), we used the orthogonality condition for the pseudo Jacobi polynomials [31]

$$\int_{-\infty}^{\infty} (1 + x)^{-N-1} e^{2\nu \operatorname{arctg} x} P_n(x; \nu, N) P_m(x; \nu, N) dx = d_n^2 \delta_{nm}, \tag{4.27}$$

where d_n^2- is the square of the norm of the pseudo Jacobi polynomials and is equal to

$$d_n^2 = \pi n! \, 2^{2n-2N} \frac{\Gamma(2N+1-2n)\Gamma(2N+2-2n)}{\Gamma(2N+2-n)|\Gamma(N+1-n+i\nu)|^2}. \tag{4.28}$$

In conclusion of this section, we also present the form of the wave functions, explicitly indicating the dependences on the parameter a (4.19) of the model

$$\psi_{Nn}(x) = C_{Nn} \left(1 + \frac{x^2}{a^2} \right)^{-\frac{1}{2}\sqrt{\lambda_0^4 a^4 - Q/N}} P_n \left(\frac{x}{a}; 0, \sqrt{\lambda_0^4 a^4 - Q/N} - 1 \right). \tag{4.29}$$

5. CONCLUSION

In this paper, we have constructed an exactly solvable linear harmonic oscillator model with the position-dependent mass. The main point of this article is the proposal of a new and the most general Hamiltonian for the quantum dynamical systems with the position-dependent mass. This Hamiltonian contains, in the form of special cases, the Hamiltonians used in the literature. One feature of the psevdo Jacobi oscillator is that the number of its energy levels is finite. This is due to the fact that the depth of the pseudo-parabolic oscillatory well $V_0 > 0$ is finite. This depth is

$$\lim_{x \to \pm\infty} V(x) = \lim_{x \to \pm\infty} \frac{M(x)\omega^2 x^2}{2} = \frac{1}{2}\hbar\omega\sqrt{(\bar{N} + 1)^2 + Q/N} \equiv V_0. \tag{5.1}$$

The second feature is relating to the fact that the energy levels are not equidistant. The minimum and maximum energy values are respectively

$$E_{N0} = \frac{\hbar\omega}{2} \frac{(\bar{N}+1)^2 + Q/N}{\sqrt{(\bar{N}+1)^2 + Q/N}} \quad \text{and} \quad E_{N\bar{N}} = \frac{\hbar\omega}{2} \frac{\bar{N}(\bar{N}+2) + 1 + Q/N}{\sqrt{(\bar{N}+1)^2 + Q/N}}. \tag{5.2}$$

The wave functions of the constructed model of the oscillator are expressed in terms of pseudo Jacobi polynomials. In the limit $a \to \infty$, all quantities (equation of motion, wave functions, energy spectrum) of this model transform into the corresponding quantities of an ordinary linear harmonic oscillator with constant mass. For example, for energy levels (4.21) and wave functions (4.24) we have the following limit expressions

$$\lim_{a \to \infty} E_n = \hbar \omega (n + 1/2), \qquad (5.3)$$

$$\lim_{a \to \infty} \psi_{Nn}(x) = \sqrt{\frac{\lambda_0}{2^n n! \sqrt{\pi}}} H_n(\lambda_0 x) e^{-\frac{1}{2}\lambda_0^2 x^2}. \quad (5.4)$$

It is clear from formula (5.4) that there is a limit relation between the pseudo Jacobi and Hermite polynomials with a shifted argument. We will prove in the next paper that it has the form

$$\lim_{N \to \infty} N^{\frac{n}{2}} P_n \left(\frac{x}{\sqrt{N}}; \nu \sqrt{N}, N \right) = \frac{1}{2^n} H_n(x - \nu). \quad (5.5)$$

Let us make one more remark about the properties of the pseudo Jacobi oscillator, connected with the form of the generalized free Hamiltonian (3.6) (or (3.9)). In obtaining solutions (4.21) and (4.24), we assumed that the following inequality holds:

$$\frac{a^4 m_0^2 \omega^2}{\hbar^2} - \frac{Q}{N} > 0, \qquad (5.6)$$

where $Q = 2 \sum_{i=1}^{N} (\alpha_i + \gamma_i - \alpha_i \gamma_i)$. However, for certain values of the parameters α_i, γ_i $(i = 0,1,2,3 \dots, N$ this inequality may not hold, i.e., the pseudo Jacobi oscillator for certain energy values may not have a discrete spectrum ...

[1] *L.D. Landau and E.M. Lifshitz.* Quantum mechanics (Non-relativistic Theory) (Oxford: Pergamon, 1991).

[2] *M. Moshinsky and Y.F. Smirnov.* The harmonic oscillator in modern physics (New York: Harwood Academic, 1996).

[3] *S.C. Bloch.* Introduction to classical and quantum harmonic oscillators (Wiley, New-York, 1997).

[4] *R.P. Feynman, M. Kislinger, and F. Ravndal.* Current Matrix Elements from a Relativistic Quark Model, Phys. Rev. 3**:** 11, 1971, 2706-2732.

[5] *N.M. Atakishiyev, R.M. Mir-Kasimov, Sh.M. Nagiyev.* Quazi-potential models of relativistic oscillators, TMPh, 1980, vol. 44, № 1, pp. 47–62.

[6] *N.M. Atakishiyev, R.M. Mir-Kasimov, and Sh.M. Nagiyev.* A Relativistic Model of the Isotropic Oscillator, Ann. Phys., 42, No. 1, 1985, 25–30.

[7] *S.M. Nagiyev, E.I. Jafarov, and R.M. Imanov.* The relativistic linear singular oscillator, J. Phys. A: Math. and Gen., 36, 2003, 7813-7824.

[8] *S.M. Nagiyev, E.I. Jafarov, R.M. Imanov, and L. Homorodean.* A relativistic model of the isotropic three-dimensional singular oscillator, Phys. Lett. A 334 (4), 2005, 260-266.

[9] *V.V. Borzov.* Orthogonal polynomials and generalized oscillator algebras, Integral Transform.Spec. Funct. 12 :2. 2001, 115-138.

[10] *V.V. Borzov.* Generalized oscillator and its coherent states, TMPh, 2007, vol. 153, № 3, pp. 363–380.

[11] *Yu.A. Grishechkin and V.N. Kapshai.* Solution of the Logunov-Tavkhelidze equation for the 3-dimensional oscillator potential in the relativistic configuration representation, Russian Phys. Jour., Vol. 61, No. 9, 2019, pp. 1645-1652.

[12] *O. von Roos.* "Position-dependent effective masses in semiconductor theory", Phys. Rev. B, 27, 1983, 7547–7551.

[13] *J.-M. Levy-Leblond.* "Position-dependent effective mass and Galilean invariance", Phys. Rev. A, 52, 1995, 1845–1849.

[14] *A.R. Plastino, A. Rigo, M. Casas, F. Garcias and A. Plastino.* "Supersymmetric approach to quantum systems with position-dependent effective mass", Phys. Rev. A, 60, 1999, 4318–4325.

[15] *A.D. Alhaidari.* "Solution of the Dirac equation with position-dependent mass in the Coulomb field", Phys.Lett. A, 322, 72–77 (2004).

[16] *C. Quesne and V.M. Tkachuk.* "Deformed algebras, position-dependent effective masses and curved spaces: an exactly solvable Coulomb problem", J. Phys. A: Math. Gen., 37, 2004, 4267–4281.

[17] *J. Yu, S.-H. Dong.* Exactly solvable potentials for the Schrödinger equation with spatially dependent mass, Phys. Lett. A 325, 2004, 194–198.

[18] *M.L. Cassou, S.-H. Dong, J. Yu.* Quantum features of semiconductor quantum dots, Physics Letters A 331, 2004, 45–52.

[19] *B. Roy.* Lie algebraic approach to singular oscillator with a position-dependent mass Europhys. Lett., 72 (1), 2005, pp. 1–6.

[20] *A.G.M. Schmidt.* Wave-packet revival for the Schrödinger equation with position-dependent mass, Phys. Lett. A 353 (2006) 459–462.

[21] *A de Souza Dutra, A de Oliveira.* Two-dimensional position-dependent massive particles in the presence of magnetic fields, J. Phys. A: Math. Theor. 42, 2009, 025304 (13pp).

[22] *G. Levai, O. Ozer.* An exactly solvable Schrödinger equation with finite positive position-dependent effective mass, J. Math. Phys. 51, 2010, 092103.

[23] *A. Arda, R. Sever.* Bound State Solutions of Schr¨odinger Equation for Generalized Morse Potential with Position-Dependent Mass, Commun. Theor. Phys. 56, 2011, 51–54.

[24] *J.R.F. Lima, M. Vieira, C. Furtado, F. Moraes, C. Filgueiras.* Yet another position-dependent mass quantum model, J. Math. Phys. 53, 2012, 072101.

[25] *H. Rajbongshi.* ”Exactly solvable potentials and the bound-state solution of the position-dependent mass Schrodinger equation in *D*-dimensional space”, Theor. Math. Phys., 184, 996–1010 (2015).

[26] *N. Amir, S. Iqbal.* Algebraic solutions of shape-invariant position-dependent effective mass systems, J.Math.Phys., 2017, 57, 465202.

[27] *E.I. Jafarov, S.M. Nagiyev, R. Oste and J. Van der Jeugt.* Exact solution of the position-dependent effective mass and angular frequency Schrödinger equation: harmonic oscillator model with quantized confinement parameter, J. Physics A: Math.Theor. 2020, 53, 485301.

[28] *E.I. Jafarov, S.M. Nagiyev, A.M. Jafarova.* Quantum-mechanical explicit solution for the confined harmonic oscillator model with the Von Roos kinetic energy operator, Reports on Mathematical Physics, Vol. 86: 1, 2020, 25-37.

[29] *E.I. Jafarov, S.M. Nagiyev, A.M. Seyidova.* Zhu-Kroemer kinetic energy operator with position-dependent effective mass and exact solution of the non-relativistic confined harmonic oscillator model. AMEA-nın Xəbərləri, Fiz.-texn., riyaz. Ser., fizika və astronomiya №2, 2020, 3-14.

[30] *H. Bateman and A. Erd´elyi.* Higher Transcendental Functions: Vol. 2, McGraw Hill Publications, New York, 1953.

[31] *R. Koekoek, P. A. Lesky and R.F. Swarttouw.* Hypergeometric Orthogonal Polynomials and their q-Analogues, Springer, Berlin 2010.

[32] *A.F. Nikiforov and V.B. Uvarov.* Special Functions of Mathematical Physics: A Unified Introduction with Applications, Birkh¨auser, Basel 1988.

ANALYSIS OF FLUCTUATION CONDUCTIVITY IN $Y_{0,5}Cd_{0,5}Ba_2Cu_3O_{7-\delta}$

V.M. ALIEV, J.A. RAHIMOV[1], V.I. EMINOVA, G.A. ALIEVA[2]

Institute of Physics of the National Academy of Sciences of Azerbaijan, AZ 1143,
Baku, H. Javid Ave., 131
[1]Azerbaijan Medical University, AZ 1022, Baku, st. Bakikhanov, 23
[2]Institute INKhP NAS of Azerbaijan, AZ 1025, Baku, Khojaly ave. 30
v_aliev@bk.ru

The mechanism of the formation of excess conductivity in cuprate HTSCs $YBa_2Cu_3O_{7-\delta}$ and $Y_{0,5}Cd_{0,5}Ba_2Cu_3O_{7-\delta}$ was considered in the framework of the model of local pairs, taking into account the Aslamazov - Larkin theory near T_c^{mf}. The temperature Tcr of the transition from the 2D fluctuation region to the 3D region (the temperature of the 2D-3D crossover) is determined. The values of the coherence length of fluctuation Cooper pairs $\xi_c(0)$ along the c axis are calculated. It is shown that partial substitution of Y for Cd in the Y-Ba-Cu-O system leads to an increase in $\xi_c(0)$ by ~ 3.2 times (from 1.1 Å to 3.6 Å), as well as to an expansion as a region of existence pseudogap, and the region of superconducting (SC) fluctuations near T_c^{mf}. The temperature dependence of the pseudogap $\Delta^*(T)$ and the values of $\Delta^*(T_c^{mf})$ were determined, and the temperatures T_m (122.7K) corresponding to the maximum of the temperature dependence of the pseudogap in $Y_{0,5}Cd_{0,5}Ba_2Cu_3O_{7-\delta}$ were estimated. The maximum values of the pseudogap in the $Y_{0,5}Cd_{0,5}Ba_2Cu_3O_{7-\delta}$ sample are 660K.

INTRODUCTION

The anomalous properties of layered metal oxide high-temperature superconductors (HTSC) are one of the most important problems in modern solid-state physics [1]. In experiments on the charge transfer dynamics in such systems, a number of objective difficulties arise, including the rather complex crystal structure of HTSCs [2, 3], the nonuniform distribution of structural defects [4], the presence of intergrain boundaries and cluster inclusions [5], and the inhomogeneity of specific experimental samples [6], which is often caused by different technological prehistories, etc.

The physical properties of HTSCs are also unusual, especially in the normal state, where a pseudogap (PG) opens along the excitation spectrum at the characteristic temperature $T^* >> T_c$ [7, 8] (T_c is the critical temperature of the superconducting (SC) transition).

It is believed that the correct understanding PG physics, which remains one of the most intriguing properties of cuprates [9], will shed light on the SC pairing mechanism in HTSCs.

Since the discovery of HTSCs with active plane CuO_2 (cuprates), attempts have been made to improve their superconducting characteristics by isomorphic substitutions of one of the components [11, 12].

One of the most interesting materials for studying the properties of HTSCs is the $YBa_2Cu_3O_{7-\delta}$ (YBCO) compound, because it is possible to widely vary its composition by replacing yttrium with its isoelectronic analogues, or by changing the degree of oxygen non-stoichiometry. In YBCO, yttrium is replaced by a majority of lanthanides and other elements [1, 12-14], which usually does not lead to the deterioration of the compound's superconducting properties. Pr is an exception, since PrBCO is an insulator [15].

It is wellknown that ions of rare earth elements and K replace yttrium atoms. Accordingly, Sr is incorporated into the positions of Ba atoms, while other dopants are incorporated into the Cu(1) position [16]. However, this process is not well understood. The mechanisms of how a modification impacts the properties of HTSCs in underdoped and overdoped regimes remain unclear, which is important since fulfilling the conditions of these regimes is necessary to achieving the optimal properties of HTSC materials. The effect of substitution on fluctuation processes and the PG is, likewise, poorly understood. Therefore, the study of substitution in the classical structure of $YBa_2Cu_3O_{7-\delta}$ provides new data on the mechanism of superconductivity and the contribution made to superconductivity by Y, Ba, and Cu atoms.

HTSC materials are synthesized with partial substitution of Cd for Y in YBa2Cu3O*x*, because despite the fact that yttrium and cadmium are heterovalent, their ionic radii are similar (0.90 and 0.95 Å, respectively). This serves as the basis for such a substitution in YBaCuO.

The goal of this study is to investigate how possible defects and structural changes impact the physical parameters, fluctuation characteristics, and PG after substituting Cd $YBa_2Cu_3O_{7-\delta}$. A sample (Y1) $YBa_2Cu_3O_{7-\delta}$ and (Y2) $Y_{0,5}Cd_{0,5}Ba_2Cu_3O_{7-\delta}$ were studied. In this case, the resistivity $\rho(T)$ of the Y2 sample in the normal phase at 300 K in comparison with Y1 increases by almost 13 times.

The fluctuation conductivity (FLC) is analyzed within the framework of the Aslamazov–Larkin (AL) and Hikami–Larkin (CL) theories [17, 18]. Near *Tc*, the FLC of all samples, $\triangle\sigma(T)$, is perfectly described by the threedimensional (3D) equation of the AL theory, which is typical for HTSCs [1, 15]. To analyze the temperature dependence of the pseudogap, the model of local pairs proposed in [19] was used.

EXPERIMENTAL RESULTS AND THEIR PROCESSING

The $Y_{0.5}Cd_{0.5}Ba_2Cu_3O_{7-\delta}$ samples are prepared in two stages [12]. At the first step, the initial components, which are in a stoichiometric ratio, are mixed and annealed in air at a temperature of 1120 K for 25 h. At the second step, the resulting compositions are annealed in oxygen (P = 1.2–1.5 atm) at a temperature of 1190 K for 25 h, and slowly cooled to room temperature. In this work, we analyze the results of replacing Y with Cd at x = 0.5.
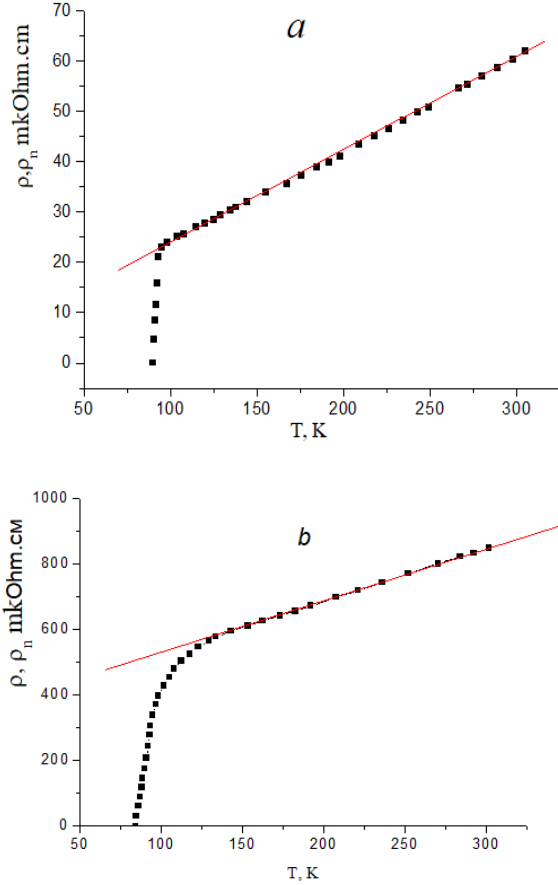

Fig. 1. Temperature dependences of the resistivity of the samples $YBa_2Cu_3O_{7-\delta}$ (a) and $Y_{0.5}Cd_{0.5}Ba_2Cu_3O_{7-\delta}$ (b). Straight lines denote ρ_n (T) extrapolated to low temperatures.

Samples 8×4×3 mm in size are cut from compressed tablets (12 mm diameter and 3 mm thickness) of synthesized polycrystalline material. The electrical resistance is measured according to the standard four-probe method. The current contacts are created by applying a silver paste and subsequently connecting silver conductors with 0.05 mm diameters to the ends of the polycrystalline sample, in order to ensure the current spreads across it in a uniform manner. The potential contacts located at the middle of the sample's surface are created in a similar way. Then, a three-hour annealing process is carried out at a temperature of 200 °C in an oxygen atmosphere. This procedure makes it possible to obtain a contact transition resistance of 1 Ω and to perform resistive

measurements at transport currents of up to 10 mA in the *ab*-plane.

The temperature dependences of the resistivity ρ (T) = ρab (T) of the synthesized polycrystals Y1 and Y2 are shown in Fig. 1. The ρ(T) dependences at different values of have a shape characteristic of optimally doped HTSCs [20]. One exception is the nonlinear dependence ρ(T) at Y1, ρ(T) ~ T^2, which is typical for overdoped cuprates [20]. Analysis shows that the data in this case are well approximated by the equation ρ(T) = ρ_0 + B_1(T) + B_2 (T)^2 with the parameters ρ_0 = 9.07, B_1 = 0.1442, and B_2 = 0.0000957, obtained by approximating data using the Origin computer program. The coefficient of the quadratic term is very small, but nonzero. Thus, we have an overdoped sample. This result is particularly interesting, since it is impossible to obtain an overdoped sample of $YBa_2Cu_3O_{7-\delta}$ simply by oxygen intercalation. The maximum that can be obtained is δ = 0 and an oxygen index 7– δ = 7, at T_c ~ 92 K [20]. It is most likely that such a dependence ρ(T) is specific to this polycrystalline sample.

As seen in Fig. 1, the critical temperatures of the samples of the Y – Ba – Cu – O system upon doping with Cd in the considered case remain up to ~ 85 K. In this case, the resistivity ρ (T) of the Y2 samples in the normal phase at 300 K in comparison with $YBa_2Cu_3O_{7-\delta}$ increases by almost 13 times.

To determine the temperature of the beginning of the formation of local pairs [3,4] in the samples (T *), the criterion [ρ (T) −ρ_0] / aT = 1 was used, which reflects the transformation of the equation of a straight line [39], where $\rho 0$ is the residual resistance cut off by this line on the Y axis at T=0. In this case, it is defined as the temperature of deviation of ρ (T) from 1.

FLUCTUATION CONDUCTIVITY

The linear course of the temperature dependence of the specific resistance of samples Y1 and Y2 in the normal phase is well extrapolated by the expressions ρ_n(T) = (D+ κT +BT^2) and ρ_n(T) = (ρ_0+ κT +BT^2) (here D, B and k are some constants). This linear relationship, extrapolated to the low temperature range, was used to determine excess conductivity $\Delta\sigma$(T according to:

$$\Delta\sigma(T) = \rho^{-1}(T) - \rho v^{-1}(T). \qquad (1)$$

The analysis of the behavior of excess conductivities was carried out in the framework of the local pair model [4].

Assuming the possibility of the formation of local pairs [(3), 4] in the Y2 sample at temperatures below T * = 136.6 K, the experimental results obtained near Tcmf were analyzed taking into account the occurrence of fluctuation Cooper pairs (PCPs) above Tc within the framework of the Aslamazov - Larkin theory (AL) [17] (fiq.2).

The Fig. 2 shows dependence of the logarithm of the excess conductivity of the samples Y1 (1) and Y2 (2) on the logarithm of the reduced temperature ε = (T / T_c^{mf}-1). According to the theory of AL, as

well as Hikami – Larkin (HL) developed for HTSC [18], in the region of $T>T_c$ (but near T_c^{mf}), the fluctuation coupling of charge carriers occurs, leading to the appearance of fluctuation conductivity (FC). In this region, the temperature dependence of excess conductivity on temperature is described by the expressions:

$$\Delta\sigma_{AL3D} = C_{3D}\{e^2/[32\hbar\xi_c(0)]\}\varepsilon^{-1/2}, \qquad (2)$$

$$\Delta\sigma_{AL2D} = C_{2D}\{e^2/[16\hbar d]\}\varepsilon^{-1}, \qquad (3)$$

respectively for three-dimensional (3D) and two-dimensional (2D) region. The scaling coefficients C are used to combine the theory with experiment [4].
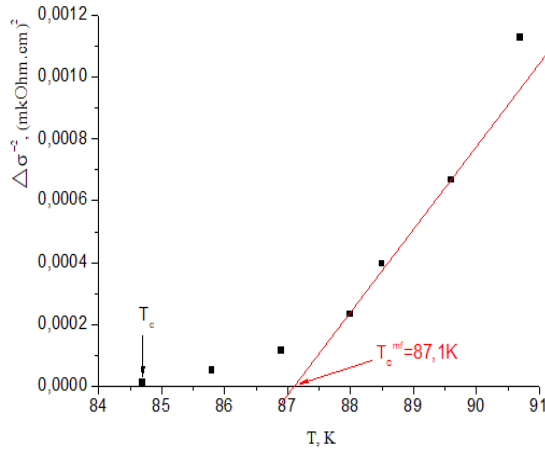

Fig.2. Temperature dependence of the inverse square of the excess conductivity $\Delta\sigma^{-2}$ (T) of the $Y_{0,5}Cd_{0,5}Ba_2Cu_3O_{7-\delta}$ polycrystal.
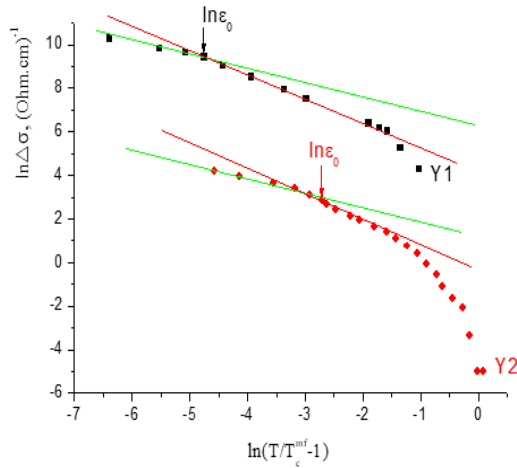

Fig. 3. Dependences of the excess conductivity logarithm on ln (T / T_c^{mf} -1) for samples Y1 and Y2. Solid lines - calculation within the framework of the Aslamazov-Larkin theory.

Thus, by the angle of inclination α of dependences ln ($\Delta\sigma$) as a function of ε = ln (T / T_c^{mf}-1) (see Fig. 3), we can distinguish 2D (tgα = -1) and 3D (tgα = - 1/2) regions of phase transition. It can also determine the crossover temperature T_0 (the transition

temperature from $\Delta\sigma_{2D}$ to σ_{3D}) and the tangents of the slopes of the dependences $\Delta\sigma(T)$ corresponding to the exponents ε in equations (2) and (3). The corresponding values of the parameters 2D and 3D regions determined from the experiment for sample Y1 are 2D (tgα = -1.04) and 3D (tgα = -0.5) and for Y2 2D (tgα = -1) and 3D (tgα = -0.5).

On basis of value the temperature of the crossover T_0, which corresponds to lnε_0, according to Fig. 3, it can determine the coherence length of local pairs along the c axis [18,19]:

$$\xi_c(0) = d\sqrt{\varepsilon}_0 , \qquad (4)$$

here d $\approx$ 11.7Å is the distance between the inner conducting planes in Y-Ba-Cu-O [20]. The values of ξ_c (0) = 1.1 Å (lnε_0 $\approx$ -1.2318) for Y1 and ξ_c (0) = 3.6 (lnε_0 $\approx$ -2.347) for Y2 was obtained, accordingly.

ANALYSIS OF THE MAGNITUDE AND TEMPERATURE DEPENDENCE OF THE PSEUDOGAP

As noted above, in the cuprates at T<T *, the density of electron states of quasiparticles on the Fermi level decreases [21] (the cause of this phenomenon is not yet fully elucidated), which creates conditions for the formation of a pseudogap in the excitation spectrum and it leads ultimately to the formation of an excess conductivity. The magnitude and temperature dependence of the pseudogap in the investigated samples was analyzed using the local pair model, taking into account the transition from Bose-Einstein condensation (SCB) to the BCS mode predicted by the theory [18] for HTSC when the temperature decreases in the interval T * <T <T_c. Note that excess conductivity exists precisely in this temperature range, where fermions supposedly form pairs - the so-called strongly coupled bosons (PRS). The pseudogap is characterized by a certain value of the binding energy ε_b~$1/\xi^2(T)$, causing the creation of such pairs [18], which decreases with temperature, because the coherence length of the Cooper pairs $\xi(T)=\xi(0)(T/T_c-1)^{-1/2}$, on the contrary, increases with decreasing temperatures. Therefore, according to the LP_model, the SCB are transformed into the FCP when the temperature approaches T_c (BEC-BCS transition), which becomes possible due to the extremely small coherence length ξ (T) in cuprates.

From our studies, we can estimate the magnitude and temperature dependence of PG, based on the temperature dependence of excess conductivity in the entire temperature range from T * to T_c^{mf} according to [21]:

$$\Delta\sigma(\varepsilon) = \left\{\frac{A(1-T/T^*)[\exp(-\Delta^*/T)]e^2}{16\hbar\xi_c(0)\sqrt{2\varepsilon_0^* \cdot sh(2\varepsilon/\varepsilon_0^*)}}\right\} \qquad (5)$$

where the (1-T / T *) determines the number of pairs formed at T $\leq$ T *: and the exp (-Δ */T) determines the

number of pairs destroyed by thermal fluctuations below the BEC-BCS transition temperature. The

coefficient A has the same meaning as the coefficients C_{3D} and C_{2D} in (2) and (3).

The solution of equation (5) gives the value of $\Delta *$:

$$\Delta^*(T) = T \cdot \ln \left\{ \frac{A(1 - T/T^*)e^2}{\Delta\sigma(T)16\hbar\xi_c(0)\sqrt{2\varepsilon_0^* \cdot sh(2\varepsilon/\varepsilon_0^*)}} \right\} \qquad (6)$$

where $\Delta\sigma$ (T) is the experimentally determined excess conductivity.
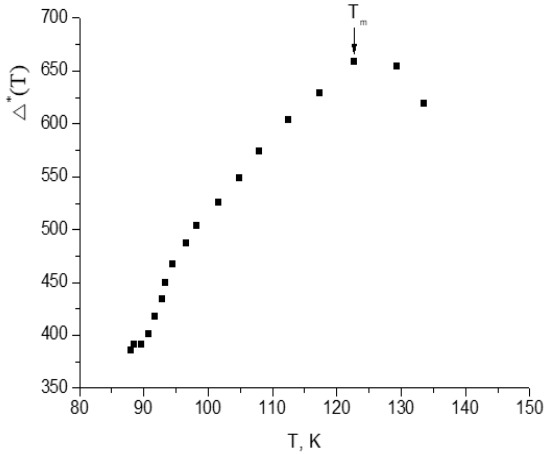

Fig.4. Temperature dependences of the calculated pseudogap for the sample Y2. The arrows show the maximum values of the pseudogap value.

The temperature dependence and the value of the pseudogap parameter $\Delta * (T)$ (Fig. 4) were calculated based on equation (6). with the parameters given above. Note that no PG is observed in Y1, since the sample is in overdoped mode. As noted in [21], the value of the coefficient A is selected from the condition of coincidence of the temperature dependence of $\Delta\sigma$ equation (5), assuming $\Delta* = \Delta*(T)$). with experimental data in the region of 3D fluctuations near T_c. According to [21, 22], the optimal approximation for the HTSC material is achieved with values of $2\Delta*(T)/K_B T \approx 5 \div 7$. For sample Y2, the $2\Delta*(T_c)/K_B T_c = 5$. As a result, from the LP analysis for Y2, the values A=6.95 and $\Delta(T_c^{mf}) = 87,1 \cdot 2,5 = 217,7K$, were obtained, which is consistent with the experimental data.

The temperature dependences of $\Delta*(T)$ obtained on the basis of equation (6) are in Fig. four. The maximum values of the pseudogap for Y2 $\Delta * (T_m) \approx$ 660 K, $T_m = 122,7K$ have been determined.

From the presented data in Fig. 4, it is also seen that as T decreases, the pseudogap value first increases, then, after passing through a maximum, decreases.

This decrease is due to the transformation of the SCB in the PCF as a result of the BEC-BCS transition, which accompanied by an increase in excess conductivity at T→T_c. Such a behavior of $\Delta *$ with decreasing temperature was first found on YBCO films [21,22] with different oxygen contents, which seems to be typical of cuprate HTSC [21]. Thus, we can come to the conclusion that in the $Y_{0,5}Cd_{0,5}Ba_2Cu_3O_{7-\delta}$ investigated by us, the formation of local pairs of charge carriers at T>>T_c^{mf} is possible, which creates conditions for the formation of a pseudogap [21,22] with the subsequent establishment of the phase coherence of fluctuation Cooper vapor at T<T_c^{mf}.

CONCLUSION

The investigation of the effect of partial substitution of Y bu Cd on the mechanism of excess conductivity in Y-Ba-Cu-O polycrystals showed that partial substitution of Y by Cd leads to a decrease in the critical temperatures of the $Y_{0,5}Cd_{0,5}Ba_2Cu_3O_{7-\delta}$ (Y2) sample compared to $YBa_2Cu_3O_{7-\delta}$ (Y1) (respectively T_c^{mf}(Y2)=87,1K и T_c^{mf}(Y1)=91,99K T_c). In this case, the resistivity of the $Y_{0,5}Cd_{0,5}Ba_2Cu_3O_{7-\delta}$ sample in the normal phase at 300 K increases (13 times) as compared to $YBa_2Cu_3O_{7-\delta}$, and the increase in the coherence length of Cooper pairs is 3.27 times (1.1 and 3.6 Å, respectively).

Studies and analysis have shown that the excess conductivity $\Delta\sigma$ (T) in $Y_{0,5}Cd_{0,5}Ba_2Cu_3O_{7-\delta}$ in the temperature range T_c^{mf}<T<T^* is satisfactorily described in the framework of the model of local pairs.

The result of the analysis of the pseudogap state by the excess conductivity method confirmed that the model of local pairs in this case is applicable for the $Y_{0,5}Cd_{0,5}Ba_2Cu_3O_{7-\delta}$ image.

[1] *R.V. Vovk, A.L. Solovyev.* LTP 44, 111 (2018) [Low Temp. Phys. 2018, 44, 81].

[2] *R.J. Cava.* Science 1990, 243, 656.

[3] *M. Asta, D. de Futaine, G. Ceder, E. Salomons, and M. Kraitchman.* J. Less. Common. Metals 1991, 168, 39.

[4] *R.V. Vovk, N.R. Vovk, and O.V. Dobrovolskiy.* J. Low Temp. Phys. 2014, 175, 614.

[5] *R.V. Vovk, Z.F. Nazyrov, M.A. Obolenskii, I.L. Goulatis, A. Chroneos, and V.M. Pinto Simoes.* J. Alloys Compd. 2011, 509, 4553.

[6] *S.V. Savich, A.V. Samoilov, R.V. Vovk, O.V. Dobrovolskiy, S.N. Kamchatna, Ya.V. Dolgopolova, and O.A. Chernovol-Tkachenko.* Mod. Phys. Lett. B 30, 2016, 1650034.

[7] *T. Timusk and B. Statt.* Reports Prog. Phys. 62, 61 (1999).

[8] *S. Badoux, W. Tabis, F. Laliberte, G. Grissonnanche, B. Vignolle, D. Vignolles, J. Beard, D. A. Bonn, W. N. Hardy, R. Liang, N. Doiron-Leyraud, Louis Taillefer, and Cyril Proust.* Nature (London) 531, 210 (2016).

[9] *A.A. Kordyuk.* Fiz. Nizk. Temp. 2015, 41, 417 [Low Temp. Phys. 2015, 41, 319].

[10] *A.L. Solovyev, V.M. Dmiriyev.* LTP 33, 32, 2007. [Low Temp. Phys. 2007, 33, 23].

[11] *R.V. Vovk, M.A. Obolenskii, A.A. Zavgorodnii, A.V. Bondarenko, M.G. Revakin.* LTP 33, 2007, 546. [Low Temp. Phys. 33, 408, 2007].

[12] *S.A. Aliev, J.A. Baghirov, S.S. Ragimov, SA. Huseyhov, V. M. Aliev, I.A. Ismailov, and A.Sh. Mechtiev.* Proc. 2nd Intern. Conf. on Rare Earth Development and Application V, Beijing, China 1991.

[13] *V.M. Aliev.* Transactions of Azerbaijan National Academy of Sciences Physics and Astronomy 32(2), 2012, 110.

[14] *E.A. Gudilin, A.P. Soloshenko, V.V. Lennikov, A.V. Knotko, D.A. Vetoshkin, N.N. Oleynikov, Y.D. Tretyakov.* Journal of inorganic chemistry, 2000, 45, 917.

[15] *A.L. Solovyev, L.V. Omelchenko, R.V. Vovk, S.N. Kamchatnaya.* LTP 43, 1050, 2017. [Low Temp. Phys. 43, 841, 2017].

[16] *G.D. Chryssikos, E.I. Kamitsos, J.A. Kapoutsis, A.P. Patsis, V. Psycharis, A. Kafoudakis, C. Mitros, G. Kallias, E. Gamari-Seale, and D. Niarchos.* Physica C 254, 1995, 44.

[17] *L.G. Aslamazov and A.I. Larkin.* Phys. Lett. A 26, 1968, 238.

[18] *S. Hikami and A.I. Larkin.* Mod. Phys. Lett. B 2, 1988, 693.

[19] *I. Esterlis, S. A. Kivelson, and D. J. Scalapino.* Phys. Rev. B 99, 2019, 174516.

[20] *Y. Ando, S. Komiya, K. Segawa, S. Ono, and Y. Kurita.* Phys. Rev. Lett. 93, 267001 (2004).

[21] *A.L. Solovyev, V.M. Dmitriyev.* Fluctuation conduction and pseudogap in high-temperature supersemiconductors YBCO, LTP, 35, 3, 2009, 227-264.

[22] *V.V. Florentyev, A.V. Inushkin, A.N. Taldenkov.* Thermal conduction of single crystals $LnBa_2Cu_3O_{7-\delta}$, Superconduction: physics, chemistry, technology, 1990, 3, 10, ч.2, 1990, 2302-2319.

NEUTRALINO PAIR PRODUCTION IN POLARIZED LEPTON-ANTILEPTON COLLISIONS

S.K. ABDULLAYEV, M.Sh. GOJAYEV, A.K. GULAYEVA

Baku State University, Baku, Z. Khalilov st., 23, Azerbaijan, AZ 1148
m_qocayev@mail.ru

The process of producing a neutralino pair in arbitrarily polarized lepton-antilepton (electron-positron or muon-antimuon) collisions has been studied within the Minimal Supersymmetric Standard Model: $\ell^- + \ell^+ \to \tilde{\chi}_i^0 + \tilde{\chi}_j^0$. We consider s-channel diagrams with neutral Z-boson and Higgs-boson H (h or A) exchanges, and t-channel diagrams with scalar $\tilde{\ell}_L^-$ and $\tilde{\ell}_R^+$-lepton exchanges. General expressions for the differential and integral cross sections of the process are obtained, transverse and longitudinal spin asymmetries due to lepton-antilepton pair polarizations, and degrees of longitudinal and transverse neutralino polarization are determined. Angular and energy dependences of cross sections and polarization characteristics of the process are studied in detail.

Keywords: Standard Model, Minimal Supersymmetric Standard Model, lepton-antilepton pair, neutralino, Higgs boson, effective cross section.
PACS: 11.30.Pb, 14.80.Da, 14.70.Nb

1. INTRODUCTION

The discovery of a scalar Higgs boson with characteristics corresponding to the Standard Model (SM) predictions was made at the Large Hadron Collider (LHC) by the ATLAS and CMS collaborations in 2012. [1, 2] (see also reviews [3-5]). With its discovery the missing brick in the CM building was found. The way to the discovery was long and the fact of the discovery itself meant the beginning of great work to verify the validity of the detected signal and clarify its nature, determining the properties of the new particle.

Higgs boson H_{SM} is unstable particle and can decay through different channels. It was discovered at the LHC by studying decays to two photons ($H_{\text{SM}} \to \gamma + \gamma$), decays to two vector bosons ZZ^* and WW^* (here Z^* and W^*-virtual bosons). Neutral bosons Z were identified by decay channels into two leptons: e^-e^+- or $\mu^-\mu^+$-pair. This is written as $H_{\text{SM}} \to ZZ^* \to 4\ell$, where ℓ – one of the leptons is $e^\mp, \mu^\mp$. The decays of the W-boson pair were identified by the channel $H_{\text{SM}} \to WW^* \to \ell\nu\ell\nu$, where ν – is the electron or muon neutrino.

Based on the decay of the Higgs boson into two photons $H_{\text{SM}} \to \gamma + \gamma$ its mass is found to be $M_{H_{\text{SM}}}(\gamma\gamma) = 126.0\pm0.4$ (stat.) ±0.4 (syst.) GeV [1]. For the decay to four leptons $M_{H_{\text{SM}}}(4\ell) = 126.8\pm0.2$ (stat.)±0.7 (syst.) GeV [6]. For a complete picture it is useful to cite the results of the CSM experiment [2], which performed the discovery of a new particle simultaneously with the ATLAS collaboration: $M_{H_{\text{SM}}}(\gamma\gamma) = 125.3\pm0.4$ (stat.)±0.5 (syst.) GeV. A mass value of $M_{H_{\text{SM}}}(4\ell) = 125.6\pm0.4$ (stat.)±0.2 (system.) GeV was found for the decay channel

$H_{\text{SM}} \to ZZ^* \to 4\ell$. Consequently, the results of the ATLAS and CSM collaborations match the mass of the Higgs boson.

SM is a successful theory that describes all known elementary particles and strong, electromagnetic, weak interactions between them (the gravitational interaction so far is described by Einstein's general theory of relativity). On the basis of SM one can make accurate calculations and compare them with the corresponding experimental data. The agreement between SM and experiment is strikingly good.

However, SM has its shortcomings. For example, the key point of SM is the Higgs mechanism of electrically weak symmetry, which successfully describes the generation of elementary particle masses. Unfortunately, SM does not give any explanation why there is a Higgs field at all and why it has such property – to form a vacuum condensate.

The second shortcoming of SM is connected with renormalization of the Higgs boson mass. The fact is that for all SM particles the mass renormalization works well. However, in the case of the Higgs boson virtual particles have a strong influence on the mass by trillions of times. Inside SM there is no constraint stopping the Higgs boson mass growth at the expense of virtual particles. This drawback can be eliminated in the following way. If some other particles exist in nature, they in virtual form can compensate their influence on Higgs boson mass. The most important thing here is that in the Minimal Supersymmetric Standard Model (MSSM) such compensation arises by construction of the theory itself. It is such theories that most attract physicists.

According to SM, neutrinos ν_e, ν_μ and ν_τ are massless particles. However, experiments prove that neutrinos have mass, and in addition, they are very actively mixing with each other, passing from one kind to another. All this suggests that the mass and mixing of neutrinos is not due to the Higgs mechanism, but to a phenomenon of some other nature.

Again, there are no such phenomena in SM, while there are plenty of such mechanisms in models outside of SM.

The absence of dark matter particles in SM is one of the difficulties of this model. Astro-physicists believe that in the Universe, besides ordinary matter in the form of stars, black hole planets, gas-dust clouds, neutrinos, etc., there are also particles of a completely different nature. We do not see these particles, they are neutral and practically do not interact with ordinary matter and radiation. In the SM there is not a single particle suitable for this role. However, in the MSSM there are such particles as neutralino, sneitrino, gluino, gravitino, which may be candidates for dark matter.

The above facts and a number of other reasons indicate the need to go beyond SM. In this case, the main attention is paid to the MSSM [7-10]. In this model, in contrast to SM, two scalar field doublets with hypercharges –1 and +1 are introduced:

$$\varphi_1 = \begin{pmatrix} H_1^0 \\ H_1^- \end{pmatrix}, \quad \varphi_2 = \begin{pmatrix} H_2^+ \\ H_2^0 \end{pmatrix}.$$

To obtain the physical fields of Higgs bosons and determine their masses, the scalar fields φ_1 and φ_2 decompose into real and imaginary parts around the vacuum

$$\varphi_1 = \frac{1}{\sqrt{2}} \begin{pmatrix} \upsilon_1 + H_1^0 + iP_1^0 \\ H_1^- \end{pmatrix},$$

$$\varphi_2 = \frac{1}{\sqrt{2}} \begin{pmatrix} H_2^+ \\ \upsilon_2 + H_2^0 + iP_2^0 \end{pmatrix},$$

where $<\varphi_1> = \frac{1}{\sqrt{2}}\upsilon_1$ and $<\varphi_2> = \frac{1}{\sqrt{2}}\upsilon_2$ are the vacuum values of the Higgs boson fields. Mixing the fields H_1^0 and H_2^0 obtain the CP-even H and h Higgs bosons (mixing angle α):

$$\begin{pmatrix} H \\ h \end{pmatrix} = \begin{pmatrix} \cos\alpha & \sin\alpha \\ -\sin\alpha & \cos\alpha \end{pmatrix} \begin{pmatrix} H_1^0 \\ H_2^0 \end{pmatrix}.$$

Similarly mix the fields P_1^0 and P_2^0 ($H_1^\pm$ and $H_2^\pm$) and obtain a Goldston G^0-boson and CP odd Higgs boson A (charged Goldston $G^\pm$- and Higgs bosons $H^\pm$) (mixing angle β):

$$\begin{pmatrix} G^0 \\ A \end{pmatrix} = \begin{pmatrix} \cos\beta & \sin\beta \\ -\sin\beta & \cos\beta \end{pmatrix} \begin{pmatrix} P_1^0 \\ P_2^0 \end{pmatrix},$$

$$\begin{pmatrix} G^\pm \\ H^\pm \end{pmatrix} = \begin{pmatrix} \cos\beta & \sin\beta \\ -\sin\beta & \cos\beta \end{pmatrix} \begin{pmatrix} H_1^\pm \\ H_2^\pm \end{pmatrix}.$$

Thus, there are five Higgs bosons in the MSSM: the CP-even H and h-bosons, the CP-odd A-boson, and the charged H^+- and H^--bosons. The Higgs sector is characterized by the mass parameters M_H, M_h, M_A, $M_{H^\pm}$ and the mixing angles of the scalar fields α and β. Of these, only two parameters are considered to be free: the mass M_A and the angle $tg\beta = \upsilon_2/\upsilon_1$. The other parameters are expressed through them:

$$M_{H(h)}^2 = \frac{1}{2}[M_A^2 + M_Z^2 \pm \sqrt{(M_A^2 + M_Z^2)^2 - 4M_A^2 M_Z^2 \cos^2 2\beta}], \quad M_{H^\pm}^2 = M_A^2 + M_Z^2,$$

$$tg2\alpha = tg2\beta \frac{M_A^2 + M_Z^2}{M_A^2 - M_Z^2}, \quad \left(-\frac{\pi}{2} \le \alpha < 0\right),$$

where M_W and M_Z – are the masses of gauge $W^\pm$- and Z-bosons.

The supersymmetric (SUSY) partners of gauge $W^\pm$- and Higgs $H^\pm$-bosons are calibrino $\widetilde{W}^\pm$ and higgsino $\widetilde{H}^\pm$. These spinor fields mix and new chargino $\widetilde{\chi}_{1,2}^\pm$ states appear. The neutral counterparts of charginos are called neutralinos and there are four

of them $\widetilde{\chi}_j^0$ ($j = 1, 2, 3\ 4$). They arise as a result of mixing binos $\widetilde{B}^0$, vino $\widetilde{W}_3^0$ and higgsinos $\widetilde{H}_1^0$, $\widetilde{H}_2^0$. The mass matrix of the neutralino is non-diagonal and depends on the mass parameters wine M_2, higgsino μ and wine M_1, as well as on the parameter $tg\beta$ [7, 8, 11-13]:

$$M_N = \begin{pmatrix} M_1 & 0 & -M_Z \sin\theta_W \cos\beta & M_Z \sin\theta_W \sin\beta \\ 0 & M_2 & M_Z \cos\theta_W \cos\beta & -M_Z \cos\theta_W \sin\beta \\ -M_Z \sin\theta_W \cos\beta & M_Z \cos\theta_W \cos\beta & 0 & -\mu \\ M_Z \sin\theta_W \sin\beta & -M_Z \cos\theta_W \sin\beta & -\mu & 0 \end{pmatrix}.$$

This matrix can be diagonalized by one real matrix Z. Expressions of the matrix elements of this matrix Z_{ij} ($i, j = 1, 2, 3\ 4$) and the neutralino mass are given in [11, 13]. For large values of the parameter $|\mu| \gg M_{1,2} \gg M_Z$, the masses of the neutralino are:

$$m_{\chi_1^0} \approx M_1 - \frac{M_Z^2}{\mu^2}(M_1 + \mu\sin 2\beta)\sin^2\theta_W,$$

$$m_{\chi_2^0} \approx M_2 - \frac{M_Z^2}{\mu^2}(M_2 + \mu\sin 2\beta)\cos^2\theta_W,$$

$$m_{\chi_{3/4}^0} \approx |\mu| + \frac{M_Z^2}{2\mu^2}\varepsilon_\mu(1 \mp \sin 2\beta)(\mu \pm M_2\sin^2\theta_W \mp M_1\cos^2\theta_W),$$

θ_W – Weinberg angle, $\varepsilon_\mu = \dfrac{\mu}{|\mu|}$ – sign of the parameter μ. At $|\mu| \to \infty$ two neutralinos correspond to the calibrino state with masses $m_{\chi_1^0} \approx M_1$ and $m_{\chi_2^0} \approx M_2$, and other neutralinos correspond to the higgsino state with masses $m_{\chi_3^0} \approx m_{\chi_4^0} \approx |\mu|$.

Supersymmetric (SUSY) chargino and neutralino particles can be born in the LHC in cascade decays of squarks and gluinos: $\tilde{g} \to q\tilde{q}$, $\tilde{q} \to q\tilde{\chi}_i$. Note that chargino or neutralino pairs can be born in high-energy lepton-antilepton (electron-positron and muon-antimuon) colliders:

$$\ell^- + \ell^+ \to \tilde{\chi}_i^- + \tilde{\chi}_j^+, \quad \ell^- + \ell^+ \to \tilde{\chi}_i^0 + \tilde{\chi}_j^0.$$

These processes in the case of nonpolarized initial and final particles are considered in [14, 15]. The production of SUSY particles with spin 0 or 1/2 in polarized electron-positron collisions has been studied in [16-18]. In previous papers [19, 20] we have considered the process of chargino pair production in arbitrarily polarized lepton-antilepton interactions. Diagrams with photon and Z-boson exchange, with Higgs boson exchange H (h or A), and with scalar neutrino $\tilde{\nu}_L$ exchange have been studied in detail. It is found that in diagrams with photon and Z-boson exchange the lepton and antilepton must have opposite helicities ($\ell_R^-\ell_L^+$ or $\ell_L^-\ell_R^+$); in diagrams with Higgs boson exchange H (h or A) the lepton and antilepton must have identical helicities ($\ell_L^-\ell_L^+$ or $\ell_R^-\ell_R^+$); the diagram with sneutrino $\tilde{\nu}_L$ exchange is characterized by the fact that the lepton and antilepton can have only the left helicity ($\ell_L^-\ell_L^+$).

The purpose of the present paper is to study the process of neutralino pair production in arbitrarily polarized lepton-antilepton collisions

$$\ell^- + \ell^+ \to \tilde{\chi}_i^0 + \tilde{\chi}_j^0, \tag{1}$$

here $\ell^-\ell^+$ – is the lepton-antilepton (electron-positron and or muon-antimuon) pair, $\tilde{\chi}_i^0\tilde{\chi}_j^0$ – neutralino pair. Within the MSSM framework and taking into account the arbitrary polarizations of the lepton-antilepton pair, a general expression for the effective cross section of the process (1) is obtained. The longitudinal and transverse spin asymmetries due to the lepton-antilepton pair polarizations and the degrees of longitudinal and transverse neutralino polarization were determined. In particular, it is shown that the longitudinal spin asymmetry arising from the annihilation of longitudinally polarized leptons with nonpolarized antileptons is equal in magnitude and opposite in sign to the asymmetry arising from the annihilation of longitudinally polarized antileptons with nonpolarized leptons.

2. THE AMPLITUDE AND CROSS SECTION OF THE PROCESS $\ell^-\ell^+ \to (Z^*) \to \tilde{\chi}_i^0\tilde{\chi}_j^0$

The annihilation of a lepton-antilepton pair into a neutralino pair is described by the Feynman diagrams in Fig. 1. Diagram a) s-channel diagram with Z-boson exchange, diagram b) also s-channel diagram with Higgs boson exchange H (h or A) (this diagram plays an important role in muon-antimuon annihilation). Diagrams c) and d) are t-channel diagrams with an exchange of sleptons $\tilde{\ell}_L$ and $\tilde{\ell}_R$.
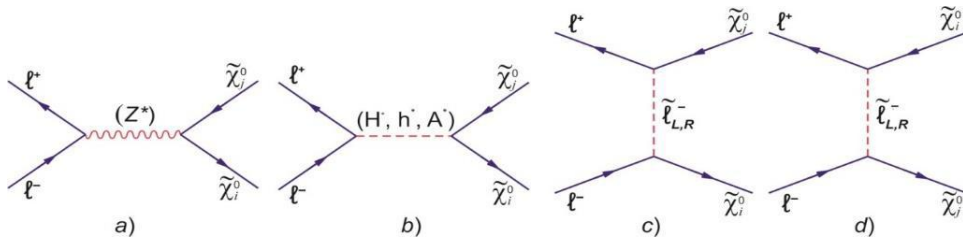

Fig. 1. Feynman diagrams for the reaction $\ell^-\ell^+ \to \tilde{\chi}_i^0\tilde{\chi}_j^0$.

The Lagrangians of the Z-boson interactions with a lepton-antilepton pair and neutralino pair are written in the following form:

$$L_{Z\ell\ell} = -\frac{ig}{\cos\theta_W}\bar{\ell}\gamma_\mu(g_L P_L + g_R P_R)\ell Z_\mu, \qquad (2)$$

$$L_{Z\tilde{\chi}_i^0\tilde{\chi}_j^0} = \frac{ig}{2\cos\theta_W}\bar{\tilde{\chi}}_i^0\gamma_\mu(g_{Z\tilde{\chi}_i^0\tilde{\chi}_j^0}^L P_L + g_{Z\tilde{\chi}_i^0\tilde{\chi}_j^0}^R P_R)\tilde{\chi}_j^0 Z_\mu, \qquad (3)$$

here $g = \dfrac{e}{\sin\theta_W}$ – is the electroweak interaction constant, g_L and g_R ($g_{Z\tilde{\chi}_i^0\tilde{\chi}_j^0}^L \equiv G_L$ and $g_{Z\tilde{\chi}_i^0\tilde{\chi}_j^0}^R \equiv G_R$) – are the left and right interaction constants of the lepton (neutralino) with the Z-boson:

$$g_L = -\frac{1}{2} + \sin^2\theta_W, \quad g_R = \sin^2\theta_W, \qquad (4)$$

$$G_L = -\frac{1}{2\sin\theta_W}[Z_{i3}Z_{j3} - Z_{i4}Z_{j4}], \quad G_R = \frac{1}{2\sin\theta_W}[Z_{i3}Z_{j3} - Z_{i4}Z_{j4}], \qquad (5)$$

$P_{L,R} = \dfrac{1}{2}(1 \pm \gamma_5)$ – kirality matrices.

Diagram (a) of Fig. 1 corresponds the amplitude

$$M_{i\to f}^{(Z)} = \frac{g^2}{2\cos^2\theta_W}\bar{\upsilon}(p_2,s_2)\gamma_\mu(g_L P_L + g_R P_R)u(p_1,s_1)\cdot D_Z(s)\times$$

$$\times \bar{u}_i(k_1,s)\gamma_\mu(G_L P_L + G_R P_R)\upsilon_j(k_2,s'), \qquad (6)$$

where $p_1(s_1)$, $p_2(s_2)$, $k_1(s)$ and $k_2(s')$ – are the 4-momentum (polarization vectors) of the lepton, antilepton, and neutralino $\tilde{\chi}_i^0$ and $\tilde{\chi}_j^0$, $D_Z(s) = (s - M_Z^2 + i\Gamma_Z M_Z)^{-1}$, $s = (p_1 + p_2)^2$ – is the square of the total energy of the lepton-antilepton pair, Γ_Z – is the total width of the Z-boson.

We find in the standard way for the modulus of the square of the amplitude (6):

$$\left|M_{i\to f}^{(Z)}\right|^2 = \frac{g^4|D_Z(s)|^2}{4\cos^4\theta_W}L_{\mu\nu}\times\chi_{\mu\nu}, \qquad (7)$$

where the expressions for the lepton $L_{\mu\nu}$ and neutralino $\chi_{\mu\nu}$ tensors are given in the Appendix.

In the case when the lepton-antilepton pair is polarized arbitrarily and summation is performed on the polarization neutralino states, the expression for the modulus of the amplitude square (6) is obtained:

$$\left|M_{i\to f}^{(Z)}\right|^2 = \frac{g^4|D_Z(s)|^2}{4\cos^4\theta_W}\{(G_L^2 + G_R^2)[(k_1\cdot p_1)(k_2\cdot p_2) + (k_1\cdot p_2)(k_2\cdot p_1) -$$

$$- m_\ell^2((k_1\cdot s_1)(k_2\cdot s_2) + (k_1\cdot s_2)(k_2\cdot s_1))) + 2g_L g_R((p_1\cdot s_2)((k_1\cdot s_1)(k_2\cdot p_2) + (k_2\cdot s_1)(k_1\cdot p_2) -$$

$$- (p_1\cdot p_2)((k_1\cdot s_1)(k_2\cdot s_2) + (k_1\cdot s_2)(k_2\cdot s_1)) + (p_2\cdot s_1)((k_1\cdot s_2)(k_2\cdot p_1) + (k_2\cdot s_2)(k_1\cdot p_1) -$$

$$- (k_1\cdot k_2)(p_1\cdot s_2)) - (s_1\cdot s_2)((k_1\cdot p_1)(k_2\cdot p_2) + (k_1\cdot p_2)(k_2\cdot p_1) - (k_1\cdot k_2)(p_1\cdot p_2)) +$$

$$- (g_L^2 - g_R^2)m_\ell((k_1\cdot p_1)(k_2\cdot s_2) + (k_2\cdot p_1)(k_1\cdot s_2) - (k_1\cdot p_2)(k_2\cdot s_1) - (p_2\cdot k_2)(k_1\cdot s_1)] +$$

$$+ 2G_L G_R m_{\chi_i}m_{\chi_j}[(g_L^2 + g_R^2)((p_1\cdot p_2) - m_\ell^2(s_1\cdot s_2)) + (g_L^2 - g_R^2)((p_1\cdot s_2) - (p_2\cdot s_1))] +$$

$$+ (G_L^2 - G_R^2)[(g_L^2 + g_R^2)m_\ell((p_1\cdot k_2)(k_1\cdot s_2) - (p_1\cdot k_1)(k_2\cdot s_2) + (k_2\cdot p_2)(k_1\cdot s_1) - (k_1\cdot p_2)(k_2\cdot s_1)) +$$

$$+ (g_L^2 - g_R^2)((k_1\cdot p_2)(k_2\cdot p_1) - (k_1\cdot p_1)(k_2\cdot p_2) + m_\ell^2((k_1\cdot s_1)(k_2\cdot s_2) - (k_1\cdot s_2)(k_2\cdot s_1)) +$$

$$+ g_R g_L m_\ell((k_2\cdot p_2)(k_1\cdot s_2) - (k_1\cdot p_2)(k_2\cdot s_2) + (k_1\cdot p_1)(k_2\cdot s_1) - (k_2\cdot p_1)(k_1\cdot s_1))]\}, \qquad (8)$$

where m_ℓ – is the lepton mass.

Using calculations based on (8), for arbitrary polarization of the colliding lepton-antilepton beams in the center-of-mass system, we have the following expression for the differential cross section reaction (1):

$$\frac{d\sigma^{(Z)}}{d\Omega} = \frac{g^4 s|D_Z(s)|^2}{256\pi^2\cos^4\theta_W}\sqrt{\lambda(r_i,r_j)}\{[g_L^2(1-\lambda_1)(1+\lambda_2) + g_R^2(1+\lambda_1)(1-\lambda_2)]\times$$

$$\times [(G_L^2 + G_R^2)((1 + r_i - r_j)(1 - r_i + r_j) + \lambda(r_i, r_j)\cos^2\theta) + 4G_L G_R \sqrt{r_i r_j}] + g_L g_R (G_L^2 + G_R^2)\eta_1\eta_2\lambda(r_i, r_j) \times$$

$$\times \sin^2\theta\cos(2\varphi - \phi) + [g_L^2(1 - \lambda_1)(1 + \lambda_2) - g_R^2(1 + \lambda_1)(1 - \lambda_2)](G_L^2 - G_R^2)\sqrt{\lambda(r_i, r_j)}\cos\theta\}, \qquad (9)$$

here λ_1 and λ_2 – are the helicities of the lepton and antilepton, η_1 and η_2 – are the transverse components of the spin vectors of the lepton-antilepton pair, θ – the angle of departure of the neutralino $\tilde{\chi}_j^0$ with respect to the lepton momentum direction, φ – the azimuthal angle of departure of the neutralino, and ϕ – the angle between the vectors $\vec{\eta}_1$ and $\vec{\eta}_2$,

$$r_i = \left(\frac{m_{\tilde{\chi}_i^0}}{\sqrt{s}}\right)^2, \quad r_j = \left(\frac{m_{\tilde{\chi}_j^0}}{\sqrt{s}}\right)^2, \quad \lambda(r_i, r_j) \text{ – is the kin-}$$

ematic function of the two-particle phase volume:

$$\lambda(r_i, r_j) = (1 - r_i - r_j)^2 - 4r_i r_j.$$

Let us analyze the differential cross section (9) in various cases of lepton-antilepton pair polarization. It is well known that electrons and positrons moving in storage rings acquire predominantly transverse polarization due to synchrotron radiation. In the case when the lepton-antilepton pair is polarized transversely, the differential cross section of the process (1) has the form:

$$\frac{d\sigma^{(Z)}(\eta_1, \eta_2)}{d\Omega} = \frac{d\sigma_0^{(Z)}(\theta)}{d\Omega}[1 + \eta_1\eta_2 A_\perp(\theta, \varphi)]. \qquad (10)$$

Here

$$\frac{d\sigma_0^{(Z)}(\theta)}{d\Omega} = \frac{g^4 s |D_Z(s)|^2}{256\pi^2\cos^4\theta}\sqrt{\lambda(r_i, r_j)}\{(g_L^2 + g_R^2)[(G_L^2 + G_R^2)((1 + r_i - r_j)(1 - r_i + r_j) +$$

$$+ \lambda(r_i, r_j)\cos^2\theta) + 4G_L G_R \sqrt{r_i r_j}] + (g_L^2 - g_R^2)(G_L^2 - G_R^2)\sqrt{\lambda(r_i, r_j)}\cos\theta\} \qquad (11)$$

– is the differential cross section of the process averaged over the polarization states of the lepton-antilepton pair, a $A_\perp(\theta, \varphi)$ – is the azimuthal angular (or transverse spin) asymmetry determined by the formula (the angle ϕ is assumed $\phi = \pi$):

$$A_\perp(\theta, \varphi) = \frac{d\sigma(\theta, 2\varphi)/d\Omega - d\sigma(\theta, \pi - 2\varphi)/d\Omega}{d\sigma(\theta, 2\varphi)/d\Omega + d\sigma(\theta, \pi - 2\varphi)/d\Omega} = -g_L g_R (G_L^2 + G_R^2)^2\lambda(r_i, r_j)\sin^2\theta\cos 2\varphi \times$$

$$\times \{(g_L^2 + g_R^2)[(G_L^2 + G_R^2)[(1 + r_i - r_j)(1 - r_i + r_j) + \lambda(r_i, r_j)\cos^2\theta] + 4G_L G_R \sqrt{r_i r_j}] +$$

$$+ (g_L^2 - g_R^2)(G_L^2 - G_R^2)\sqrt{\lambda(r_i, r_j)}\cos\theta\}^{-1}. \qquad (12)$$

The differential cross section of the process $\ell^-\ell^+ \to (Z^*) \to \tilde{\chi}_i^0\tilde{\chi}_j^0$ in the case of nonpolarized particles (11) is not symmetric when the polar angle is replaced by $\theta \to \pi - \theta$. Hence, the angular distribution neutralino possesses asymmetry. The forward-backward angular asymmetry is defined by formula

$$A_{FB}(\theta) = \frac{d\sigma_0^{(Z)}(\theta)/d(\cos\theta) - d\sigma_0^{(Z)}(\pi - \theta)/d(\cos\theta)}{d\sigma_0^{(Z)}(\theta)/d(\cos\theta) + d\sigma_0^{(Z)}(\pi - \theta)/d(\cos\theta)} \qquad (13)$$

and has the following form

$$A_{FB}(\theta) = \frac{g_L^2 - g_R^2}{g_L^2 + g_R^2}\frac{(G_L^2 - G_R^2)\sqrt{\lambda(r_i, r_j)}\cos\theta}{(G_L^2 + G_R^2)[(1 + r_i - r_j)(1 - r_i + r_j) + \lambda(r_i, r_j)\cos^2\theta] + 4G_L G_R \sqrt{r_i r_j}}. \qquad (14)$$

Now assume that the lepton-antilepton pair, as well as the neutralino $\tilde{\chi}_i^0$ and $\tilde{\chi}_j^0$ polarized longitudinally. In this case, let us represent the differential cross section of the process (1) as follows:

$$\frac{d\sigma^{(Z)}(\lambda_1, \lambda_2; h_1, h_2)}{d\Omega} = \frac{g^4 s |D_Z(s)|^2}{1024\pi^2\cos^4\theta_W}\sqrt{\lambda(r_i, r_j)}\{[g_L^2(1 - \lambda_1)(1 + \lambda_2) + g_R^2(1 + \lambda_1)(1 - \lambda_2)] \times$$

$$\times [(G_L^2 + G_R^2)((1 + r_i - r_j)(1 - r_i + r_j) + \lambda(r_i, r_j)\cos^2\theta - h_1 h_2((1 + r_i - r_j)(1 - r_i + r_j)\cos^2\theta + \lambda(r_i, r_j))) +$$

49

$$+ (G_L^2 - G_R^2)\sqrt{\lambda(r_i, r_j)}(h_2(1 + r_i - r_j + (1 - r_i + r_j)\cos^2\theta) - h_1(1 - r_i + r_j + (1 + r_i - r_j)\cos^2\theta)) +$$

$$+ 8G_L G_R\sqrt{r_i r_j}(1 - h_1 h_2)] + [g_L^2(1 - \lambda_1)(1 + \lambda_2) - g_R^2(1 + \lambda_1)(1 - \lambda_2)] \times [(G_L^2 + G_R^2)(h_2 - h_1)((1 + r_i - r_j) \times$$

$$\times (1 - r_i + r_j) + \lambda(r_i, r_j)] + 2(G_L^2 - G_R^2)(1 - h_1 h_2)\sqrt{\lambda(r_i, r_j)} + 8G_L G_R(h_2 - h_1)\sqrt{r_i \cdot r_j}]\cos\theta\}, \qquad (15)$$

where h_1 and h_2 – are the helicities of the neutralino $\tilde{\chi}_i^0$ and $\tilde{\chi}_j^0$.

As can be seen from the cross section, the lepton and the antilepton must have opposite helicities at annihilation: $\lambda_1 = -\lambda_2 = \pm 1$. If the antilepton is polarized right $\lambda_2 = +1(\ell_R^+)$, the lepton must have a left-handed helicity $\lambda_1 = -1$ (ℓ_L^-) and vice versa, if the left-handed antilepton is annihilated ($\lambda_2 = -1; \ell_L^+$), the lepton must have a right-handed helicity: $\lambda_1 = +1$ (ℓ_R^-) (see Fig. 2, which shows the momentum and spin vectors of the lepton-antilepton pair).

This is a consequence of the conservation of total momentum in the transition $\ell^- + \ell^+ \to Z$. Indeed, consider this process in the center-of-mass system of the lepton-antilepton pair. In this system, the momenta of the lepton and antilepton are equal in magnitude and opposite in direction. In Fig. 2a), the helicity of the lepton is $\lambda_1 = -1$, and the helicity of the antilepton is $\lambda_2 = +1$. Hence, the projection of the total momentum of the lepton-antilepton pair in the direction of the antilepton momentum will be $+1$ (in units of $\hbar$); the spin of the Z-boson also equals $+1$, so the total momentum is conserved in the transition $\ell^- + \ell^+ \to Z$.

Fig. 2. Impulse and spin $\ell^- \ell^+$-pair directions.

As for the helicities of neutralinos h_1 and h_2, we note that, according to formula (15), they can be arbitrary independently of each other ($h_1 = \pm 1$, $h_2 = \pm 1$). This is due to taking into account the masses $m_{\tilde{\chi}_i^0}$ and $m_{\tilde{\chi}_j^0}$ neutralinos. Suppose that the energy

of the counter lepton-antilepton beams is much larger than the masses of the neutralinos ($\sqrt{s} >> m_{\tilde{\chi}_i^0}$, $m_{\tilde{\chi}_j^0}$), then we can neglect the mass terms of the neutralinos. As a result, for the cross section of the process (1) we have the expression:

$$\frac{d\sigma^{(Z)}(\lambda_1, \lambda_2; h_1, h_2)}{d\Omega} = \frac{g^4 s |D_Z(s)|^2}{1024 \pi^2 \cos^4\theta_W}\{[g_L^2(1 - \lambda_1)(1 + \lambda_2) + g_R^2(1 + \lambda_1)(1 - \lambda_2)] \times$$

$$\times [G_L^2(1 - h_1)(1 + h_2) + G_R^2(1 + h_1)(1 - h_2)](1 + \cos^2\theta) + [g_L^2(1 - \lambda_1)(1 + \lambda_2) - g_R^2(1 + \lambda_1)(1 - \lambda_2)] \times$$

$$\times [G_L^2(1 - h_1)(1 + h_2) - G_R^2(1 + h_1)(1 - h_2)] \cdot 2\cos\theta\} . \qquad (16)$$

According to this formula, the neutralinos $\tilde{\chi}_i^0$ and $\tilde{\chi}_j^0$ must have opposite helicities $h_1 = -h_2 = \pm 1$. At high energies, the process $\ell^- + \ell^+ \to \tilde{\chi}_i^0 + \tilde{\chi}_j^0$ corresponds to four spiral cross sections:

$$\frac{d\sigma_{LL}^{(Z)}}{d\Omega} \sim [g_L G_L(1 + \cos\theta)]^2,$$

$$\frac{d\sigma_{LR}^{(Z)}}{d\Omega} \sim [g_L G_R(1 - \cos\theta)]^2,$$

$$\frac{d\sigma_{RR}^{(Z)}}{d\Omega} \sim [g_R G_R(1 + \cos\theta)]^2,$$

$$\frac{d\sigma_{RL}^{(Z)}}{d\Omega} \sim [g_R G_L(1 - \cos\theta)]^2. \qquad (17)$$

Here, the first and second indices at the cross section show the helicities of the lepton and neutralino $\tilde{\chi}_i^0$, respectively. For example, $\frac{d\sigma_{LL}^{(Z)}}{d\Omega}$ defines the cross section of the spiral process $\ell_L^- + \ell_R^+ \to \tilde{\chi}_{iL}^0 + \tilde{\chi}_{jR}^0$.

As can be seen from the expression of the spiral sections (17), the sections $\frac{d\sigma_{LL}^{(Z)}}{d\Omega}$ and $\frac{d\sigma_{RR}^{(Z)}}{d\Omega}$ are zero at $\theta = \pi$, and the sections $\frac{d\sigma_{LR}^{(Z)}}{d\Omega}$ and $\frac{d\sigma_{RL}^{(Z)}}{d\Omega}$ are zero at $\theta = 0$. This is a consequence of the law of conservation of total momentum (see Fig. 3, where the directions of momenta and spins of initial and final particles are represented).
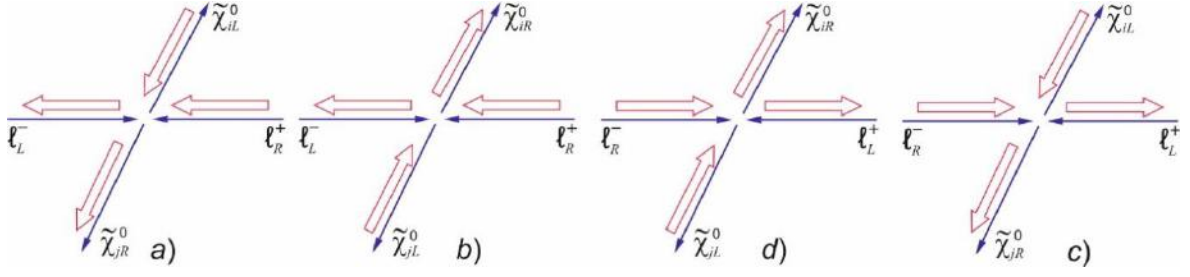
Fig. 3. Directions of impulses and spins of particles in the process $\ell^-\ell^+ \to \tilde{\chi}_i^0\tilde{\chi}_j^0$.

Fig. 4. Directions of impulses and spins of the particles at $\theta = \pi$.

Let us consider a spiral process $\ell_L^- + \ell_R^+ \to \tilde{\chi}_{iL}^0 + \tilde{\chi}_{jR}^0$ in the center-of-mass system at $\theta = \pi$. In this case the neutralino $\tilde{\chi}_i^0$ flies out against the momentum of the electron (Fig. 4).

The projection of the total momentum of the initial particles on the direction of the lepton momentum is -1. However, the projection of the total momentum of finite particles on the direction of the lepton momentum is equal $+1$ (see Fig. 4b). Thus, the law of conservation of the total momentum is not satisfied.

Therefore, the departure of the neutralino $\tilde{\chi}_i^0$ against the lepton momentum is forbidden by the law of conservation of the total momentum. The multiplier $(1+\cos\theta)^2$ in the expression for the corresponding cross section corresponds to this.

Based on the differential effective cross section (15), let us determine the longitudinal spin asymmetry due to lepton (antilepton) polarization:

$$A_1(\theta) = \frac{1}{\lambda_1}\frac{d\sigma^{(Z)}(\lambda_1,0)\big/d\Omega - d\sigma^{(Z)}(-\lambda_1,0)\big/d\Omega}{d\sigma^{(Z)}(\lambda_1,0)\big/d\Omega + d\sigma^{(Z)}(-\lambda_1,0)\big/d\Omega},$$

$$A_2(\theta) = \frac{1}{\lambda_2}\frac{d\sigma^{(Z)}(0,\lambda_2)\big/d\Omega - d\sigma^{(Z)}(0,-\lambda_2)\big/d\Omega}{d\sigma^{(Z)}(0,\lambda_2)\big/d\Omega + d\sigma^{(Z)}(0,-\lambda_2)\big/d\Omega}, \tag{18}$$

where $\dfrac{d\sigma^{(Z)}(\lambda_1,0)}{d\Omega}\left(\dfrac{d\sigma^{(Z)}(0,\lambda_2)}{d\Omega}\right)$ – is the differential cross section of the process (1) in the annihilation of

the longitudinally polarized lepton and nonpolarized antilepton (nonpolarized lepton and longitudinally polarized antilepton). Given (15) in (18), we have

$$A_2(\theta) = -A_1(\theta) = \{(g_L^2 - g_R^2)[(G_L^2 + G_R^2)[(1+r_i-r_j)(1-r_i+r_j)+\lambda(r_i, r_j)\cos^2\theta] + 4G_LG_R\sqrt{r_{\chi_i}r_{\chi_j}}] +$$
$$+ (g_L^2 - g_R^2)(G_L^2 - G_R^2)\sqrt{\lambda(r_i,\, r_j)}\cos\theta\} \times \{(g_L^2 + g_R^2)[(G_L^2 + G_R^2)[(1+r_i-r_j)(1-r_i+r_j)+$$
$$+ \lambda(r_i,\, r_j)\cos^2\theta] + 4G_LG_R\sqrt{r_{\chi_i}r_{\chi_j}}] + (g_L^2 - g_R^2)(G_L^2 - G_R^2)\sqrt{\lambda(r_i,\, r_j)}\cos\theta\}^{-1}. \tag{19}$$

Hence, the longitudinal spin asymmetry $A_1(\theta)$, resulting from the annihilation of a polarized lepton with an nonpolarized antilepton, is equal in magnitude but opposite in sign to the longitudinal spin asymmetry $A_2(\theta)$, resulting from the annihilation of an nonpolarized lepton with a polarized antilepton.

Measurement of the transverse spin asymmetry $A_\perp(\theta,\varphi)$, the angular forward-backward asymmetry $A_{FB}(\theta)$, the longitudinal spin asymmetries $A_1(\theta)$ and $A_2(\theta)$ in the experiment allows, in principle, to

obtain information about constants of the neutralino with the vector Z-boson G_L and G_R.

From the formula of the differential cross section (9), we can obtain expressions for the integral characteristics of the process $\ell^- + \ell^+ \to \tilde{\chi}_i^0 + \tilde{\chi}_j^0$. For this purpose, let us define the following expressions for the cross sections for the production of a neutralino pair:

a) in the case of a transversely polarized lepton-antilepton pair

$$\frac{d\sigma^{(Z)}(\eta_1,\eta_2)}{d\varphi} = \int\limits_0^\pi \frac{d\sigma}{d\Omega}d(\cos\theta) = \frac{g^4 s|D_Z(s)|^2}{128\pi^2\cos^4\theta_W}\sqrt{\lambda(r_i,\,r_j)} \times$$

$$\times\left\{(g_L^2+g_R^2)\left[(G_L^2+G_R^2)\left((1+r_i-r_j)(1-r_i+r_j)+\frac{1}{3}\lambda(r_i,\,r_j)\right)+4G_LG_R\sqrt{r_ir_j}\right] - \right.$$

$$\left. -\frac{2}{3}g_Lg_R(G_L^2+G_R^2)\eta_1\eta_2\lambda(r_i,\,r_j)\cos2\varphi\right\}; \tag{20}$$

b) in the case of longitudinally polarized $\ell^-\ell^+$ -pair

$$\sigma^{(Z)}(\lambda_1,\lambda_2) = 2\pi\int\limits_0^\pi \frac{d\sigma(\lambda_1,\lambda_2)}{d(\cos\theta)}d(\cos\theta) =$$

$$= \frac{g^4 s|D_Z(s)|^2}{64\pi\cos^4\theta_W}\sqrt{\lambda(r_i,\,r_j)}[g_L^2(1-\lambda_1)(1+\lambda_2)+g_R^2(1+\lambda_1)(1-\lambda_2)] \times$$

$$\times\left\{(G_L^2+G_R^2)\left[(1+r_i-r_j)(1-r_i+r_j)+\frac{1}{3}\lambda(r_i,\,r_j)\right]+4G_LG_R\sqrt{r_ir_j}\right\}. \tag{21}$$

Let us also determine the cross sections for the neutralino production in the front (F) and back (B) hemispheres in the case of nonpolarized particles:

$$\sigma_F^{(Z)} = 2\pi\int\limits_0^{\pi/2} \frac{d\sigma_0(\theta)}{d(\cos\theta)}d(\cos\theta) = \frac{g^4 s|D_Z(s)|^2}{128\pi\cos^4\theta_W}\sqrt{\lambda(r_i,\,r_j)} \times$$

$$\times\left\{(g_L^2+g_R^2)\left[(G_L^2+G_R^2)\left((1+r_i-r_j)(1-r_i+r_j)+\frac{1}{3}\lambda(r_i,\,r_j)\right)+4G_LG_R\sqrt{r_ir_j}\right] + \right.$$

$$\left. +(g_L^2-g_R^2)(G_L^2-G_R^2)\sqrt{\lambda(r_i,\,r_j)}\cdot\frac{1}{2}\right\}, \tag{22}$$

$$\sigma_B^{(Z)} = 2\pi\int\limits_{\pi/2}^\pi \frac{d\sigma_0(\theta)}{d(\cos\theta)}d(\cos\theta) = \frac{g^4 s|D_Z(s)|^2}{128\pi\cos^4\theta_W}\sqrt{\lambda(r_i,\,r_j)} \times$$

$$\times\left\{(g_L^2+g_R^2)\left[(G_L^2+G_R^2)\left((1+r_i-r_j)(1-r_i+r_j)+\frac{1}{3}\lambda(r_i,\,r_j)\right)+4G_LG_R\sqrt{r_ir_j}\right] - \right.$$

$$\left. +(g_L^2-g_R^2)(G_L^2-G_R^2)\sqrt{\lambda(r_i,\,r_j)}\cdot\frac{1}{2}\right\}, \tag{23}$$

From formula (20) of the cross section we define the transverse spin asymmetry $A_\perp(\sqrt{s},\varphi)$, integrated on the polar angle of the neutralino θ:

$$A_\perp(\sqrt{s},\varphi) = -\frac{2g_Lg_R}{g_L^2+g_R^2}\frac{(G_L^2+G_R^2)\lambda(r_i,\,r_j)\cos2\varphi}{(G_L^2+G_R^2)[3(1+r_i-r_j)(1-r_i+r_j)+\lambda(r_i,\,r_j)]+12G_LG_R\sqrt{r_ir_j}}. \tag{24}$$

From the cross section formula (15) for the integral longitudinal spin asymmetry we obtain:

$$A_2 = -A_1 = \frac{g_L^2-g_R^2}{g_L^2+g_R^2}. \tag{25}$$

These longitudinal spin asymmetries depend only on the Weinberg parameter $x_W = \sin^2\theta_W$ and at $x_W = 0.2315$ $A_2 = -A_1 = 14.7\%$.

For the integral forward-backward asymmetry, we obtain the expression:

$$A_{FB}(\theta) = \frac{\sigma_F - \sigma_B}{\sigma_F + \sigma_B} =$$

$$= \frac{g_L^2 - g_R^2}{g_L^2 + g_R^2} \frac{(G_L^2 - G_R^2)\sqrt{\lambda(r_i, r_j)}}{(G_L^2 + G_R^2)[(1 + r_i - r_j)(1 - r_i + r_j) + \frac{1}{3}\lambda(r_i, r_j) + 8G_L G_R \sqrt{r_i r_j}}. \tag{26}$$

Let us estimate the above asymmetries in the processes $e^- + e^+ \to \tilde{\chi}_1^0 + \tilde{\chi}_2^0$ and $e^- + e^+ \to \tilde{\chi}_2^0 + \tilde{\chi}_2^0$. For the left and right coupling constants of the neutralino with the Z-boson we obtain expressions:

1) in the process $e^- + e^+ \to \tilde{\chi}_1^0 + \tilde{\chi}_2^0$:

$$G_R = -G_L = \frac{1}{2\sin\theta_W}[Z_{13}Z_{23} - Z_{14}Z_{24}];$$

2) in the process $e^- + e^+ \to \tilde{\chi}_2^0 + \tilde{\chi}_2^0$:

$$G_R = -G_L = \frac{1}{2\sin\theta_W}[(Z_{23})^2 - (Z_{24})^2],$$

the matrix elements of the and matrix Z_{13}, Z_{23}, Z_{14} and Z_{24} are given in [11, 13].

Fig. 5 shows the angular dependence of the transverse spin asymmetry $A_\perp(\theta)$ in the reactions $e^- + e^+ \to \tilde{\chi}_1^0 + \tilde{\chi}_2^0$ (curve 1), $e^- + e^+ \to \tilde{\chi}_2^0 + \tilde{\chi}_2^0$ (curve 2) at $\varphi = 0$, $\sqrt{s} = 500$ GeV, $M_2 = 2M_1 = 150$ GeV, $\text{tg}\beta = 3$, $x_W = 0.2315$.
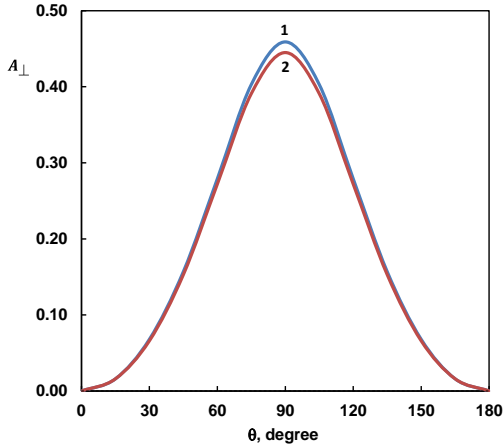

Fig. 5. Dependence of the transverse spin asymmetry $A_\perp$ on θ

Fig. 6 illustrates the energy dependence of the transverse spin asymmetry integrated along the polar angle θ in the reactions $e^- + e^+ \to \tilde{\chi}_1^0 + \tilde{\chi}_2^0$ (curve 1), $e^- + e^+ \to \tilde{\chi}_2^0 + \tilde{\chi}_2^0$ (curve 2) at the same values of the parameters as in Fig. 5.

As for the forward-backward angular asymmetry $A_{FB}(\theta)$, as well as the forward-backward integral asymmetry A_{FB}, we note that, due to the relation

between the neutralino $G_L = -G_R$ bond chiral constants in the reactions considered, they turn to zero $A_{FB}(\theta) = A_{FB} = 0$. For this reason, the longitudinal spin asymmetries $A_2(\theta) = -A_1(\theta)$ do not depend on the angle of departure of the neutralino and are only functions of the left and right coupling constants of the lepton with the gauge Z-boson:

$$A_2(\theta) = -A_1(\theta) = \frac{g_L^2 - g_R^2}{g_L^2 + g_R^2}.$$

The energy dependence of the reaction $e^- + e^+ \to \tilde{\chi}_1^0 + \tilde{\chi}_2^0$ cross section is presented in Fig. 7 in three cases: 1) when the electron is polarized right: $\lambda_1 = +1$; 2) when the electron possesses left-hand helicity: $\lambda_1 = -1$; 3) when the electron is non-polarized.
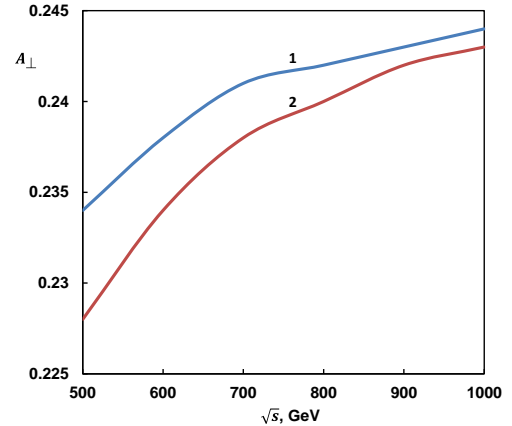

Fig. 6. Dependence of transverse spin asymmetry $A_\perp$ on energy $\sqrt{s}$.

3. DEGREES OF LONGITUDINAL AND TRANSVERSE POLARIZATION OF THE NEUTRALINO

In the previous section we were interested in the polarization properties of the lepton and antilepton, we determined the transverse and longitudinal spin asymmetries due to the lepton and antilepton polarizations. Note that the study of the degrees of longitudinal and transverse polarizations of the neutralino is also of some interest. They can give valuable information about the interaction constants of the neutralino with the gauge Z-boson G_L and G_R. In this connection, let us proceed to the study of the polarization characteristics of the neutralino.
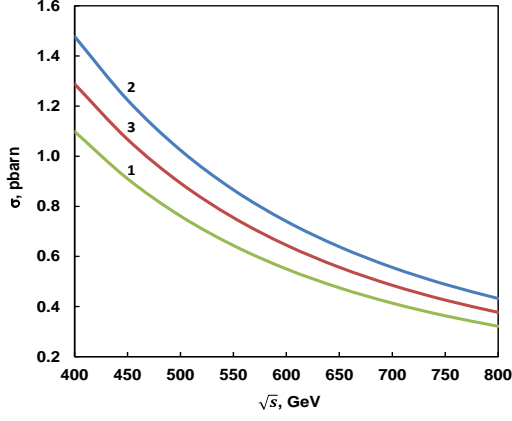
Fig. 7. Dependence of the reaction $e^- + e^+ \rightarrow \tilde{\chi}_1^0 + \tilde{\chi}_2^0$ cross section on the energy $\sqrt{s}$ at $\lambda_1 = +1$ (curve 1), at $\lambda_1 = -1$ (curve 2) and nonpolarized lepton ($\lambda_1 = 0$) (curve 3).

Let us consider the differential section of the process (1) taking into account the longitudinal polarizations of the lepton and neutralino:

$$\frac{d\sigma^{(Z)}(\lambda_1, h)}{d\Omega} = \frac{1}{2} \frac{d\sigma_0^{(Z)}(\lambda_1)}{d\Omega}[1 + h_1 P_\parallel(\sqrt{s}, \theta)], \quad (27)$$

$\dfrac{d\sigma_0^{(Z)}(\lambda_1)}{d\Omega}$ – is the differential cross section of reaction (1) in the annihilation of a polarized lepton and an nonpolarized antilepton:

$$\frac{d\sigma_0^{(Z)}(\lambda_1)}{d\Omega} = \frac{g^4 s |D_Z(s)|^2}{256 \pi^2 \cos^4 \theta_W} \sqrt{\lambda(r_i, r_j)} \{[g_L^2(1 - \lambda_1) + g_R^2(1 + \lambda_1)] \times$$
$$\times [(G_L^2 + G_R^2)((1 + r_i - r_j)(1 - r_i + r_j) + \lambda(r_i, r_j)\cos^2\theta) + 4 G_L G_R \sqrt{r_i r_j}] +$$
$$+ [g_L^2(1 - \lambda_1) - g_R^2(1 + \lambda_1)](G_L^2 - G_R^2)\sqrt{\lambda(r_i, r_j)}\cos\theta, \quad (28)$$

a $P_\parallel(\sqrt{s}, \theta)$ – is the degree of longitudinal polarization of the neutralino:

$$P_\parallel(\sqrt{s}, \theta) = \{[g_L^2(1 - \lambda_1) + g_R^2(1 + \lambda_1)](G_R^2 - G_L^2)\sqrt{\lambda(r_i, r_j)}[1 - r_i + r_j + (1 + r_i - r_j)\cos^2\theta -$$
$$- 2[g_L^2(1 - \lambda_1) - g_R^2(1 + \lambda_1)][(G_L^2 + G_R^2)(1 - r_i - r_j) + 4 G_L G_R \sqrt{r_i r_j}\cos\theta\} \times$$
$$\times \{[g_L^2(1 - \lambda_1) + g_R^2(1 + \lambda_1)](G_L^2 + G_R^2)((1 + r_i - r_j)(1 - r_i + r_j) + \lambda(r_i, r_j)\cos^2\theta) + 8 G_L G_R \sqrt{r_i r_j}] +$$
$$+ 2[g_L^2(1 - \lambda_1) - g_R^2(1 + \lambda_1)](G_L^2 - G_R^2)\sqrt{\lambda(r_i, r_j)}\}^{-1}. \quad (29)$$

If the neutralino is polarized transversely in the plane of production, then the differential cross section of the reaction $e^- + e^+ \rightarrow \tilde{\chi}_i^0 + \tilde{\chi}_j^0$ will take the form (the lepton is polarized longitudinally):

$$\frac{d\sigma^{(Z)}(\lambda_1, \eta)}{d\Omega} = \frac{1}{2} \frac{d\sigma_0^{(Z)}(\lambda_1)}{d\Omega}[1 + \eta P_\perp(\sqrt{s}, \theta)], \quad (30)$$

where η – is the transverse component of the neutralino spin vector, $\dfrac{d\sigma_0^{(Z)}(\lambda_1)}{d\Omega}$ – is the differential cross section for the annihilation of a longitudinally polarized lepton and an nonpolarized antilepton (formula (28)), and $P_\perp(\sqrt{s}, \theta)$ – the degree of transverse polarization of the neutralino is defined by the expression:

$$P_\perp(\sqrt{s}, \theta) = \sqrt{\lambda(r_i, r_j)} \sin 2\theta \{[g_L^2(1 - \lambda_1) + g_R^2(1 + \lambda_1)](G_L^2 - G_R^2)\sqrt{r_j} +$$
$$+ [g_L^2(1 - \lambda_1) - g_R^2(1 + \lambda_1)][-(G_L^2 + G_R^2)\sqrt{r_i} + 8 G_L G_R \sqrt{r_j}]\} \cdot \{[g_L^2(1 - \lambda_1) + g_R^2(1 + \lambda_1)] \times$$
$$\times [(G_L^2 + G_R^2)[(1 + r_i - r_j)(1 - r_i + r_j) + \lambda(r_i, r_j)\cos^2\theta] + 8 G_L G_R \sqrt{r_i r_j}] +$$
$$+ 2[g_L^2(1 - \lambda_1) - g_R^2(1 + \lambda_1)](G_L^2 - G_R^2)\sqrt{\lambda(r_i, r_j)}\cos\theta\}^{-1}. (31)$$

Figure 8 illustrates the dependence of the degree of longitudinal polarization of the neutralino in the process $e^- + e^+ \rightarrow \tilde{\chi}_1^0 + \tilde{\chi}_2^0$ on the angle θ at $\sqrt{s} = $ 500 GeV and $\lambda_1 = +1$ (curve 1), $\lambda_1 = -1$ (curve 2) and at nonpolarized electron (curve 3). It follows from the figure that at $\lambda_1 = +1$ ($\lambda_1 = -1$) the degree of longitudinal polarization of the neutralino is minimal (maximum), with an increase in the angle θ it in-

creases (decreases) and vanishes at an angle of θ =90°. With a further increase in the angle θ, the degree of longitudinal polarization of the neutralino changes sign and increases (decreases).
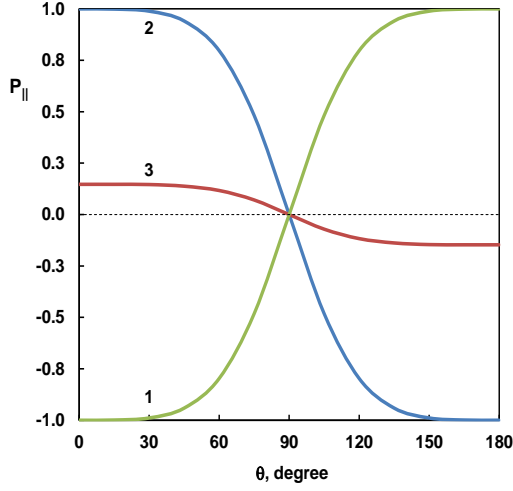

Fig. 8. Degree of longitudinal polarization of the neutralino in the reaction $e^-e^+ \to \tilde{\chi}_1^0 \tilde{\chi}_2^0$ as a function of the polar angle θ at $\lambda_1 = +1$ (curve 1), $\lambda_1 = -1$ (curve 2), at nonpolarized e^-e^+-pair (curve 3).
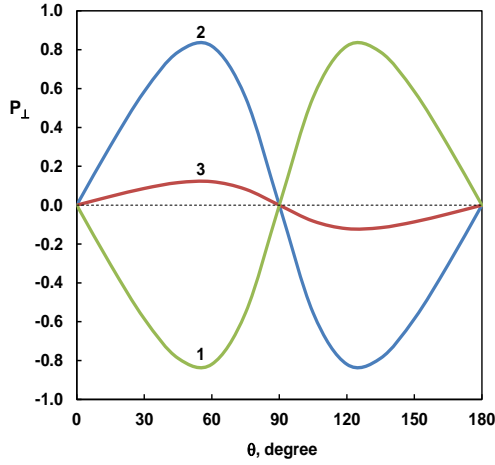

Fig. 9. Dependence of the transverse spin asymmetry $P_\perp(\sqrt{s}, \theta)$ on the angle θ in the reaction $e^-e^+ \to \tilde{\chi}_2^0 \tilde{\chi}_2^0$.

In the case of nonpolarized initial particles, the degree of longitudinal polarization of neutralino at the beginning of the angular spectrum is positive and gradually decreases with increasing angle.

The angular dependence of the degree of transverse polarization of the neutralino $P_\perp(\sqrt{s}, \theta)$ in the process $e^- + e^+ \to \tilde{\chi}_2^0 + \tilde{\chi}_2^0$ is shown in Fig. 9 for $\lambda_1 = +1$ (curve 1), $\lambda_1 = -1$ (curve 2) and at nonpolarized electron (curve 3). As you can see, the degree of transverse polarization is maximum or minimum near the angle 60° or 150°, vanishes at $\theta = 0°$; 90° and 180°.

4. AMPLITUDE AND CROSS SECTION OF THE PROCESS $\ell^- \ell^+ \to (\Phi^*) \to \tilde{\chi}_2^0 \tilde{\chi}_2^0$

We now turn to the study of the effective cross section of the process corresponding to the diagram b) of Fig. 1 with the Higgs boson exchange $\Phi^* = H^*(h^*; A^*)$. The Lagrangians of the interaction of the Higgs boson Φ with a lepton pair and a neutralino pair are written in the following form [7, 20]:

$$L_{\Phi\ell\ell} = -g_{\Phi\ell\ell}\,\overline{\ell}\gamma_\mu(a+b\gamma_5)\ell \cdot \Phi,$$
$$L_{\Phi\chi_i^0\chi_j^0} = g \cdot \overline{\tilde{\chi}}_i^0 \gamma_\mu (G_L P_L + G_R P_R)\tilde{\chi}_j^0 \cdot \Phi, \tag{32}$$

where in the case of CP-even Higgs bosons H and h $a = 1$ and $b = 0$ and

$$g_{H\ell\ell} = i\frac{m_\ell}{\upsilon}\cdot\frac{\cos\alpha}{\cos\beta}, \quad g_{h\ell\ell} = -i\frac{m_\ell}{\upsilon}\cdot\frac{\sin\alpha}{\cos\beta},$$

and in the case of CP-odd A-bosons $a = 0$ and $b = 1$ and

$$a = \frac{m_\ell}{\upsilon}\mathrm{tg}\beta,$$

$\upsilon = 246$ GeV is the vacuum value of the Higgs boson field, G_L and G_R – are the left and right interaction constants of the Higgs boson with the neutralino pair

$$G_L = \frac{1}{2\sin\theta_W}(Z_{j2} - \mathrm{tg}\theta_W Z_{j1})(e_k Z_{i3} + d_k Z_{i4}) + i \leftrightarrow j,$$

$$G_R = \frac{1}{2\sin\theta_W}(Z_{j2} - \mathrm{tg}\theta_W Z_{j1})(e_k Z_{i3} + d_k Z_{i4})\varepsilon_k + i \leftrightarrow j, \tag{33}$$

$\varepsilon_1 = \varepsilon_2 = -\varepsilon_3 = 1$, the coefficients of e_k and d_k are equal:

$$e_1 = +\cos\alpha, \quad e_2 = -\sin\alpha, \quad e_3 = -\sin\beta,$$
$$d_1 = -\sin\alpha, \quad d_2 = -\cos\alpha, \quad d_3 = +\cos\beta.$$

Based on the Lagrangians (32), let us write down the amplitude of the corresponding diagram b) of Fig. 1:

$$M_{i \to f}^{(\Phi)} = g_{\Phi \ell \ell} g D_\Phi(s) \overline{\upsilon}_\ell(p_2, s_2)(a + b\gamma_5) u_\ell(p_1, s_1) g[\overline{u}_i(k_1, s)(G_L P_L + G_R P_R)\upsilon_j(k_2, s')]. \quad (34)$$

Here $D_\Phi(s) = (s - M_\Phi^2 + i\Gamma_\Phi M_\Phi)^{-1}$, M_Φ and Γ_Φ – are the mass and total width of the Φ-boson.

The square of the modulus of the matrix element (34) with simultaneous accounting of the polarizations of all particles involved has the form:

$$\left| M_{i \to f}^{(\Phi)} \right|^2 = g_{\Phi \ell \ell} g^2 \left| D_\Phi(s) \right|^2 L \times \chi, \quad (35)$$

where L and χ – are the scalars functions of the lepton-antilepton pair and the neutralino pair:

$$L = [|a|^2 + |b|^2][(p_1 \cdot p_2) + m_\ell^2(s_1 \cdot s_2)] + [|a|^2 - |b|^2][-m_\ell^2 - (s_1 \cdot s_2)(p_1 \cdot p_2) + (p_1 \cdot s_2)(p_2 \cdot s_1)] -$$
$$- 2\operatorname{Re}(ab^*)m_\ell[(p_1 \cdot s_2) + (p_2 \cdot s_1)] + 2\operatorname{Im}(ab^*)(p_1 p_2 s_1 s_2)_\varepsilon\}; \quad (36)$$

$$\chi = \frac{1}{2}(G_L^2 + G_R^2)[(k_1 \cdot k_2) + m_{\chi_1} m_{\chi_2}(s \cdot s')] + \frac{1}{2}(G_L^2 - G_R^2)[m_{\chi_i}(k_2 \cdot s) + m_{\chi_j}(k_1 \cdot s')] +$$
$$+ G_L G_R[-m_{\chi_i} m_{\chi_j} - (k_1 \cdot k_2)(s \cdot s') + (k_1 \cdot s')(k_2 \cdot s)]. \quad (37)$$

The effective cross section of the process in the case of arbitrary polarizations of the initial and longitudinal polarizations of the final particles can be represented as (in the center-of-mass system):

$$\sigma^{(\Phi)} = \frac{g_{\Phi \ell \ell}^2 g^2 s}{128} \left| D_\Phi(s) \right|^2 \sqrt{\lambda(r_i, r_j)} \cdot \{[|a|^2 + |b|^2][1 - (\vec{n}\vec{\xi}_1)(\vec{n}\vec{\xi}_2)] + [|a|^2 - |b|^2] \times$$
$$\times [(\vec{\xi}_1 \vec{\xi}_2) - (\vec{n}\vec{\xi}_1)(\vec{n}\vec{\xi}_2)] + 2\operatorname{Re}(ab^*)[(\vec{n}\vec{\xi}_2) - (\vec{n}\vec{\xi}_1)] - 2\operatorname{Im}(ab^*)(\vec{n}[\vec{\xi}_1 \vec{\xi}_2])\}\{[(G_L^2 + G_R^2) \times$$
$$\times (1 - r_i - r_j) - 4G_L G_R \sqrt{r_i \cdot r_j}](1 + h_1 h_2) + (G_L^2 - G_R^2)\sqrt{\lambda(r_i, r_j)}(h_1 + h_2)\}, \quad (38)$$

where $\vec{n}$ – a unit vector in the lepton momentum direction; $\vec{\xi}_1$ and $\vec{\xi}_2$ – unit vectors directed along the lepton and antilepton spins in their rest systems, respectively.

The interaction constant of the Φ-boson with a lepton pair is proportional to the lepton mass m_ℓ, therefore the study of the process of production of the neutralino pair in muon-antimuon collisions is of particular interest. Therefore, let us consider the process $\mu^- + \mu^+ \to (\Phi^*) \to \tilde{\chi}_i^0 + \tilde{\chi}_j^0$ in the case of a longitudinally polarized muon-antimuon pair: in which $(\vec{n}\vec{\xi}_1) = \lambda_1$, $(\vec{n}\vec{\xi}_2) = -\lambda_2$, $(\vec{\xi}_1\vec{\xi}_2) = -\lambda_1\lambda_2$, where λ_1 and λ_2 – are the helicities of the muon and antimuon:

$$\sigma^{(\Phi)}(\lambda_1, \lambda_2, h_1, h_2) = \frac{g_{\Phi \ell \ell}^2 g^2 s}{128} \sqrt{\lambda(r_i, r_j)} \cdot \{[|a|^2 + |b|^2](1 + \lambda_1\lambda_2) - 2\operatorname{Re}(ab^*)(\lambda_1 + \lambda_2)\} \times$$
$$\times \{[(G_L^2 + G_R^2)(1 - r_i - r_j) - 4G_L G_R \sqrt{r_i, r_j}](1 + h_1 h_2) + (G_L^2 - G_R^2)\sqrt{\lambda(r_i, r_j)}(h_1 + h_2)\}. \quad (39)$$

It follows from this formula for the effective cross section that the muon and antimuon as well as the neutralino $\tilde{\chi}_i^0$ and $\tilde{\chi}_j^0$ must have the same helicities: $\lambda_1 = \lambda_2 = \pm 1$, $h_1 = h_2 = \pm 1$. This is a consequence of the conservation of the total angular momentum in the transitions $\ell^- + \ell^+ \to \Phi$ and $\Phi \to \tilde{\chi}_i^0 + \tilde{\chi}_j^0$. Diagram b) of Fig. 1 corresponds to four spiral sections:

1) all particles are left-polarized: ($\lambda_1 = \lambda_2 = h_1 = h_2 = -1$):

$$\sigma_{LL}^{(\Phi)} \sim |a + b|^2 \{(G_L^2 + G_R^2)(1 - r_i - r_j) - 4G_L G_R \sqrt{r_i r_j} - (G_L^2 - G_R^2)\sqrt{\lambda(r_i, r_j)}\},$$

2) all particles are right-handedly polarized: ($\lambda_1 = \lambda_2 = h_1 = h_2 = +1$):

$$\sigma_{RR}^{(\Phi)} \sim |a - b|^2 \{(G_L^2 + G_R^2)(1 - r_i - r_j) - 4G_L G_R \sqrt{r_i r_j} + (G_L^2 - G_R^2)\sqrt{\lambda(r_i, r_j)}\};$$

3) initial particles are left-polarized and final particles are right-polarized: ($\lambda_1 = \lambda_2 = -1$, $h_1 = h_2 = +1$):

$$\sigma_{LR}^{(\Phi)} \sim |a + b|^2 \{(G_L^2 + G_R^2)(1 - r_i - r_j) - 4G_L G_R \sqrt{r_i r_j} - (G_L^2 - G_R^2)\sqrt{\lambda(r_i, r_j)}\};$$

4) initial particles are right-polarized and final particles are left-polarized ($\lambda_1 = \lambda_2 = +1$, $h_1 = h_2 = -1$):

$$\sigma_{RL}^{(\Phi)} \sim |a - b|^2 \{(G_L^2 + G_R^2)(1 - r_i - r_j) - 4G_L G_R \sqrt{r_i r_j} - (G_L^2 - G_R^2)\sqrt{\lambda(r_i, r_j)}\}$$

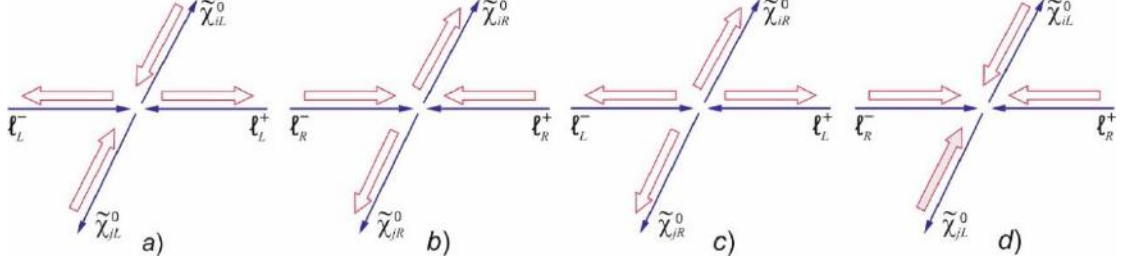In these cases directions of impulses and spins of particles are shown in Fig. 10.

Fig. 10. Directions of impulses and spins of particles in the process $\ell^- \ell^+ \to (\Phi^*) \to \tilde\chi_i^0 \tilde\chi_j^0$.

As can be seen from Fig. 10, the directions of spins of the lepton and antilepton, as well as neutralino $\tilde\chi_i^0$ and $\tilde\chi_j^0$ are directed opposite to each other, therefore, their total momentum is zero, the spin of the intermediate Higgs boson Φ is also zero, so in transitions $\ell^- + \ell^+ \to \Phi$ and $\Phi \to \tilde\chi_i^0 + \tilde\chi_j^0$ the law of conservation of total momentum is satisfied.

It follows from the above reasoning that we can distinguish contributions to the cross section of diagrams a) and b) in Fig. 1 from the spirals of the lepton-antilepton pair. The contribution of the diagram with vector Z-boson exchange differs from zero if the lepton and antilepton have opposite helicities $\lambda_1 = -\lambda_2 = \pm 1$. However, the contribution of the Φ-boson exchange diagram is zero in this case. If the lepton and the antilepton have the same helicity $\lambda_1 = \lambda_2 = \pm 1$, then the contribution of diagram a) is zero, and the contribution of diagram b) is different from zero.

On the basis of the effective cross section formula (39), let us determine the longitudinal spin asymmetries due to the polarizations of the lepton and antilepton:

$$A_1 = \frac{1}{\lambda_1} \frac{\sigma^{(\Phi)}(\lambda_1, 0) - \sigma^{(\Phi)}(-\lambda_1, 0)}{\sigma(\lambda_1, 0) + \sigma(-\lambda_1, 0)} = -\frac{2\,\mathrm{Re}(ab^*)}{|a|^2 + |b|^2},$$

$$A_2 = \frac{1}{\lambda_2} \frac{\sigma^{(\Phi)}(0, \lambda_2) - \sigma^{(\Phi)}(0, -\lambda_2)}{\sigma^{(\Phi)}(0, \lambda_2) + \sigma^{(\Phi)}(0, -\lambda_2)} = -\frac{2\,\mathrm{Re}(ab^*)}{|a|^2 + |b|^2},$$

$$(40)$$

here $\sigma^{(\Phi)}(\lambda_1, 0)$ $(\sigma^{(\Phi)}(0, \lambda_2))$ – is the annihilation cross section of the polarized lepton and nonpolarized antilepton (nonpolarized lepton and polarized antilepton). From formulas (40) it follows that the longitudinal spin asymmetry arising from the interaction of a polarized lepton with nonpolarized antileptons is equal to the longitudinal spin asymmetry arising from the interaction of polarized antileptons with nonpolarized leptons.

Experimental study of these asymmetries

$$A_1 = A_2 = -\frac{2\,\mathrm{Re}(ab^*)}{|a|^2 + |b|^2}$$

in the process $\mu^- + \mu^+ \to (\Phi^*) \to \tilde\chi_i^0 + \tilde\chi_j^0$ can provide valuable information about the nature of the Φ-boson. If the Φ-boson is a purely CP-even particle (like the $H(h)$ Higgs boson) or a CP odd particle (like the A-boson), the experiments will not reveal longitudinal spin asymmetry.

In the case where the lepton-antilepton pair is polarized transversely, the effective cross section (38) will take the form:

$$\sigma^{(\Phi)} = \frac{g_{\Phi\ell\ell}^2 g^2 s}{32} |D_\Phi(s)|^2 \sqrt{\lambda(r_i, r_j)} \cdot [|a|^2 + |b|^2 + (|a|^2 - |b|^2)\eta_1\eta_2 \cos\phi - 2\,\mathrm{Im}(ab^*)\eta_1\eta_2 \sin\phi] \times$$

$$\times [(G_L^2 + G_R^2)(1 - r_i - r_j) - 4 G_L G_R \sqrt{r_i \cdot r_j}],$$

$$(41)$$

where $\phi-$ the angle between the transverse spin vectors $\vec\eta_1$ and $\vec\eta_2$. This section leads to the following transverse spin asymmetries due to the lepton-antilepton pair polarizations:

$$A_3 = \frac{1}{\eta_1\eta_2} \frac{\sigma^{(\Phi)}(\phi = 0) - \sigma^{(\Phi)}(\phi = \pi)}{\sigma^{(\Phi)}(\phi = 0) + \sigma^{(\Phi)}(\phi = \pi)} = \frac{|a|^2 - |b|^2}{|a|^2 + |b|^2},$$

$$(42)$$

$$A_4 = \frac{1}{\eta_1 \eta_2} \frac{\sigma^{(\Phi)}(\phi = -\pi/2) - \sigma^{(\Phi)}(\phi = \pi/2)}{\sigma^{(\Phi)}(\phi = -\pi/2) + \sigma^{(\Phi)}(\phi = \pi/2)} = \frac{2\,\mathrm{Im}(ab^*)}{|a|^2 + |b|^2}. \tag{43}$$

The study of these transverse spin asymmetries is also a source of information about the nature of the Φ-boson. If the Φ-boson is CP-even then the asymmetry is $A_3 = +1$, and if it is CP-odd then this asymmetry is $A_3 = -1$. The difference from zero of the transverse spin asymmetry A_4 also indicates a violation of the CP-accountability in the process $\mu^- + \mu^+ \to (\Phi^*) \to \tilde{\chi}_i^0 + \tilde{\chi}_j^0$.

From the effective cross section formula (39), let us determine the degree of longitudinal polarization of the neutralino by the standard formula :

$$P = \frac{\sigma^{(\Phi)}(h_1 = 1) - \sigma^{(\Phi)}(h_1 = -1)}{\sigma^{(\Phi)}(h_1 = 1) + \sigma^{(\Phi)}(h_1 = -1)} = \frac{(G_L^2 - G_R^2)\sqrt{\lambda(r_i, r_j)}}{(G_L^2 + G_R^2)(1 - r_i - r_j) - 4G_L G_R \sqrt{r_i \cdot r_j}}. \tag{44}$$

In the case when the neutralino $\tilde{\chi}_i^0$ and $\tilde{\chi}_j^0$ are polarized transversely, the differential cross section of the process $\ell^- + \ell^+ \to (\Phi^*) \to \tilde{\chi}_i^0 + \tilde{\chi}_j^0$ has the following form:

$$\frac{d\sigma^{(\Phi)}}{d\Omega} = \frac{1}{4} \frac{d\sigma_0^{(\Phi)}}{d\Omega}(1 + \eta\eta' A_\perp), \tag{45}$$

Where

$$\frac{d\sigma_0^{(\Phi)}}{d\Omega} = \frac{g_{\Phi\ell\ell}^2 g^2 \cdot s |D_\Phi(s)|}{512}\sqrt{\lambda(r_i, r_j)} \cdot [|a|^2 + |b|^2][(G_L^2 + G_R^2)(1 - r_i - r_j) - 4G_L G_R \sqrt{r_i \cdot r_j}] \tag{46}$$

– is the differential cross section of the process, η and η' – are the transverse components of the spin vectors of the neutralino $\tilde{\chi}_i^0$ and $\tilde{\chi}_j^0$, $A_\perp$ – is the degree of transverse polarization of the neutralino:

$$A_\perp = \frac{2\cos\varphi \cdot [G_L G_R(1 - r_i - r_j) - (G_L^2 + G_R^2)\sqrt{r_i \cdot r_j}]}{(G_L^2 + G_R^2)(1 - r_{\chi_i} - r_{\chi_j}) - 4G_L G_R \sqrt{r_i \cdot r_j}}. \tag{47}$$

Let us estimate the degree of longitudinal (P) and transverse ($A_\perp$) polarization in the process $\mu^- + \mu^+ \to (H^*) \to \tilde{\chi}_1^0 + \tilde{\chi}_2^0$. According to (33), the left and right Higgs boson H coupling constants of the neutralino pair $\tilde{\chi}_i^0$ and $\tilde{\chi}_j^0$ are equal to each other $G_L = G_R$. As a consequence, the degree of longitudinal polarization is zero, while the degree of transverse polarization of the neutralino is equal to the cosine of the angle φ :

$$A_\perp = \cos\varphi.$$

The degree of transverse polarization is maximum at angle $\varphi = 0$ ($A_\perp = 100\%$) and turns to zero at $\varphi = \frac{\pi}{2}$, then $A_\perp$ changes sign and decreases with increasing angle φ and reaches a minimum at $\varphi = \pi$: $A_\perp = -100\%$.

Figure 11 illustrates the energy dependence of the cross section of the process

$$\mu^- + \mu^+ \to (H^*) \to \tilde{\chi}_1^0 + \tilde{\chi}_2^0 \quad \text{at} \quad \mathrm{tg}\beta = 3,$$

$M_A = 500$ GeV, and $\Gamma_H = 4$ GeV.

It can be seen that the cross section is maximum when the energy of the muon-antimuon pair is equal to the Higgs boson mass: $\sqrt{s} = M_H = 500$ GeV.
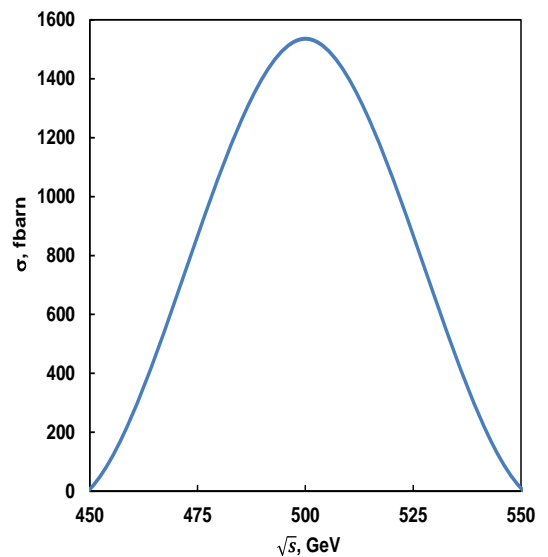

Fig. 11. Energy dependence of the cross section of the process $\mu^- \mu^+ \to (H^*) \to \tilde{\chi}_i^0 \tilde{\chi}_j^0$.

5. AMPLITUDE AND CROSS SECTION OF THE REACTION $\ell^- \ell^+ \to (\tilde{\ell}_L, \tilde{\ell}_R) \to \tilde{\chi}_i^0 \tilde{\chi}_j^0$

We turn to the study of diagrams c) and d) of Fig. 1 with the exchange of scalar $\tilde{\ell}_L$ and $\tilde{\ell}_R$ leptons

The Lagrangian of the interaction of lepton ℓ, neutralino $\tilde{\chi}_i^0$ and scalar lepton $\tilde{\ell}_L$ ($\tilde{\ell}_R$) is written as follows:

$$L_{\ell \tilde{\ell} \tilde{\chi}_i^0} = g f_{\ell i}^L (\bar{\ell} P_R \tilde{\chi}_i^0) \tilde{\ell}_R + g f_{\ell i}^R (\bar{\ell} P_L \tilde{\chi}_i^0) \tilde{\ell}_R + \text{e.c.} \tag{48}$$

Based on this Lagrangian, it is easy to write the amplitudes of the t- and u-channel diagrams c) and d) of Fig. 1:

$$M_c = i g^2 \{ D_{\tilde{\ell}_L}(t) f_{\ell i}^L f_{\ell j}^L (\bar{u}_i(k_1) P_L u_\ell(p_1))(\bar{\upsilon}_\ell(p_2) P_R \upsilon_j(k_2)) +$$

$$+ D_{\tilde{\ell}_R}(t) f_{\ell i}^R f_{\ell j}^R (\bar{u}_i(k_1) P_R u_\ell(p_1))(\bar{\upsilon}_\ell(p_2) P_L \upsilon_j(k_2)) \} , \tag{49}$$

$$M_d = -i g^2 \{ D_{\tilde{\ell}_L}(u) f_{\ell i}^L f_{\ell j}^L (\bar{u}_j(k_2) P_L u_\ell(p_1))(\bar{\upsilon}_\ell(p_2) P_R \upsilon_i(k_1)) +$$

$$+ D_{\tilde{\ell}_R}(u) f_{\ell i}^L f_{\ell j}^L (\bar{u}_j(k_2) P_R u_\ell(p_1))(\bar{\upsilon}_\ell(p_2) P_L \upsilon_i(k_2)) \} . \tag{50}$$

Here $t = (p_1 - k_1)^2$ and $u = (p_1 - k_2)^2$ – are the kinematic variables $D_{\tilde{\ell}_{L,R}}(x) = (x - m_{\tilde{\ell}_{L,R}}^2(x))^{-1}$, $f_{\ell i}^L$ and $f_{\ell j}^R$ – are the left and right interaction constants of the lepton, neutralino and scalar lepton [7, 15]:

$$f_{\ell i}^L = -\sqrt{2} \left[\frac{1}{\cos \theta_W} (T_3(\ell) - e_\ell \sin^2 \theta_W) Z_{i2} + e_\ell \sin \theta_W Z_{i1} \right],$$

$$f_{\ell i}^R = -\sqrt{2} e_\ell \sin \theta_W (\text{tg} \theta_W Z_{i2}^* - Z_{i1}^*), \tag{51}$$

e_ℓ and $T_3(\ell)$ – and is the electric charge and the third projection of the weak lepton isospin ℓ.

Now let us find the square of the matrix element $\overline{|M_c + M_d|^2}$, summed over the spin states of the neutralino (lepton and antilepton are longitudinally polarized):

$$\overline{|M_c + M_d|^2} = g^4 \{ (f_{\ell i}^L f_{\ell j}^L)^2 [|D_{\tilde{\ell}_L}(t)|^2 (p_1 \cdot k_1)(p_2 \cdot k_2) + |D_{\tilde{\ell}_L}(u)|^2 (p_1 \cdot k_2)(p_2 \cdot k_1) -$$

$$- 2 \text{Re}(D_{\tilde{\ell}_L}(t) D_{\tilde{\ell}_L}^*(u)) \eta_i \eta_j m_{\chi_i} m_{\chi_j} s](1 - \lambda_1)(1 - \lambda_2) + (f_{\ell i}^R f_{\ell j}^R)^2 |D_{\tilde{\ell}_R}(t)|^2 (p_1 \cdot k_1)(p_2 \cdot k_2) +$$

$$+ |D_{\tilde{\ell}_R}(u)|^2 (p_1 \cdot k_2)(p_2 \cdot k_1) - 2 \text{Re}(D_{\tilde{\ell}_R}(t) D_{\tilde{\ell}_R}^*(u)) \eta_i \eta_j m_{\chi_i} m_{\chi_j} s](1 + \lambda_1)(1 - \lambda_2) \} . \tag{52}$$

Here η_i, $\eta_j = \pm 1$ are the sign factors appearing from the operator products in the S-matrix in connection with Vick's theorems [15].

Having the square of the matrix element, it is easy to calculate in a standard way the differential effective cross section of this process in the center-of-mass system we used the following relations:

$$(p_1 \cdot k_1) = \frac{s}{4}[1 + r_i - r_j - \sqrt{\lambda(r_i, r_j)} \cos\theta], \quad (p_2 \cdot k_2) = \frac{s}{4}[1 - r_i + r_j - \sqrt{\lambda(r_i, r_j)} \cos\theta],$$

$$(p_1 \cdot k_2) = \frac{s}{4}[1 - r_i + r_j + \sqrt{\lambda(r_i, r_j)} \cos\theta], \quad (p_2 \cdot k_1) = \frac{s}{4}[1 + r_i - r_j + \sqrt{\lambda(r_i, r_j)} \cos\theta],$$

$$\frac{d\sigma^{(\tilde{\ell})}}{d(\cos\theta)} = \frac{g^4 s}{2^9 \pi} \sqrt{\lambda(r_i, r_j)} \{ (f_{\ell i}^L f_{\ell j}^L)^2 [|D_{\tilde{\ell}_L}(t)|^2 ((1 + r_i - r_j)(1 - r_i + r_j) + \lambda(r_i, r_j) \cos^2\theta -$$

$$-2\sqrt{\lambda(r_i, r_j)}\cos\theta) + \left|D_{\tilde{\ell}_L}(u)\right|^2((1+r_i-r_j)(1-r_i+r_j)+\lambda(r_i,r_j)\cos^2\theta +$$

$$+2\sqrt{\lambda(r_i,r_j)}\cos\theta) - 8\operatorname{Re}(D_{\tilde{\ell}_L}(t)D^*_{\tilde{\ell}_L}(u))\eta_i\eta_j\sqrt{r_ir_j}](1-\lambda_1)(1+\lambda_2) +$$

$$+(f^R_{\ell i}f^R_{\ell j})^2[\left|D_{\tilde{\ell}_R}(t)\right|^2((1+r_i-r_j)(1-r_i+r_j)+\lambda(r_i,r_j)\cos^2\theta - 2\sqrt{\lambda(r_i,r_j)}\cos\theta) +$$

$$+\left|D_{\tilde{\ell}_R}(u)\right|^2((1+r_i-r_j)(1-r_i+r_j)+\lambda(r_i,r_j)\cos^2\theta + 2\sqrt{\lambda(r_i,r_j)}\cos\theta) -$$

$$-8\operatorname{Re}(D_{\tilde{\ell}_R}(t)D^*_{\tilde{\ell}_R}(u))\eta_i\eta_j\sqrt{r_ir_j}](1+\lambda_1)(1-\lambda_2). \tag{53}$$

It follows from this expression that, in the annihilation process, the lepton and the antilepton must have opposite helicities, either $\lambda_1 = -\lambda_2 = +1$, or $\lambda_1 = -\lambda_2 = -1$.

Integrating by the angles of departure of the neutralino , we finally obtain

$$\sigma^{(\tilde{\ell})}_{tot} = \frac{1}{2}\sigma_{\tilde{\ell}}(2-\delta_{ij}), \tag{54}$$

where

$$\sigma_{\tilde{\ell}} = \frac{g^4\sqrt{\lambda(r_i,r_j)}}{32\pi s}\times$$

$$\times\left\{(f^L_{\ell i}f^L_{\ell j})^2\left[2 - \frac{r_{\tilde{\ell}_L}}{r_ir_j+r_{\tilde{\ell}_L}(1+r_{\tilde{\ell}_L}-r_i-r_j)} - \frac{1}{\sqrt{\lambda(r_i,r_j)}}\left(r_i+r_j-2r_{\tilde{\ell}_L} - \frac{2\eta_i\eta_j\sqrt{r_ir_j}}{1+2r_{\tilde{\ell}_L}-r_i-r_j}\right)L(\tilde{\ell}_L)\right] + \right.$$

$$\left. +(f^R_{\ell i}f^R_{\ell j})^2\left[2 - \frac{4r_{\tilde{\ell}_R}}{1+2r_{\tilde{\ell}_R}-r_i-r_j} + \frac{1}{\sqrt{\lambda(r_i,r_j)}}\left(r_i+r_j-2r_{\tilde{\ell}_R} - \frac{2\eta_i\eta_j\sqrt{r_ir_j}}{1+2r_{\tilde{\ell}_R}-r_i-r_j}\right)L(\tilde{\ell}_R)\right]\right\}, \tag{55}$$

$$L(\tilde{\ell}_{L,R}) = \ln\left|\frac{1+2r_{\tilde{\ell}_{L,R}}-r_i-r_j+\sqrt{\lambda(r_i,r_j)}}{1+2r_{\tilde{\ell}_{L,R}}-r_i-r_j-\sqrt{\lambda(r_i,r_j)}}\right|, \quad r_{\tilde{\ell}_L} = \left(\frac{m_{\tilde{\ell}_L}}{\sqrt{s}}\right)^2, \quad r_{\tilde{\ell}_R} = \left(\frac{m_{\tilde{\ell}_R}}{\sqrt{s}}\right)^2,$$

$\delta_{ij}=0$ at the production of different neutralinos ($i \neq j$) and $\delta_{ij}=1$ at the production of identical neutralinos ($i=j=1, 2, 3, 4$), $m_{\tilde{\ell}_L}$ and $m_{\tilde{\ell}_R}$ – are the masses scalar lepton $\tilde{\ell}_L$ and $\tilde{\ell}_R$.
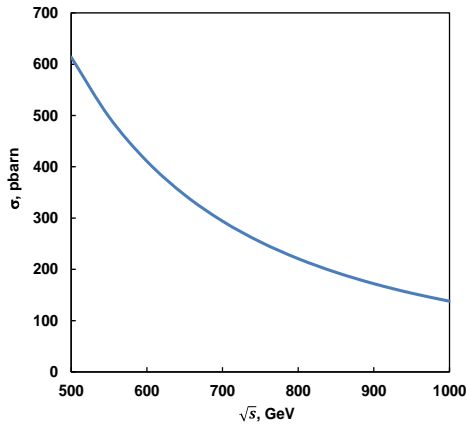

Fig. 12. Energy dependence of the cross section of the reaction $e^-e^+ \to (\tilde{\ell}_L; \tilde{\ell}_R) \to \tilde{\chi}_2^0\tilde{\chi}_2^0$.

Figure 12 illustrates the dependence of the effective cross section of the process $e^- + e^+ \to (\tilde{\ell}_L; \tilde{\ell}_R) \to \tilde{\chi}_2^0 + \tilde{\chi}_2^0$ on the energy $\sqrt{s}$ of the electron-positron beams at parameter values $m_{\tilde{\ell}_L} = m_{\tilde{\ell}_R} = 40$ GeV, $x_W = 0.2315$, $M_2 = 2M_1 = 150$ GeV, $\mu = 200$ GeV, $\text{tg}\beta = 3$. As can be seen from the figure, the cross section of the process $e^- + e^+ \to (\tilde{e}_L; \tilde{e}_R) \to \tilde{\chi}_2^0 + \tilde{\chi}_2^0$ decreases with increasing energy of the electron-positron beams.

CONCLUSION

Thus, we have discussed the process of neutralino pair production in arbitrarily polarized lepton-antilepton (electron-positron or muon-antimuon) collisions $\ell^- + \ell^+ \to \tilde{\chi}_i^0 + \tilde{\chi}_j^0$. Diagrams with exchanges of neutral Z-bosons, scalar H and h, pseudoscalar A-bosons, and scalar $\tilde{\ell}_L$ and $\tilde{\ell}_R$ leptons have been studied in detail. Expressions for the differential and integral cross sections of the process are obtained, and the longitudinal and transverse spin asymmetries due to lepton-antilepton pair polarizations, the forward-backward angular asymmetry, and the degrees of longitudinal and transverse neutralino polarization are determined. The angular and energy dependences of these characteristics and the total cross section of the reaction are studied in detail. The results of the calculations are illustrated by graphs.

APPENDIX

Here we give the expressions for the lepton tensor $L_{\mu\nu}$ and the neutralino tensor $\chi_{\mu\nu}$:

$$L_{\mu\nu} = \frac{1}{2}(g_L^2 + g_R^2)[p_{1\mu}p_{2\nu} + p_{2\mu}p_{1\nu} - (p_1 \cdot p_2)g_{\mu\nu} - m_\ell^2(s_{1\mu}s_{2\nu} + s_{2\mu}s_{1\nu} - (s_1 \cdot s_2)g_{\mu\nu})] +$$

$$+ \frac{1}{2}(g_L^2 - g_R^2)m_\ell[p_{1\mu}s_{2\nu} + s_{2\mu}p_{1\nu} - (p_1 \cdot s_2)g_{\mu\nu} - s_{1\mu}p_{2\nu} - p_{2\mu}s_{1\nu} + (p_2 \cdot s_1)g_{\mu\nu}] +$$

$$+ g_L g_R\{(p_1 \cdot s_2)[s_{1\mu}p_{2\nu} + p_{2\mu}s_{1\nu} - (p_2 \cdot s_1)g_{\mu\nu}] - (p_1 \cdot p_2)[s_{1\mu}s_{2\nu} + s_{2\mu}s_{1\nu} - (s_1 \cdot s_2)g_{\mu\nu}] +$$

$$+ (p_2 \cdot s_1)[s_{2\mu}p_{1\nu} + p_{1\mu}s_{2\nu}] - (s_1 \cdot s_2)[p_{1\mu}p_{2\nu} + p_{2\mu}p_{1\nu}]\} + \frac{1}{2}(g_L^2 + g_R^2)(-m_\ell)[(\mu\nu p_1 s_2)_\varepsilon +$$

$$+ (\mu\nu p_2 s_1)_\varepsilon] + \frac{1}{2}(g_L^2 - g_R^2)i[-(\mu\nu p_1 p_2)_\varepsilon + m_\ell^2(\mu\nu s_1 s_2)_\varepsilon] + g_L g_R im_\ell[(\mu\nu p_1 s_1)_\varepsilon - (\mu\nu p_2 s_2)_\varepsilon];$$

$$\chi_{\mu\nu} = \frac{1}{2}(G_L^2 + G_R^2)[k_{1\mu}k_{2\nu} + k_{2\mu}k_{1\nu} - (k_1 \cdot k_2)g_{\mu\nu} - m_{\chi_i}m_{\chi_j}(s_\mu s'_\nu + s_\nu s'_\mu - (s \cdot s')g_{\mu\nu}] +$$

$$+ \frac{1}{2}(G_L^2 - G_R^2)[m_{\chi_j}(k_{1\mu}s'_\nu + k_{1\nu}s'_\mu - (k_1 \cdot s')g_{\mu\nu} - m_{\chi_i}(s_\mu k_{2\nu} + s_\nu k_{2\mu} - (k_2 \cdot s)g_{\mu\nu})] +$$

$$+ G_L G_R[-m_{\chi_i}m_{\chi_j}g_{\mu\nu} - (k_1 \cdot k_2)(s_\mu s'_\nu + s_\nu s'_\mu - (s \cdot s')g_{\mu\nu}) - (s \cdot s')(k_{1\mu}k_{2\nu} + k_{2\mu}k_{1\nu}) +$$

$$+ (k_1 \cdot s')[s_\mu k_{2\nu} + s_\nu k_{2\mu} - (k_2 \cdot s)g_{\mu\nu}] + (s \cdot k_2)[k_{1\mu}s'_\nu + k_{1\nu}s'_\mu] + \frac{1}{2}(g_L^2 + g_R^2)i[m_{\chi_j}(\mu\nu k_1 s')_\varepsilon +$$

$$m_{\chi_i}(\mu\nu k_2 s)_\varepsilon] + \frac{1}{2}(g_L^2 - g_R^2)i[(\mu\nu k_1 k_2)_\varepsilon - m_{\chi_i}m_{\chi_j}(\mu\nu s s')_\varepsilon] + g_L g_R i[m_{\chi_i}(\mu\nu k_2 s')_\varepsilon + (\mu\nu k_1 s)_\varepsilon],$$

the notation is introduced here $(\mu\nu ab)_\varepsilon = \varepsilon_{\mu\nu\rho\sigma}a_\rho b_\sigma$.

———————————————————————

[1] ATLAS Collaboration. Observation of a new particle in the search for the Standard Model Higgs boson with the ATLAS detector of the LHC. Phys. Letters, 2012, B 716, p. 1-29.

[2] CMS Collaboration. Observation of a new boson at mass of 125 GeV with the CMS experiment at the LHC. Phys. Letters, 2012, B 716, p. 30-60.

[3] *V.A. Rubakov.* UFN, 2012, V.182, No 10, p.1017-1025 (in Russian).

[4] *A.V. Lanev.* CMS Collaboration results: Higgs boson and search for new physics. UFN, 2014, V. 184, No 9, p. 996-1004 (In Russian).

[5] *D.I. Kazakov.* The Higgs boson is found: what is next? UFN, 2014, V. 184, No 9, p. 1004-1017 (In Russian).

[6] ATLAS Collaboration. Measurements of Higgs boson production and couplings in diboson final states with the ATLAS detector at the LHC. Phys. Letters, 2013, B 726, p. 88-119.

[7] *A. Djouadi.* The Anatomy of Electro-Weak Symmetry Breaking. Tome II: The Higgs boson in the Minimal Supersymmetric Standard Model. arXiv: hep-ph/0503172v2, 2003; DOI: 10.1016/j.physrep.2007.10.004.

[8] *J.F. Gunion, H.E. Haber.* Higgs bosons in Supersymmetric. Phys. Rev., 2003, D 67, p. 0750.19.

[9] *D.I. Kazakov.* Supersymmetry on the Run: LHC and Dark Matter. Nucl. Phys. B Proc. Suppl.,

2010, Vol. 203-204, p. 118-154.

[10] *R.K. Barman et al.* Current status of MSSM Higgs sector with LHC 13 TeV data. Eur. Phys. J. Plus, 2019, Vol. 134: 150, No 4 arXiv: 1608.02573v3, [hep-ph]

[11] *M.M. El Kheishen, A.A. Shafik, A.A. Aboshousha.* Phys. Rev., 1992, Vol. 45, No. 11, pp. 4345-4348. DOI:https://doi.org/10.1103/PhysRevD.45.4345

[12] *A. Djouadi, P. Janot, J. Kalinowski, P.M. Zerwas.* SUSY Decays of Higgs Particles. CERN PPE/96-34, 1996, 13p.

[13] *A. Djouadi, J. Kalinowski, P. Ohmann, P.M. Zerwas.* Heavy SUSY Higgs bosons at e⁻e⁺ linear colliders. Z. Phys., 1997, C 74, p. 93-111.

[14] *A. Bartl, H. Fraas, W. Majerotto.* Signatures of chargino production in e⁺e⁻collisions. Z. Phys., 1986, B 30, p. 441-449.

[15] *A. Bartl, H. Fraas, W. Majerotto.* Production and decay of neutralinos in e⁺e⁻-collisions. J. Nucl. Phys., 1986, B 278, p. 1-25

[16] *E.Ch. Christova, N.P. Nedelcheva.* Neutralino production on polarized e⁺e⁻-collisions. Preprint, Dubna, 1988, E2-88-607, 14p.

[17] *S.M. Bilenky, N.P. Nedelcheva.* Possible test for supersymmetry in e⁻e⁺-collisions with polarized beams. Preprint, Dubna, 1986, E2-88-494, 10p.

[18] *P. Cheapetta, J. Soffer, P. Taxil, F.M. Renard, P. Sorba.* Supersymmetry and polarization in e⁻

e^{+}-collisions (I). Nucl. Phys., 1984, Vol. B259, p. 365-396.

[19] *S.K. Abdullayev, M.Sh. Gojayev, A.K. Gulayeva.* The production of a chargino pair in polarized lepton-antilepton collisions (I). AJP, Fizika, 2020, V. XXVI, No 3, p. 20-30.

[20] *S.K. Abdullayev, M.Sh. Gojayev, A.K. Gulayeva.* The production of a chargino pair in polarized lepton-antilepton collisions (II). AJP, Fizika, 2020, V. XXVI, No 4, p. 19-27.

THE FERMI LEVEL TUNING BY ANNEALING IN SELENIUM VAPOR AND ARGON PLASMA ETCHING OF Bi_2Se_3 SURFACES

S.Sh. GAHRAMANOV[1], Y.A. ABDULLAYEV[1], A.A. BADALOV[1], K.M. JAFARLI[1], N.A. ABDULLAYEV[1,2], K.Sh. GAHRAMANOV[1]

[1]Institute of Physics of ANAS, AZ1143, H.Javid ave., 131, Baku, Azerbaijan
[2]Baku State University, AZ1148, Z. Khalilov str., 23, Baku, Azerbaijan
e-mail: samir.gahramanov@gmail.com

In the near-surface area of Bi_2Se_3 crystals, in order to reduce concentration of charge carriers and Se vacancies, which are electronic donors, annealing in selenium vapor was used. It has been established that the most optimal mode is annealing at a temperature of 100-150 °C for 70 hours. Effective impact on the surface condition with an identical purpose is exerted by processing the sample in a glow discharge in an argon medium. It was determined that treatment with an ions dose of $\sim 1.1 \cdot 10^{17}$ ion/cm^{-2}, both after and without preliminary treatments in the form of annealing or chemical etching, leads to a significant decrease in concentration of carriers in crystals near-surface area.

INTRODUCTION

Bi_2Se_3 crystals of $A^V_2B^{VI}_3$ type semiconductors are topological insulators (TI) –materials, with previously predicted and recently detected condensed state of matter [1-4], which allows unhindered movement of electrons in surface layers due to strong spin-orbit interaction and formation spin splitted surface states, which topologically protected from scattering by defects by symmetry with respect to time reversal. A continuous spectrum of these surface states forms a Dirac cone around point Γ of the Brillouin zone, where the direction of the spin moment is orthogonal to the wave vector. These materials surfaces study is a scientific and practical interest in the creation of high-speed devices and the miniaturization of their working elements.

The crystal structure of the Bi_2Se_3 compound belongs to the space group D^5_{3d} and has a layered structure, represents a set of layers - quintets, perpendicular to the third-order symmetry axis C_3. Each quintet (QL) consists of five layers that alternate in the sequence $Se^{(1)}–Bi–Se^{(2)}–Bi–Se^{(1)}$. Chemical bonds in compound Bi_2Se_3 inside quintets are ion-covalent type, the connection between quintets carried by van der Waals forces.

These materials are doped to remove defects in the bulk of the material, which creating energy levels in the band gap and fixing the position of the Fermi level [5], becouse of control Fermi level relative to the Dirac node is a necessary condition for the practical use of topological insulators.The position of Fermi level is closely related to morphology and composition of surface, which affect the surface states in TI. In [6], it was noted that the real cleaved surface of these compounds consists of terraces with a step height, mostly a multiple of QL, against which terraces (islands) ending in semimetal atoms are observed.The presence of an additional surface charge on these islands shifts the E_F position to the region of higher energies. Although it is known that topological surface states (*TSS*) are resistant to non-magnetic surface disturbances, their dispersion of zones and spatial distribution are yet sensitive to surface defects.In particular, *Se* vacancies significantly modify the band structure of the Bi_2Se_3 surface. Enrichment with bismuth is usually observed with the growth of a crystal of stoichiometric composition due to the relative easyvolatility of the chalcogen. There are differences in the energy of the formation of *Se* vacancies, which are the main donor defects, in two nonequivalent layers of the chalcogen $Se^{(1)}$ and $Se^{(2)}$, and the vacancies in the position $Se^{(1)}$ have the lowest formation energy of all intrinsic defects.This leads to the formation of *n*-type defects without significant compensation by *p*-type defects to a level of at least 0.1 eV above the bottom of the conduction band. In the presence of *Se* vacancies on the surface, several dangling bonds appear that interact with *TSS*, three dangling *Bi* bonds form under one Se vacancy, and, accordingly, three new states near the *K*point of Brillouin zone of the surface.The state at 0.4 eV is mainly associated with the *p*-orbitals of three *Bi* atoms, which have dangling bonds. The states below E_F are formed mainly by these three *Bi* atoms and partially by the *p*-states of $Se^{(2)}$ atoms [7].The vacancies of *Se* and antisite defects of Se_{Bi}, as the effect of electron doping, shift the Fermi energy upward to the conduction band; with increasing their density, the band structure becomes more complicated. A small number of *Se* vacancies on the surface do not destroy *TSS*, and with an increase in their number that violates the spin- orbit interaction, topological surface states can down from the first to the second quintet layer and separate from vacancies [7].

Annealing in selenium vapor leads to decrease in vacancies and number of charge carriers [8]. In [9, 10], it was shown that along with terraces ending chalcogen, terraces ending in bismuth can be observed, in [7] to study the band structure and charge density of surface states with a large number of *Se*-vacancies and layers ending *Se* or *Bi*, first-principle calculations were used. The substitutional defects of $Se^{(1)}$ edge atoms in

quintets should not cross the critical threshold, since a change in the *p*-state symmetry will affect the probability of inversion of states in the *Γ* point vicinity of Brillouin zone. In some works, the issue of surface stability and stability during exposure in air was related to the dependence on the surface imperfection, such as vacancies, substitution defects, dangling bonds [11, 12].The formation of oxides up to 1 nm thick was observed, which could lead to a deterioration of topological surface states [13].Oxidation of bismuth atoms is possible with selenium vacancies or substitution of upper layers selenium by bismuth, in this case, dangling bismuth bonds that exist on the surface can interact with oxygen, and surface oxidation begins primarily with them. *$Bi_2Se_3(0001)$* surface properties stability, and for most layered crystals, is related to the degree of surface perfection, since the *$Se^{(1)}$* atoms of ideal *(0001)* surface have closed electron shells with bonds directed inside the quintets and have no unsaturated bonds [12].An ideal *Bi_2Se_3* surface ending in a *$Se^{(1)}$* layer has topological surface states (*TSS*) described by a single Dirac cone inside the bulk gap [7], which is consistent with calculations [2] and experiment [3].

Argon plasma etching is used in combination with lithographic methods for the manufacture of devices based on a topological insulator. Surface treatment with argon plasma [14] was used to reduce imperfection and to understand the effect of argon etching on topological insulators.

The purpose of this work is to study the surface properties of *(0001)Bi_2Se_3* and establish the relationship between structural excellence and electronic properties during annealing in selenium vapor and treatment with argon plasma.

EXPERIMENT AND RESULTS

The morphology and electronic properties of the *(0001)* surface were studied, and the effect of annealing in selenium vapor and treatment with argon plasma on the surface properties of *Bi_2Se_3* crystal was studied. We studied *n*-type samples of *Bi_2Se_3* crystals obtained by the Bridgman method with a carrier concentration of $n = 1.1 \times 10^{19}$ cm^{-3} and a thermopower $\alpha = -52$ μV /deg. The crystal surfaces obtained by cleavage along the chipped plane *(0001)* were studied.The surface composition of single crystals was studied on aX'Pert Pro XRD X-ray diffractometer of Panalytical B.V. (radiation at 45 kV and 40 mA in CuKα, scanning at 0.01 2θ ° steps and 1.2 s time).Surface images were obtained on an NC-AFM brand AFM at room temperature. The electronic properties were investigated by modulation spectroscopy of a weak-field electric reflection (ER) of light, using a 1-molar solution of *KCl* in water.The surface field was varied by applying an external potential difference to the electrostatic capacitor, one of the electrodes of which was a semiconductor, at a modulation frequency of the surface potential of the semiconductor of 512 Hz. The electric field of the surface space charge was regulated by applying a constant potential, bias. The effect of surface treatment on optical transitions near the critical

points of the band structure made it possible to judge the state of the surface by a changing the broadening parameter, height and peak shift of the ER spectrum.A type of electro-optical effect, in which the position of Fermi level on the surface of a semiconductor changes under the influence of an external field or a charge of surface states, is usually called the zone filling effect (ZFE). In the ER spectra, the effect can manifest itself not only at the edge of the fundamental absorption of the material, but also at all allowed interband transitions, including unoccupied states near the Fermi level. When the electric bias is applied, the Fermi level remains unchanged in the bulk of the crystal, however, near the surface the filling of zones changes along the direction from the depth of the volume to the surface. In the method of electroreflection, light penetrating to a certain depth probes levels with different filling levels. Moreover, the mechanism of electroreflection is not just a transition associated with a critical point in the Brillouin zone. For the regime of accumulation on the surface, the modulation of band filling becomes the dominant ER mechanism.With strong doping of narrow-gap semiconductors, the Fermi level is advanced far into the conduction band. Under these conditions, the Franz-Keldysh effect in electroreflection is suppressed and practically does not appear.If the Fermi level is near the bottom of the conduction band, then both effects contribute to the ER mechanisms: the ZFE, which in the general case gives a broadened monopolar structure with an energy shift that grows with an applied field, and Franz-Keldysh, which appears as a bipolar line corresponding to a certain critical point [15,16].When the electric field creates a depleting bending of the zones, the Franz-Keldysh effect can become the predominant contribution to ER.
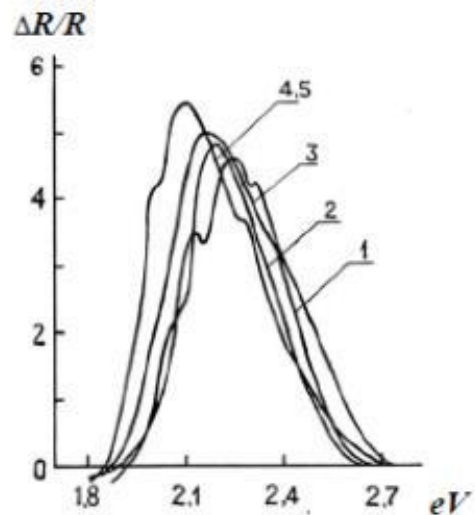

Fig. 1. ER spectra of Bi₂Se₃ crystals annealed in Se vapor for 70 hours at various temperatures:1-initial surface, 2-5 at 100, 150, 250, 300 ^{0}C, at bias voltages -0.3V, modulation 0.4V.

The ER spectra of *Bi_2Se_3* samples annealed in selenium vapor at various temperatures and durations were measured in unpolarized light at constant bias and modulation voltages in the spectral range of 1.8 - 2.7

eV, shown in Fig. 1, were studied T_3 and $T_{4.3}$ (notation according to [17]) structures of spectra.
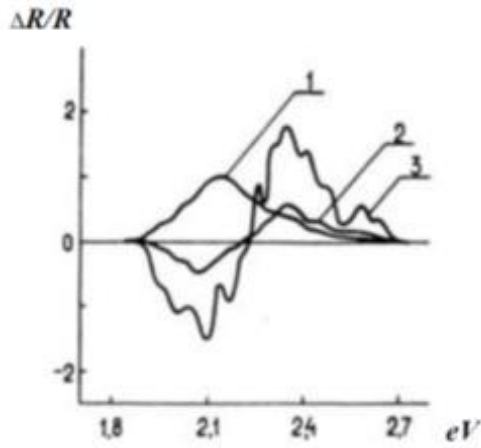

Fig. 2. ER spectra of Bi$_2$Se$_3$ crystals annealed in Se vapor at 300 ^{0}C for 70 hours, at bias and modulation voltages, 1-3: +0.3 and 0.5; +0.5 and 0.5; +0.8 and 0.5 V, respectively.

In the ER spectra of *Bi$_2$Se$_3$* samples annealed in selenium vapor on Fig. 1, curve 2 shows a decrease in half-width of the integral spectral line and a shift of maximum to the longer wavelength region compared with the spectrum from the initial surface on curve 1. Changes in the spectrum indicate a decrease in the concentration of free electrons with a simultaneous decrease in scattering on surface defects, which can be explained by the filling of selenium vacancies upon annealing.This is confirmed by the disappearance of bismuth atoms peaks in X-ray diffraction patterns from the surface annealed in selenium vapor, see Fig. 3, b), compared with the initial surface containing bismuth peaks, see Fig. 3, a). For *Bi$_2$Se$_3$* intrinsic defects in selenium enriched compositions, the energy of the formation of Se vacancies increases, and the formation energy of the acceptor-type bismuth vacancies decreases.Based on this a lower n-type conductivity can be expected when the Fermi level moves into the band gap in the volume, trying to cross the energy of formation of selenium and bismuth vacancies. Reduction of n-type defects - selenium vacancies also contributes to a decrease in electron concentration.

The shape of curve 3 in Fig. 1 shows that a further increase in the amplitude and shear with an increase in the annealing temperature is accompanied by an increase in the integral half-width of the spectral line in comparison with the initial surface. The intensification of light scattering that is already manifesting can be associated with the diffusion of excess *Se* atoms into the crystal lattice as defect centers, as well as with the aggregation of unevenly distributed surface nanoformations - vapor deposition products, see Fig. 4.In this case, the probability of occurrence of anti-structural defects of *Se$_{Bi}$*, is high, the formation energy of which becomes the lowest in the band gap [7], and for all growth variants they are donors, even if the Fermi level is at the bottom of the conduction band or is slightly higher.
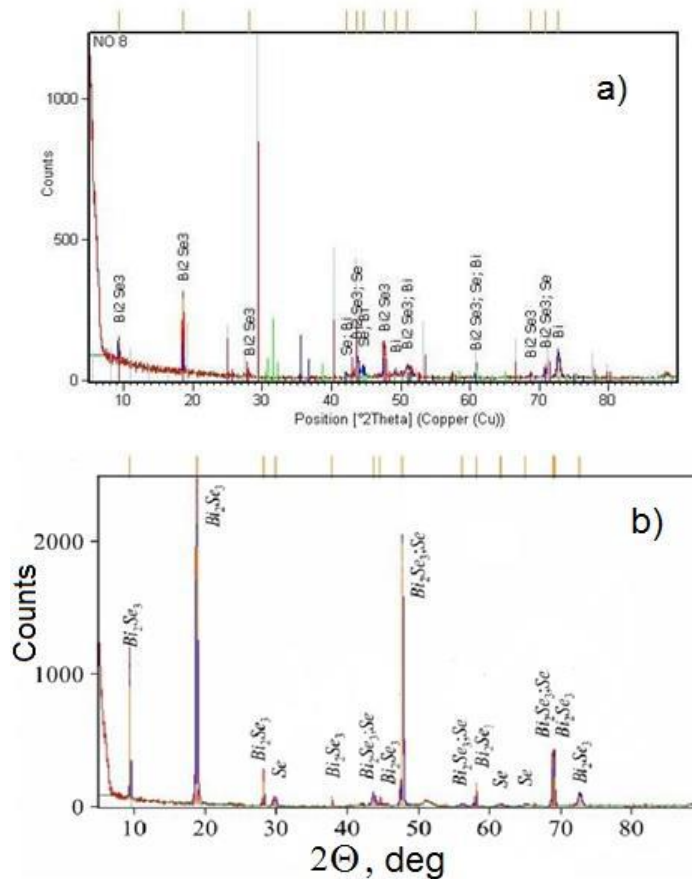

Fig.3. X-ray diffraction pattern from the initial surface of Bi$_2$Se$_3$ - a); and from the surface of Bi$_2$Se$_3$ annealed in selenium vapor for 70 hours at 200^{0}C - b).
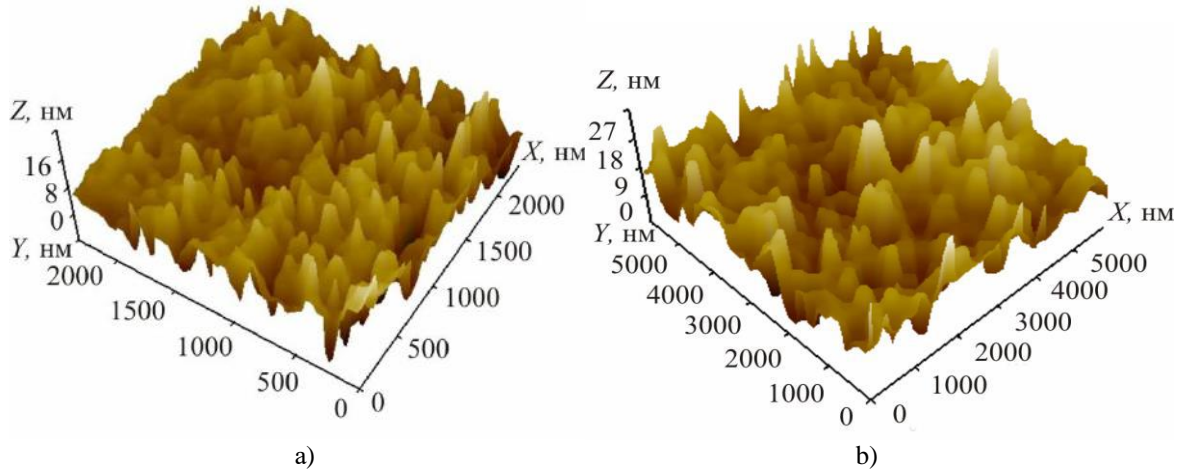
a)   b)

Fig. 4. 3D AFM images at room temperature of Bi_2Se_3 (0001) surface annealed in Se vapor for 70 hours, at 150^0C - a)   and at 300^0C - b).

This trend persists until the annealing temperature of $250\text{-}300^0C$, as can be seen in Fig. 4 a) and b), an increase in the annealing temperature leads to nanoislands enlargement on the surface. A further increase in the temperature of *Se* vapors up to 350^0C does not lead to any significant changes in the ER spectrum.

As noted above, in the electroreflection of crystals with a high carrier concentration ($n\approx10^{18}\text{-}10^{20}$ см$^{-3}$), the modulation of band filling prevails, the dominant role of which increases when enrichment bias is applied. The ER spectrum main features corresponding to the band filling modulation mechanism is its monopolarity and independence from light polarization. Under certain conditions, in degenerate *Bi_2Se_3* crystals, it is possible to partially suppress the ZFE mechanism and activate Franz-Keldysh effect in the formation of the ER spectrum. This possibility was realized by transferring the bias into the depletion mode, as well as by treating the surface of the sample with argon plasma while maintaining a negative enrichment bias. Corresponding measurements were carried out on *n*-type *Bi_2Se_3* crystals with $n=1,1x10^{19}$ cm^{-3}.

The polarization anisotropy coefficient for monopolar spectra measured in the region of even weak surface enrichment turned out to be 1.3. When measuring the ER in the region of depletion bending zones, a monopolar line was transformed into a structure of two opposite in sign lines with approximately equal amplitudes, and the polarization anisotropy coefficient increased to 2.2.

To observe the polarization-dependent dipolar spectrum in the samples annealed in selenium vapor at 300°C for 70 hours, a larger depletion bias was required, causing the zones to bend upward (Fig. 2). This indicates an increase in the concentration of charge carriers with increasing annealing temperature, which is associated with the diffusion of excess Se atoms into the crystal lattice as defective donor centers. A similar transformation of the monopolar polarization-isotropic spectrum from the initial surface of the sample into a dipolar anisotropic occurred after the sample was treated in a glow discharge in argon,

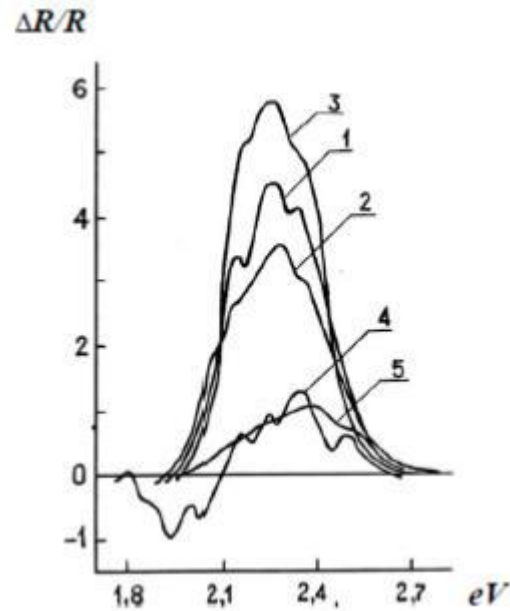and the effect occurred while maintaining a negative bias on the sample.

Fig. 5. ER spectra of Ar-plasma treated Bi_2Se_3 crystals: 1- initial surface, 2-5– treatment in the discharge by ion doses, respectively, $D\approx 3,6\cdot10^{15}$; $1,1\cdot10^{16}$; $1,1\cdot10^{17}$; $4,3\cdot10^{17}$, at bias voltages -0.3V, modulation 0.4V.

Studied crystals exposed to glow discharge in argon medium with ions doses $D\approx 3,6\cdot10^{15}$; $1,1\cdot10^{16}$; $1,1\cdot10^{17}$; $4,3\cdot10^{17}$ ion /cm^{-2}, the discharge current density was 0.2 A /m^2 at a voltage of 1.0-1.2 kV, the treatment time varied from 30s to 60min. Figure 2 shows the light ER spectra from the surfaces of *Bi_2Se_3* crystals before and after treatment in Ar-plasma. Processing of fresh cleavage for 30s led to a weakening and broadening of the spectrum (curve 2) in comparison with the spectrum from initial surface (curve 1). Note that in the case of Bi2Se3, a broadened structure of the spectrum is observed and the phenomenological broadening parameter $\Gamma=\hbar/\tau$ determined by the scattering processes by impurities,

phonons, and other imperfections in the crystal structure is only an integral part of the general broadening of spectrum.A significant part of the half-width of the spectrum is associated with field broadening, which is sufficiently large at high levels of bias and modulation on the crystal.Leaving the bias and modulation on the samples unchanged by changes in the overall broadening of the spectra at various stages of plasma treatment, one can judge the changes in the imperfection of crystal near-surface layer.From these positions, the shape of curve 2 of spectrum indicates the appearance of a defective layer on crystal surface, probably due to the deposition of argon ions and their partial incorporation with the formation of radiation defects in near-surface region.With an increase in plasma treatment time to 1.5 min, the amplitude of the spectrum grows (curve 3) and reaches a value greater than that for the initial surface (curve 1), while the broadening of the spectrum decreases. Consequently, during the treatment of 1.5 min, corresponding to the dose of argon ions incident on the surface, $D \approx 1,1 \cdot 10^{16}$ ion / см$^{-2}$, prevails process of plasma etching the surface.Further processing with argon plasma up to 15 min. with an ion dose of $\sim 1,1 \cdot 10^{17}$ ion/cm^2, the amplitude decreased and the monopolar spectrum was transformed into two split peaks of opposite sign (curve 4). Apparently, after plasma cleansing of the surface, selenium atoms are knocked out, followed by adsorption on broken bonds of oxygen atoms of the air, which have a high electron affinity.As a result, a layer of positive space charge can form in the near-surface region due to localization of surface electrons on oxygen atoms and receiving of a near-surface electron-depleted layer.Although in this case, judging by the results of studies [14], where the action of argon plasma causes the broadening of characteristic Raman peaks

without a significant change in the position of the peak, we can only assume structural transformation of the surface, and not its oxidation.Taking into account the high concentration of free charge carriers and the degeneracy of the samples, we note that the spectra are 1, 2, 3, in Fig. 5 correspond to the effect of band filling, and the dipolar shape of spectrum 4 and the long-wavelength shift of its energy position indicate that the surface of the semiconductor has turned into a non-degenerate state. Processing in Ar-plasma for 1 hour leads the surface to almost complete structural disorder (curve 5).

CONCLUSION

The results of these studies show that, for layered Bi_2Se_3 crystals, along with the deposition of NO_2 [18], HfO_2 [19] and other surface hole donors, by which it was possible to achieve the alignment of the Dirac cone site with EF, annealing in selenium vapor can be used to reduce vacancies Se, which are electronic donors: it has been established that the most optimal mode is annealing at a temperature of 100-150^{0}C for 70 hours.Effective impact on the surface condition with an identical purpose is exerted by processing the sample in a glow discharge in an argon medium. It was determined that treatment with an ion dose of $\sim 1,1 \cdot 10^{17}$ ion/cm^2, both after and without preliminary treatments in the form of annealing or chemical etching, leads to a significant decrease in concentration of carriers in crystals near-surface area.

———————————————

[1] *L. Fu, C.L. Kane, E.J. Mele.* Topological insulators in three dimensions.Phys. Rev. Lett., 2007, vol. 98, 106803, doi.org/10.1103/

[2] *H. Zhang, C.X. Liu, X.L. Qi, X. Dai, Z. Fang, S.C. Zhang.* Topological insulators in Bi_2Se_3, Bi_2Te_3 and Sb_2Te_3 with a single Dirac cone on the surface. Nature Phys., 2009, vol. 5, iss. 6, pp. 438-442.

[3] *Y. Xia, D. Qian, D. Hsieh, L. Wray, A. Pal, H. Lin, A. Bansil, D. Grauer, Y.S. Hor, R.J. Cava, M.Z. Hasan.* Observation of a large-gap topological-insulator class with a single Dirac cone on the surface. Nature Phys, 2009, vo l. 5, 398–402, doi:10.1038/nphys1274

[4] *M.Z. Hasan, C.L. Kane.* Topological insulators. *Rev. Mod. Phys.* 2010, vol. 82, 3045-3067.

[5] *D.O. Scanlon, P.D.C. King, R.P. Singh, A. de la Torre, S. McKeown Walker, G. Balakrishnan, F. Baumberger, C.R.A. Catlow.* Controlling bulk conductivity in topological insulators: Key role of anti-site defects. Advanced Materials, 2012, vol. 24, iss.16, pp 2154–2158./dx.doi.org/10.1002/adma.201200187.

[6] *S.V. Eremeev, Yu.M. Koroteev,*

E.V. Chulkov. Journal of Experimental and Theoretical Physics Letters, 2010, 91:8, 387–391. doi.org/10.1134/S0021364010080059

[7] *B. Yan, D. Zhang, C. Felser.* Phys. Status Solidi RRL, 2013, vol. 7, No.1–2, pp. 148-150. doi: 10.1002/pssr.201206415

[8] *G. Martinez, B.A. Piot, M. Hakl, M. Potemski, Y.S. Hor, A. Materna, S.G. Strzelecka, A. Hruban, O. Caha, J. Novák, A. Dubroka, Č. Drašar, M. Orlita.* Determination of the energy band gap of Bi_2Se_3. Scientific reports. 2017, vol. 7, 6891. doi: 10.1038/s41598-017-07211-x.

[9] *Sz. Winiarz, R. Czajka, S. Suto, P. Loštak, S. Szuba, A. Kasuya.* STM and STS investigations of Bi_2Te_3 surface. ActaPhysicaPolonica A. 2003, vol.104, iss.3-4, pp.389-395.

[10] *S. Urazhdin, D. Bilc, S.D. Mahanti, S.H. Tessmer, T. Kyratsi, M.G. Kanatzidis.* Surface effects in layered semiconductors Bi_2Se_3 and Bi_2Te_3. *Phys. Rev. B,* 2004, vol. 69, 085313, ().

[11] *V.A. Golyashov, K.A. Kokh, S.V. Makarenko, K.N. Romanyuk, I.P. Prosvirin, A.V. Kalinkin, O.E. Tereshchenko, A.S. Kozhukhov, D.V. Sheglov, S.V. Eremeev, S.D. Borisova,*

E.V. Chulkov. Inertness and degradation of *(0001)* surface of Bi_2Se_3 topological insulator. J. Appl. Phys., 2012, vol. 112, 113702; doi:10.1063/1.4767458

[12] *O.E. Tereshchenko, K.A. Kokh, V.V. Atuchin, K.N. Romanyuk, S.V. Makarenko, V.A. Golyashov, A.S. Kozhukhov, I.P. Prosvirin, A. A. Shklyaev.* Stability of the (0001) surface of the Bi_2Se_3 topological insulator. JetpLett. 2011, vol. 94, pp. 465–468. doi.org/10.1134/S0021364011180159

[13] *D. Kong, J.J. Cha, K. Lai,H. Peng, J.G. Analytis, S. Meister, Y. Chen, H.J. Zhang, I.R. Fisher, Z.X. Shen, Y. Cui.* Rapid surface oxidation as a source of surface degradation factor for Bi_2Se_3. ACS Nano, 2011, vol. 5, pp. 4698-4703. doi: 10.1021/nn200556h.

[14] *I. Childres, J. Tian, I. Miotkowski, Y. Chen.* AFM and Raman studies of topological insulator materials subject to argon plasma etching. *Philosophical Magazine.* 2013, vol. 93, iss. 6, pp. 681-689. doi.org/10.1080/14786435.2012.728009

[15] *V.Ya. Tyagay and O.V. Snitko,* Electroreflection of Light in Semiconductors (NaukovaDumka, Kiev, 1980, 302p) [in Russian].

[16] *M. Cardona.* Solid state physics: Modulation spectroscopy. AcademicPress, Inc.; 1St Editionedition, 1969, 358 p.

[17] *K. Taniguchi, A. Moritani, C. Hamaguchi, J. Nakai.* Electro- and thermoreflectance of Bi_2Te_3, and Bi_2Se_3, Surface science, 1973, vol.37, pp. 212-217.

[18] *D. Hsieh, Y. Xia, D. Qian, L. Wray, J. H. Dil, F. Meier, J. Osterwalder, L. Patthey, J.G. Checkelsky, N. P. Ong, A.V. Fedorov, H. Lin, A. Bansil, D. Grauer, Y.S. Hor, R.J. Cava, M.Z. Hasan.* A tunable topological insulator in the spin helical Dirac transport regime. *Nature*, 2009, vol. 460, iss. 27, pp.1101–1106. doi.org/10.1038/nature08234

[19] *K. Jeong, H. Park, J. Chae, K.I. Sim, W.J. Yang, J.H. Kim, S.B. Hong, J. H. Kim, M-H. Cho.* Topological phase control of surface states in Bi_2Se_3 via spin-orbit coupling modulation through interface engineering between HfO_{2-X}. ACS Applied Materials&Interfaces, 2020, vol. 12,pp. 12215–12226. DOI:10.1021/acsami.9b17555

CONTENTS